University of California

Los Angeles

A Measurement of the Top Quark Cross-Section at $\sqrt{s} = 1.96$ TeV at the Collider Detector at Fermilab

A dissertation submitted in partial satisfaction

of the requirements for the degree

Doctor of Philosophy in Physics

by

David James Goldstein

2004

© Copyright by

David James Goldstein

2004

The dissertation of David James Goldstein is approved.

Timothy Solberg

Katsushi Arisaka

James Rosenzweig

David Saltzberg, Committee Chair

University of California, Los Angeles

2004

To my parents, Marie and David,

and in memory of my grandmother, Lena, and my grandfather, Jacob

Table of Contents

1 Introduction **1**

1.1 Definition of the cross-section 2

1.2 Units 3

2 Theory **4**

2.1 History 5

2.1.1 CP violation 5

2.1.2 Charm and τ 5

2.1.3 Beauty and weak isospin 6

2.1.4 Flavor-changing neutral currents 8

2.1.5 Cancellation of anomalies 9

2.2 $t\bar{t}$ production in the Standard Model 10

2.3 Standard Model decays of $t\bar{t}$ to dileptons 17

3 Apparatus **22**

3.1 Fermilab Run II accelerator complex 22

3.1.1 Proton beam 22

3.1.2 Antiproton beam 24

3.1.3 Colliding beams 25

3.2 Collider Detector at Fermilab 25

3.2.1 Silicon tracking systems 30

3.2.2 Central Outer Tracker 34

3.2.3 Magnetic field 34
3.2.4 Calorimetry 37
3.2.5 Muon systems 45
3.2.6 Trigger systems 45

4 Identification of leptons and jets 50

4.1 Electrons in the endplug detectors 50
4.1.1 Preliminary studies 50
4.1.2 Plug ID variables for the $t\bar{t}$ cross-section analysis 55
4.1.3 PEM electron ID efficiencies 57
4.1.4 PEM ID efficiency scale factor 58
4.1.5 Background rejection 61
4.1.6 Validation of PHX electrons 63
4.1.7 Future improvements to the PES ratio variable 69
4.2 Electrons in the central detector 71
4.3 Muons 72
4.4 Jets 77
4.5 Missing transverse energy 78

5 Event selection and acceptance 80

5.1 Corrections to event variables 80
5.1.1 Vertex correction 80
5.1.2 CEM and PEM energy corrections 80
5.1.3 Curvature corrections 81

5.1.4 Jet corrections 82

5.1.5 Leakage correction to isolation 83

5.2 The H_T cut 83

5.3 Non-isolated leptons 86

5.4 Topological $\not\!\!E_T$ requirements 86

5.5 Jet significance 88

5.6 Data sets 91

5.7 Decay channels in the analysis 93

5.8 Dilepton event selection 93

5.9 Acceptance 96

5.10 Systematic uncertainties 98

6 Backgrounds 103

6.1 **WW/WZ** background 103

6.2 $\mathbf{Z} \to \tau^+\tau^-$ background 104

6.3 QCD fake background 105

6.4 Drell-Yan background 110

6.5 Systematic uncertainties 117

6.6 Total expected background 119

7 Results 121

7.1 b-tagged events 123

8 Discussion 137

References **138**

List of Figures

2.1 Example Feynman diagrams of direct flavor-changing neutral currents involving the b quark. 9

2.2 Example of a Feynman diagram which contributes to the triangle anomaly. 9

2.3 The $t\bar{t}$ production cross-section as a function of energy [17]. . . . 11

2.4 Feynman diagrams depicting leading-order $t\bar{t}$ production. Quark-antiquark annihilation is represented by the bottom diagram; the other two represent contributions from gluon fusion. 12

2.5 Example Feynman diagrams of processes which contribute corrections to the leading-order calculation of the $t\bar{t}$ production cross-section. 15

2.6 Charged lepton angular distributions from left-handed and longitudinal W bosons in $t\bar{t}$ decays [17]. 21

3.1 Pictorial overview of the Fermilab accelerator complex for Run II. 23

3.2 Diagram of one half of the CDF Run II detector. 27

3.3 Cut-away view of the CDF Run II detector. 28

3.4 Definition of coordinates used with the CDF Run II detector. . . 29

3.5 A three-dimensional drawing of the SVX detector. 30

3.6 Close up view of an ISL sensor ladder. 31

3.7 Design of the tracking volume for Run II at CDF. 32

3.8 Close-up view of three COT cells within a superlayer which illustrates the position of the wires with respect to the field sheets. . 35

3.9 End-on view of a portion of the COT showing how cells are arranged to form superlayers. 36

3.10 Top: Three-dimensional view of a central calorimeter wedge showing the location of each tower in pseudorapidity. Bottom: Illustration of the CES response to an EM shower. 39

3.11 Detail drawing of an endplug calorimeter for Run II. 40

3.12 Tower geometry for the CDF Run II endplug calorimeters. Each wedge covers 15° in azimuth. As shown, towers 0–14 span the region $1.1 < |\eta| < 2.11$, and towers 16–22 span the region $2.11 < |\eta| < 3.6$. 41

3.13 Schematic drawing of a 45° section of the PES detector. The segmentation into a low- and high-η region is shown. The PES is calibrated using a radioactive source, which traverses the indicated path during calibration and is retracted into a shielded box when not in use. 43

3.14 Map of the muon coverage for this analysis. 46

3.15 Cross-sectional view of drift tubes in a muon chamber. A stub is formed from the trajectory of a muon passing through the chamber, and the stub is matched to a track to become a reconstructed muon. 47

3.16 Block diagram of the Run II trigger system at CDF. 49

4.1 Average shower profile for test beam positrons incident on the U and V layers of the PES detector. The solid line is a 3-strip Lorentzian fit extrapolated to 9 strips; the dotted line corresponds to a Gaussian fit. 52

4.2 A distribution illustrating the method used to estimate the background fraction in the $W \to e\nu$ cross-section measurement using PEM electrons. Here *pem3x3Chisq* vs. *Had/EM* is shown, with all other selection requirements applied. The number of background events in the signal region, box "C," is estimated as the product $A \cdot (D/B)$. 54

4.3 Distributions of the plug electron ID variables for the candidate central/plug Z events. For these plots none of the cuts (indicated by the dashed vertical lines) have been applied. 59

4.4 'N-1' distributions of the plug electron ID variables for the candidate central/plug Z events. Cut values are indicated by the dashed vertical lines. 60

4.5 Plug ID variable efficiency and relative efficiency (data/MC) vs. E_T. Note that a background subtracted ID efficiency (see text for reference) is used to compute the average scale factor which is used in the analysis (0.96 ± 0.05). 62

4.6 Distributions of the plug electron ID variables for background (QCD jets) events. In these plots none of the cuts(indicated by the dashed lines) have been applied. 64

4.7 'N-1' distributions of the plug electron ID variables for background (QCD jets) events. Cut values are indicated by the dashed lines. 65

4.8 Distributions used in the determination of the data/Monte Carlo scale factor for PHX plug electrons. 67

4.9 Distributions of electron E_T, $\not{E}_T$, and transverse mass from our W boson cross-section measurement using PHX plug electrons. . 68

4.10 Distributions of electron E_T and invariant mass from our plug/plug Z cross-section measurement. 70

4.11 Distributions of the η vs.ϕ map for CMIO muons from data (top) and Monte Carlo (bottom). 76

5.1 Average number of interactions per crossing as a function of instantaneous luminosity. The current running conditions (36 bunches, $\mathcal{L} \approx 5\times10^{31}$ cm^{-2}s^{-1}) correspond to approximately one interaction per crossing. 84

5.2 The H_T distribution for $t\bar{t}$ and the WW and $Z\rightarrow\tau^+\tau^-$ background processes. 85

5.3 Distributions of $\Delta\phi\,(\not{E}_T$, nearest ℓ or jet) vs. $|\not{E}_T|$ for $Z\rightarrow\tau^+\tau^-$ Monte Carlo, $Z+jets$ data, and $t\bar{t}$ Monte Carlo. The region to the left of the dotted line is excluded by the event selection criteria. 87

5.4 Invariant mass distribution for dilepton $t\bar{t}$ events in the ee channel. The shaded region corresponds to the Z mass window ($76 < M_{\ell\bar{\ell}} <$ 106 GeV). Excluding this region represents a loss in acceptance of $\sim$24%. 89

5.5 Monte Carlo distributions of $\Delta\phi\,(\not{E}_T$, nearest jet) vs. $jetsig$ for $Z+jets$ events (top) and $t\bar{t}$ events (bottom). The selection requirements ($jetsig > 8$, $\Delta\phi > 10°$) are indicated by the lines. . . 90

6.1 Fake probabilities for electrons and muons as a function of E_T, integrated over all η. 109

6.2 The top plot shows an E_T distribution from Monte Carlo of electrons from b decay. The bottom plots show the electron (left) and muon (right) isolated and non-isolated fake probabilities, as a function of E_T, from 10 to 25 GeV. The contribution from b quarks becomes apparent below 20 GeV, and steadily increases as the E_T threshold is lowered. 111

7.1 H_T distribution of the dilepton candidiates compared with the Standard Model prediction. 124

7.2 $\not\!\!E_T$ distribution of the dilepton candidates compared with the Standard Model prediction. 125

7.3 Lepton p_T distribution of the dilepton candidates compared with the Standard Model prediction. 126

7.4 Invariant mass distribution of the dilepton candidates compared with the Standard Model prediction. 127

7.5 Distribution of the number of jets in the candidate events compared with the Standard Model prediction. 128

7.6 Distribution of the number of jets in the candidate events compared with the predicted Standard Model backgrounds. (No expected contribution from $t\bar{t}$ is shown.) The $\pm 1\sigma$ uncertainty on the total predicted background is indicated by the hatched fill pattern. 129

7.7 $\Delta\phi$ vs. $\not\!\!E_T$ distribution(s) of the dilepton candidates compared with the Standard Model prediction. The distribution from the Run I analysis is shown in the left-hand plot, and that from this analysis in the right-hand plot. The intriguing number of $e\mu$ events with large $\not\!\!E_T$ in the Run I distribution are not seen in this analysis. . 130

List of Tables

2.1 Standard model assignments for weak isospin, hypercharge, and electric charge. 6

2.2 Range of $t\bar{t}$ cross-section predictions at $\sqrt{s} = 1.96$ TeV for different values of m_t and mass scale (μ), using the CTEQ6M set of structure functions. The theoretical uncertainty, $\Delta\sigma$, is defined in the text. 16

2.3 Range of cross-section predictions at $\sqrt{s} = 1.96$ TeV for the combined study of the CTEQ6, MRST, and MRST with α_S variation sets of structure functions. The reference values are calculated using the CTEQ6M set. 17

2.4 Standard Model decays of the W^- boson in $t\bar{t} \rightarrow W^+W^-b\bar{b}$ events. W^+ decays to the charge-conjugate modes with the same branching ratios. 18

3.1 A comparison of the central and endplug calorimeters for Run II. In the rows corresponding to light yield, photoelectrons is abbreviated as "pe." 44

4.1 Plug electron ID cuts. *Si track* implies a 2-d Phoenix track. . . . 57

4.2 Efficiencies of plug electron ID variables. Here 'N-1' implies all other cuts have been applied *except* the cut in question. The uncertainties are statistical only. 61

4.3 Background rejection of plug electron ID variables. † For completeness the numbers for the ΔR variable are included; there are implicit cuts on ΔR in the electron reconstruction code which obscure the effect of this cut. 'Additional rejection' is computed at N-1 and implies:

#(N-1) ≡ # of evts passing all cuts but the one in question.

#(N) ≡ # of evts passing all cuts.

The value listed is then: [#(N-1) - #(N)] / [#(N-1)] . . . 63

4.4 Tight central electron (TCE) identification requirements. 73

4.5 Central muon ID cuts. 75

4.6 CMIO muon ID cuts. 75

5.1 Primary and secondary leptons defined for the analysis. 93

5.2 Dilepton decay channels defined in the analysis. The implied ordering is A/B, where A must be a primary lepton, and B can be either a primary or secondary lepton. The lepton corresponding to A must be associated with a trigger which is recorded in the event. All possible combinations are shown explicitly. 94

5.3 Breakdown of the ee portion of the $t\bar{t}$ acceptance. 98

5.4 Breakdown of the $\mu\mu$ portion of the $t\bar{t}$ acceptance. 99

5.5 Breakdown of the $e\mu$ portion of the $t\bar{t}$ acceptance. 100

5.6 Multilepton and general summary of the acceptance breakdown. . 100

5.7 Summary of the lepton scale factors (data/MC) used to correct the acceptance. 101

5.8 Summary of the relative contributions to the acceptance by detector region and lepton type. As listed in the text, the percentages correspond to the fraction of the total acceptance. The total number of dilepton channel events (3645) corresponds to a total acceptance of 0.916%. 101

6.1 Breakdown of the ee portion of the WW background estimate. . . 104

6.2 Breakdown of the $\mu\mu$ portion of the WW background estimate. . . 105

6.3 Breakdown of the $e\mu$ portion of the WW background estimate. . . 106

6.4 Multilepton and general summary of the WW background estimate.107

6.5 Breakdown of the ee portion of the WZ background estimate. . . 107

6.6 Breakdown of the $\mu\mu$ portion of the WZ background estimate. . . 108

6.7 Breakdown of the $e\mu$ portion of the WZ background estimate. . . 110

6.8 Multilepton and general summary of the WZ background estimate. 112

6.9 Breakdown of the ee portion of the $Z \to \tau^+\tau^-$ background estimate.112

6.10 Breakdown of the $\mu\mu$ portion of the $Z \to \tau^+\tau^-$ background estimate.113

6.11 Breakdown of the $e\mu$ portion of the $Z \to \tau^+\tau^-$ background estimate.114

6.12 Multilepton and general summary of $Z \to \tau^+\tau^-$ background estimate.115

6.13 Estimated contributions to dilepton backgrounds from QCD fakes in $126\,\mathrm{pb}^{-1}$. The errors are statistical only. 115

6.14 Expected contribution of fakes in 100 pb^{-1} from ten different $Wb\bar{b}$ Monte Carlo samples. 116

6.15 Fake probabilities of non-isolated leptons determined from a b-enriched data sample. 116

6.16 Drell-Yan background estimate for 126 pb^{-1} inside the Z window. The errors are statistical only. 117

6.17 Drell-Yan background estimate for 126 pb^{-1} outside the Z window. The errors are statistical only. 117

6.18 Systematic uncertainties for each lepton type for the background estimate from QCD fakes. 118

6.19 Summary of systematic uncertainties assigned to the background estimates. 119

6.20 Total predicted background from each process in 126 pb^{-1} including statistical and systematic uncertainties. 120

7.1 Run and event numbers for the candidate events. Events with a * have a tagged b jet; events with a ** are double tagged. 122

7.2 Central (isolated) + central (isolated) summary. 131

7.3 Central (isolated) + central (non-isolated) summary. 132

7.4 Central/plug (both isolated) + plug/plug (both isolated) summary. 133

7.5 Central (non-isolated) + plug (isolated) summary. 134

7.6 Total summary (all categories, isolated + non-isolated). 135

7.7 Brief overall summaries of the observed and predicted numbers of events in each decay channel (top), and as a function of the number of jets, H_T, and opposite sign requirements (bottom). 136

Acknowledgments

This thesis would never have been written had I not gone to Los Alamos to work for a bit, and there discovered that attending graduate school was really something I thought worth doing. I thank Wayne Vernon for giving me that opportunity, and Mike Weber, Steve Gierman, John Plato, Dinh Nguyen, John Kinross, and Scott Volz for making my time there extremely rewarding.

Attending graduate school at UCLA has been a great experience; I thank Jamie Rosenzweig for encouraging me to come here, and my friend Alex Balk for convincing me it was an opportunity not to be missed.

I am indebted to my father and to Bill Simon, who did their best to help raise a sunken ship and prepare me to go back to school after a several year hiatus. I also thank Steve Cowley, Jamie Rosenzweig, and especially Ernest Abers for all their help and encouragement during the first year.

I thank Frank Chase for helping me develop the hardware for the RASNIK system at UCLA, and Greg Derylo and Ken Schultz for helping with the installation onto the silicon detectors at Fermilab. I also thank Jim Patrick for helping me wade through the morass of automated kerberos authentication.

I thank my friends, John and Larra Keel, for making life more interesting while they were around, and Janice, for making the Velvet Lounge complete. Andrew Scott helped me into the larger world of Linux system administration, and shared the secrets of concert acquisition. Mike Lindgren I thank for help with all things hardware and software, for nurturing my pack rat tendencies, and for years of great conversations. Rainer Wallny I thank for being a good friend ever since I met him, for good advice, and especially for gracefully tolerating the experience of a proper sized dinner.

Most importantly I thank my advisor, David Saltzberg, for giving consistently

good advice, for giving me plenty of opportunities, and for demonstrating great instincts as a physicist. I only hope I can put all that I've learned from him to good use in the coming years.

I am indebted to Arun Tripathi, who gracefully loaned me his laptop at SLAC (preventing an eminent disaster), and to Randy Herber for his expert knowledge of the awk and postscript programming languages.

I would also like to thank the rest of the UCLA group—Jay Hauser, Martin von der Mey, Jane Nachtman, Matt Worcester, Alon Attal, Brian Mohr, Charles Plager, and Michael Sutherland, for everything over the last several years. I have good memories of working with you all, and wish everyone the best of luck.

Finally I thank my parents, whose love and support has made all the difference in my life, and kept me going throughout graduate school.

My research work was supported by a grant from the U.S. Department of Energy.

Vita

1971	Born, Rochester, New York, USA.
1993	B.S. (Physics), University of California, San Diego.
1996 – 1997	Research Assistant, Los Alamos National Laboratory, Los Alamos, New Mexico.
1997 – 1999	Teaching Assistant, Department of Physics and Astronomy, University of California, Los Angeles.
1999	M.S. (Physics), University of California, Los Angeles.
1999 – present	Research Associate, Department of Physics and Astronomy, University of California, Los Angeles.

Publications

D. Goldstein and D. Saltzberg,
The RASNIK real-time relative alignment monitor for the CDF inner tracking detectors.
Nuclear Instruments and Methods in Physics Research **A 506** (2003) 92-100.

Abstract of the Dissertation

A Measurement of the Top Quark Cross-Section at $\sqrt{s} = 1.96$ TeV at the Collider Detector at Fermilab

by

David James Goldstein

Doctor of Philosophy in Physics

University of California, Los Angeles, 2004

Professor David Saltzberg, Chair

We present a measurement of the $t\bar{t}$ cross-section in the dilepton channel, using $126\,\mathrm{pb}^{-1}$ of data collected with the Collider Detector at Fermilab (CDF). The data set corresponds to the period March 2002 - May 2003 of Run II at the Fermilab Tevatron. The analysis includes the upgrade endplug detectors and plug silicon tracking for the first time in a top physics measurement. The total acceptance for dilepton top events is thereby increased by 30% over the Run I analysis. We find 10 candidates in the data; the measured value of the cross-section is $\sigma_{t\bar{t}} = (7.6 \pm 3.4_{stat.} \pm 1.5_{syst.})\,\mathrm{pb}$, to be compared with the Standard Model prediction at $\sqrt{s} = 1.96$ TeV of $\sigma_{t\bar{t}}^{NLO} = (6.7 \pm 0.5)\,\mathrm{pb}$. Kinematic distributions of the events are thus far not indicative of new phenomena beyond the Standard Model.

CHAPTER 1

Introduction

The discovery of the top quark in 1995 at Fermilab [1] marked the end of a long and difficult search. It was also yet another success for the Standard Model of particle physics (SM), which had strongly predicted its existence. The discovery occurred during the $1992 - 1996$ collider run of the Tevatron accelerator, known as Run I, which provided $p\overline{p}$ collisions at a center-of-mass energy of $\sqrt{s} = 1.8$ TeV. The Run I measurements of the $t\overline{t}$ cross-section in the dilepton, lepton + jets, and all-hadronic channels agreed with the SM prediction within errors, however the dilepton analysis results from CDF were remarkable: The central value of the cross-section was almost a factor of two above the theoretical prediction, and one of the kinematic plots exhibited an intriguing distribution of data points. Various statistical tests were used in an attempt to discern whether the dilepton events were indicative of new phenomena. No such evidence was found; however, the total number of top events written to tape in Run I was small.

For Run II at Fermilab, with upgraded detectors and an increase in the center-of-mass energy of the Tevatron from 1.8 to 1.96 TeV, it is immediately interesting to see a $t\overline{t}$ signal again. The strategy of this analysis is to move from the discovery mode of Run I top analyses and begin to develop the paradigm for higher statistics measurements of the top sector. The data set we use here is comparable in size to that of Run I, however within two years it should be large enough such that

CDF will test SM predictions with measurements limited by systematic errors. In this analysis we focus on increasing the acceptance for dilepton top decays, allowing a moderate loss in purity compared with previous measurements in the dilepton channel. One important feature of the analysis is the addition of higher angle lepton detection using the upgrade endplug detectors. This alone provides the largest gain in acceptance, and also increases the sensitivity of the analysis to new phenomena, which may exhibit different kinematics than SM $t\bar{t}$ production and decays.

The following chapter begins with a short review of the theoretical motivation and experimental evidence supporting the existence of the top quark, and concludes with an outline of the Standard Model calculations describing $t\bar{t}$ production and decays. Chapter 3 describes the accelerators at Fermilab, which are currently the world's only source of top quarks, and the CDF detector, which allows us to study them. Chapter 4 discusses the identification of leptons and jets. Chapter 5 details the selection of dilepton $t\bar{t}$ events, and the corresponding estimate of the detector acceptance. Chapter 6 discusses the estimation of backgrounds for the analysis. Chapter 7 presents the measured cross-section, followed by a short discussion which concludes the dissertation.

1.1 Definition of the cross-section

The cross-section of an elementary particle is defined according to

$$N_x = \sigma_x \cdot \int \mathcal{L}\, dt\,,$$

where N_x is the observed number of particles of type x, σ_x is the production cross-section for particle x, and $\mathcal{L}$ is the instantaneous luminosity of a beam of

particles. Luminosity is discussed further in chapter 3. The cross-section has units of area, and in the following chapters is typically expressed in *picobarns*, where 1 pb = 10^{-36} cm^2. When measuring a cross-section, we alter the naive expression

$$\sigma_x = \frac{N_x}{\int \mathcal{L}\, dt}$$

to account for the facts that our ability to selectively identify particles *only* of type x is not perfect, and that our apparatus will not detect particles with 100% efficiency. We therefore use the following expression as a working definition of the cross-section:

$$\sigma_x = \frac{\mathrm{N_x} - \mathrm{N_{bgd}}}{\mathcal{A}_{\mathrm{total}} \cdot \int \mathcal{L}\ dt}\,, \tag{1.1}$$

where $\mathcal{A}_{\mathrm{total}}$ represents the product of efficiency factors associated with a realistic apparatus, and $\mathrm{N_{bgd}}$ is the estimated number of "non-x" events which will pass all of the selection criteria.

1.2 Units

Throughout this thesis we employ so-called *natural units*, where $\hbar = c = 1$. This implies, for instance, that masses and momenta are expressed simply in units of energy (typically GeV).

CHAPTER 2

Theory

Our current understanding of nature is that all matter[1] is ultimately made up of only a few constituents, quarks and leptons, which thus far have not exhibited substructure. The Standard Model of particle physics (SM), which has provided an extremely accurate description of the strong and electroweak interactions of these particles, groups the known quarks and leptons into three generations.

$$\begin{bmatrix} u \\ d \end{bmatrix} \begin{bmatrix} c \\ s \end{bmatrix} \begin{bmatrix} t \\ b \end{bmatrix}$$

$$\begin{bmatrix} \nu_e \\ e \end{bmatrix} \begin{bmatrix} \nu_\mu \\ \mu \end{bmatrix} \begin{bmatrix} \nu_\tau \\ \tau \end{bmatrix}$$

In this chapter we review some of the underpinnings of this model, and discuss some of the history which led up to the discovery of the top quark. We then continue with an outline of the SM calculations describing $t\bar{t}$ production and decays.

[1]Possibly excepting 'dark matter' and 'dark energy,' the nature of which we do not yet understand.

2.1 History

Dedicated searches for the top quark began in the late 1970s, and continued vigorously for sixteen years before confirming its existence. Indirect evidence in support of top began to appear in the mid-1960s, however, and many such results appeared throughout the thirty years which followed before the discovery. In the following subsections we review some of the more compelling results.

2.1.1 CP violation

In 1964, an experiment at Brookhaven National Laboratory observed rare decays of neutral kaons which violated CP symmetry [2]. With the advent of this result, Kobayashi and Maskawa added a phase factor, $e^{i\delta}$, into the quark mixing matrix in order to introduce CP violation into the model [3]. At that time, only three quarks (u, d, s) were known to exist. The addition of the phase necessarily led them to propose three complete generations of quarks, since the smallest unitary matrix which can exhibit a non-removable phase is 3×3 in size. Although experiments have since confirmed the existence of a complex phase in the CKM matrix, and three full generations of quarks have been observed, this was a somewhat bold prediction at the time; CP violation did not have to be due to a phase in the mixing matrix, and not even the full second generation of quarks had been observed. Nevertheless, many people began to suspect that a top quark would some day be discovered.

2.1.2 Charm and τ

The mid-1970s marked two major discoveries in particle physics: In 1974,

Fermion			T_L^3	Y_L	T_R^3	Y_R	$Q_f\,(=T^3+Y)$
u	c	t	$+1/2$	$+1/6$	0	$+2/3$	$+2/3$
d	s	b	$-1/2$	$+1/6$	0	$-1/3$	$-1/3$
ν_e	ν_μ	ν_τ	$+1/2$	$-1/2$	–	–	0
e^-	μ^-	τ^-	$-1/2$	$-1/2$	0	-1	-1

Table 2.1: Standard model assignments for weak isospin, hypercharge, and electric charge.

experiments at Brookhaven [4] and SLAC [5] independently observed the charm quark ($J/\psi = c\bar{c}$), and one year later in 1975, another experiment at SLAC observed the τ lepton [6]. The discovery of charm completed the second generation of quarks, and provided evidence that the emerging quark model (later to become the 'Standard Model') was viable. Taken in the context of this model, the observation of the τ, a third generation lepton, then strongly suggested that the quark sector would also have a third generation.

2.1.3 Beauty and weak isospin

In 1977, only two years after the discovery of the τ lepton, an experiment at Fermilab observed the b quark ($\Upsilon = b\bar{b}$) [7]. Searches for a companion, the top quark, began immediately, based on the existence of the b and the empirically observed generational grouping of the previously discovered quarks and leptons. Although the quark model did not provide an explanation for the proliferation of generations, it did dictate that within any generation, the fermions must appear in left-handed doublets and right-handed singlets of weak isospin [8] (See Table 2.1). In accordance with the structure of the first two generations, the left-handed b quark was thus expected[2] to be part of a doublet, with its third component of

[2]We use the word 'expected' instead of 'required' here because of the historical context: Al-

weak isospin, $T^3_{b_L} = -1/2$, and the right-handed b quark a singlet state, with $T^3_{b_R} = 0$. If there were no sixth quark, the b would appear only as a singlet state, with $T^3_{b_L} = T^3_{b_R} = 0$. These parameters can be determined, however, from measurements of the forward-backward asymmetry and the total width in $b\bar{b}$ production. The earliest results were direct measurements of the left- and right-handed weak isospin of the b quark, reported in the early 1980s by the JADE collaboration at DESY [9]. Their measurements suggested that the b quark was indeed the member of a doublet: $T^3_{b_L} = -0.490^{+0.015}_{-0.012}$, $T^3_{b_R} = -0.028 \pm 0.056$. More recent efforts concentrated on the forward-backward asymmetry; the most precise measurements came from LEP, where the process in question was $e^+e^- \to Z^0 \to b\bar{b}$. The asymmetry, $A_{FB}(b)$, is defined as:

$$A_{FB}(b) = \frac{\int_0^1 dz\ (d\sigma/dz) - \int_{-1}^0 dz\ (d\sigma/dz)}{\int_{-1}^1 dz\ (d\sigma/dz)} = \frac{\mathrm{N_{Forward}} - \mathrm{N_{Backward}}}{\mathrm{N_{Forward}} + \mathrm{N_{Backward}}},$$

where $z = \cos\theta$ (θ is the angle of the b quark with respect to the e^- in the center-of-mass frame), and σ refers to the cross-section for $e^+e^- \to b\bar{b}$ at $\sqrt{s} = M_Z$. At the Z^0 resonance, the forward-backward asymmetry may be expressed in terms of the vector and axial couplings to the electron and the b quark,

$$A_{FB}(b) = \frac{3\, V_e\, A_e\, V_b\, A_b}{(V_e^2 + A_e^2)(V_b^2 + A_b^2)},$$

with

$$\begin{aligned} V_f &= T^3_f - 2\, Q_f \sin^2\theta_W \\ A_f &= T^3_f \end{aligned},$$

where Q_f denotes the fermion charge, and θ_W is the weak mixing angle (Weinberg

---

though the SM requires this to be true, it was only expected in the late 1970s because the quark model was not yet viewed as a mature established theory (*i.e.* it had not become "the Standard Model" yet.).

angle). The expression is proportional to T_b^3, hence if the b quark were a singlet of weak isospin, one would expect a forward-backward asymmetry equal to zero. If the left-handed b quark were a member of a doublet, one would expect a forward-backward asymmetry of 0.10204 (using $\theta_W = 0.23172$). Measurements from the LEP collaborations found $A_{FB}(b) = 0.0941 \pm 0.0030$ [10], consistent with the b quark being part of a doublet with a companion t quark.

2.1.4 Flavor-changing neutral currents

In 1983, the UA1 and UA2 collaborations at CERN observed the massive $W^{\pm}$ and Z^0 gauge bosons [11, 12, 13]. This provided direct evidence for both charged- and neutral-current weak interactions, and elevated the status of the quark model to that of a mature theory, the Standard Model. An important feature of the theory is the absence of direct flavor-changing neutral currents (FCNCs), such as those illustrated in Figure 2.1. In contrast, theoretical models with only one third-generation quark predict the existence of FCNCs which should be observable in B meson decays. Kane and Peskin had shown in 1981 [14] that, if the b quark were a singlet of weak isospin and decayed via the W and Z bosons, the ratio of partial widths of B decays would be such that

$$\frac{\Gamma(B \to X\ell^+\ell^-)}{\Gamma(B \to X\ell^+\nu)} \geq 0.12\,,$$

where the relation holds no matter how many quarks the b is allowed to mix with. This implies a branching ratio $BR(B \to X\ell^+\ell^-) > 0.013$. In 1987 the CLEO collaboration measured $BR(B \to X\ell^+\ell^-) < 0.0012$ at 90% confidence level [15], effectively ruling out models with only five quarks.

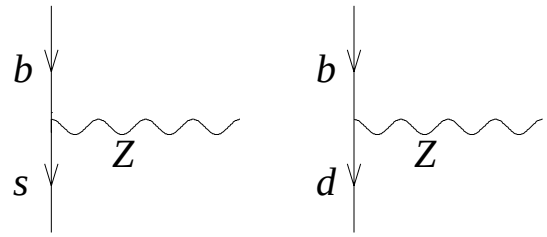

Figure 2.1: Example Feynman diagrams of direct flavor-changing neutral currents involving the b quark.

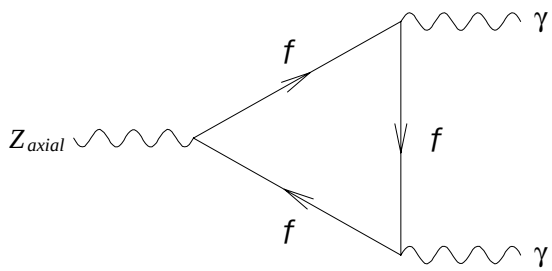

Figure 2.2: Example of a Feynman diagram which contributes to the triangle anomaly.

2.1.5 Cancellation of anomalies

Once the SM was established, purely theoretical arguments which demand the existence of a top quark became more important. One such argument arises from the so-called *triangle anomaly*[3] [16, 17], which occurs due to Feynman diagrams such as those shown in Figure 2.2. All of these diagrams contain a triangle loop of virtual fermions which couples to gauge fields via one axial and two vector

[3]This anomaly has been exhaustively studied, and is also known as the *chiral anomaly, axial anomaly,* or γ_5 *anomaly.* Note that the gauge fields in Figure 2.2 do not have to be external lines.

couplings. Anomalies in quantum field theory (QFT) occur when classical symmetries are destroyed by quantum effects, and usually involve currents which, although conserved at the classical level, have non-vanishing divergence. When the corresponding symmetry is global, anomalous currents are not problematic to the theory and in fact have real phenomenological effects. For example, the strong isospin current (which corresponds to a global symmetry in the approximation $m_u = m_d$) is anomalous, and is responsible for the decay of the π^0 meson. When the corresponding symmetry is local, an anomaly cannot persist or the theory will be invalidated. In the case of the triangle anomaly, the non-removable divergence is typically ascribed to the axial current, however this turns out to be due to an aesthetic choice which has become historical: When analyzing any *one* such diagram, it is impossible to remove the offending terms completely, however the contribution from *either* the axial or the vector current can be removed. The vector current was thought to be more sacred since it couples to the photon, hence the choice was made to associate the anomaly with the axial current.

If the triangle anomaly cannot be made to cancel, this anomaly is disastrous for the SM, rendering it both non-renormalizable and non-unitary. Summing the contribution to any such diagram over all fermions, however, one finds cancellation *per generation* provided that there is a complete set of both leptons and quarks. Thus the existence of the top quark as the partner of the τ, ν_τ, and b is required to avoid breaking the SM.

2.2 $t\bar{t}$ production in the Standard Model

At the current energy of the Tevatron collider (1.96 TeV) the production of $t\bar{t}$ pairs is just beginning to be kinematically accessible, as shown in Figure 2.3. As a consequence, the production mechanism is dominated by quark-antiquark

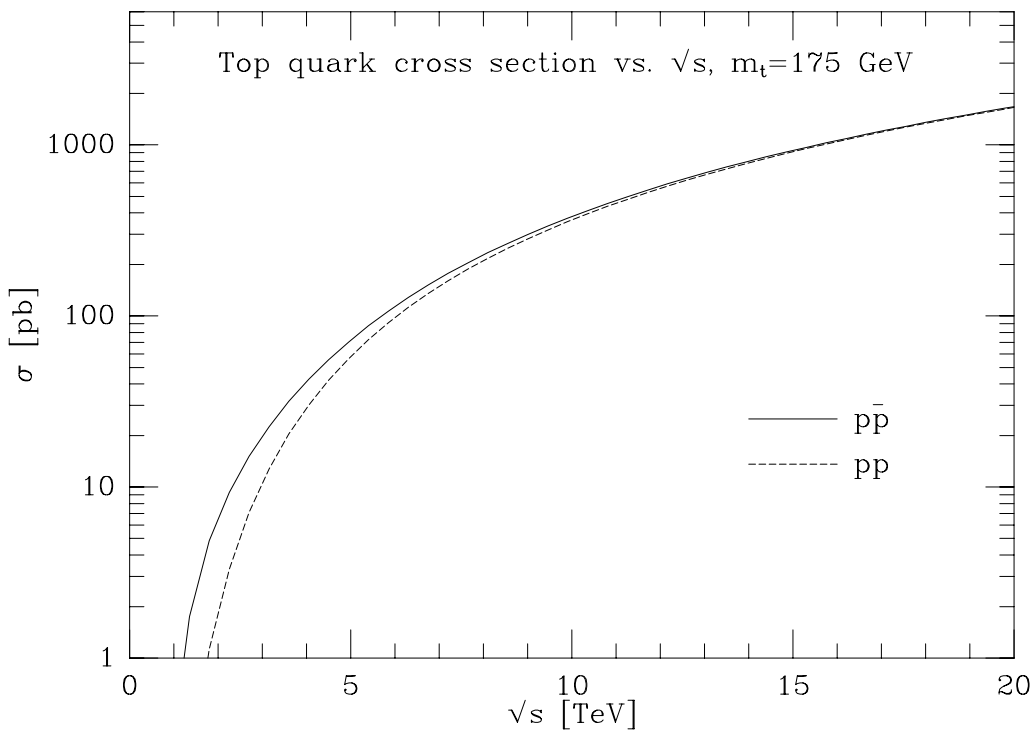

Figure 2.3: The $t\bar{t}$ production cross-section as a function of energy [17].

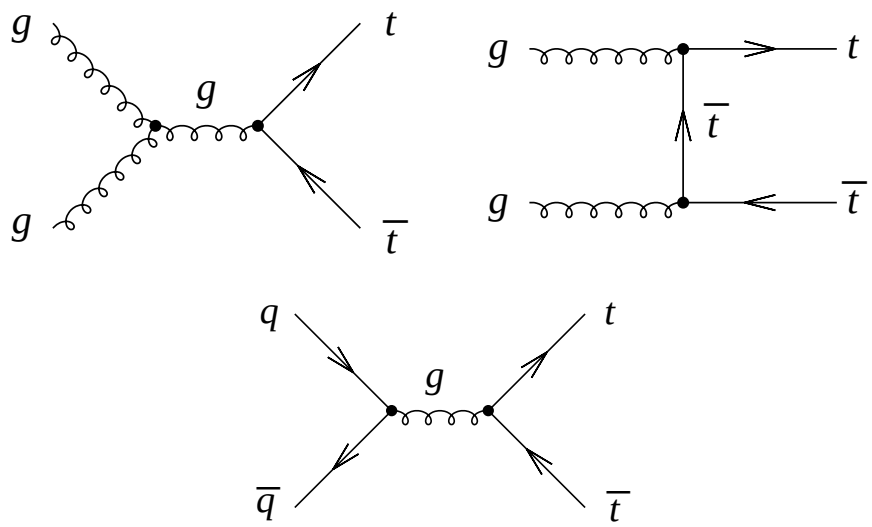

Figure 2.4: Feynman diagrams depicting leading-order $t\bar{t}$ production. Quark-antiquark annihilation is represented by the bottom diagram; the other two represent contributions from gluon fusion.

annihilation, and theoretical estimates of the $p\overline{p} \to t\bar{t}$ cross-section are fairly well approximated by leading-order processes, shown here in Figure 2.4. The large mass of the top quark necessarily involves a large momentum transfer ($Q^2 \gg \Lambda^2_{QCD}$) between incoming partons, hence the process of $t\bar{t}$ production should be well described by perturbative QCD. In the remainder of this section we present a summary of the SM calculation of the $t\bar{t}$ cross-section to leading-order [17].

In this regime, the inclusive hadronic cross-section for a heavy quark of mass m can be written as

$$\sigma(P_1, P_2) = \sum_{i,j} \int dx_1 dx_2 \; f_i(x_1, \mu^2) f_j(x_2, \mu^2) \; \hat{\sigma}_{ij}(s, m^2, \mu^2) \tag{2.1}$$

where P_1 and P_2 are the momenta of the initial state partons, the sum is over

types of incoming partons, and

$$\hat{\sigma}_{ij}(s, m^2, \mu^2) = \frac{\alpha_S^2(\mu^2)}{m^2} \mathcal{F}_{ij}\left(\rho, \frac{\mu^2}{m^2}\right). \tag{2.2}$$

The f_i and f_j are structure functions for the incident partons, which represent the probability that a given quark or gluon carries a fraction of the incoming hadron's momentum between x and $x + dx$. The parameter ρ is defined as

$$\rho = \frac{4m^2}{(p_1 + p_2)^2}.$$

The parameter μ represents the renormalization and factorization scale, which will be discussed below. In Equation 2.1 the function $\hat{\sigma}_{ij}(s, m^2, \mu^2)$ provides a complete description of the short-distance cross-section in terms of the functions $\mathcal{F}_{ij}$, which are expanded perturbatively:

$$\mathcal{F}_{ij}\left(\rho, \frac{\mu^2}{m^2}\right) = \mathcal{F}_{ij}^{(0)}(\rho) + 4\pi\alpha_S(\mu^2)\left[\mathcal{F}_{ij}^{(1)}(\rho) + \overline{\mathcal{F}}_{ij}^{(1)}(\rho)\ln\left(\frac{\mu^2}{m^2}\right)\right] + \mathcal{O}(\alpha_S^2) \tag{2.3}$$

The leading-order functions $\mathcal{F}_{ij}^{(0)}$ are calculated by integrating the following expression:

$$d\hat{\sigma}_{ij} = \frac{1}{2(p_1 + p_2)^2} \frac{d^3p_3}{(2\pi)^3 2E_3} \frac{d^3p_4}{(2\pi)^3 2E_4} (2\pi)^4 \delta^4(p_1 + p_2 - p_3 - p_4) \overline{\sum} |\mathcal{M}_{ij}|^2 \tag{2.4}$$

where for ($q\overline{q} \rightarrow Q\overline{Q}$)

$$\overline{\sum} |\mathcal{M}|^2/(4\pi\alpha_S)^2 = \frac{4}{9}\left(\tau_1^2 + \tau_2^2 + \frac{\rho}{2}\right)$$

and for ($gg \to Q\overline{Q}$)

$$\overline{\sum}|\mathcal{M}|^2/(4\pi\alpha_S)^2 = \left(\frac{1}{6\tau_1\tau_2} - \frac{3}{8}\right)\left(\tau_1^2 + \tau_2^2 + \rho - \frac{\rho^2}{4\tau_1\tau_2}\right).$$

The symbol $\overline{\sum}$ denotes an average over spins and flavors, and τ_1 and τ_2 are defined as follows to make the expressions less cumbersome:

$$\tau_1 = \frac{2p_1 \cdot p_3}{(p_1 + p_2)^2} \qquad \tau_2 = \frac{2p_2 \cdot p_3}{(p_1 + p_2)^2}.$$

The results of the calculations are:

$$\begin{aligned}
\mathcal{F}^{(0)}_{q\overline{q}}(\rho) &= \tfrac{\pi\beta\rho}{27}\left[\,(2+\rho)\,\right] \\
\mathcal{F}^{(0)}_{gg}(\rho) &= \tfrac{\pi\beta\rho}{192}\left[\tfrac{1}{\sqrt{1-\rho}}[\rho^2 + 16\rho + 16]\ln\left(\tfrac{1+\sqrt{1-\rho}}{1-\sqrt{1-\rho}}\right) - 28 - 31\rho\right] \\
\mathcal{F}^{(0)}_{gq}(\rho) &= \mathcal{F}^{(0)}_{g\overline{q}}(\rho) = 0
\end{aligned} \tag{2.5}$$

Note that the quark-gluon contribution to the cross-section is zero at leading-order, but is present at higher orders. Corrections to these results from next-to-leading-order (NLO) processes involving real and virtual gluon emission are moderate ($\sim 20\%$) for the $q\overline{q}$ process, and large for the gg process. The situation at the Tevatron is fortunate in this respect: In $p\overline{p}$ collisions at $\sqrt{s} = 1.96$ TeV, the quark-antiquark production mechanism dominates over the gluon fusion process by a factor of nearly six to one. Some examples of diagrams which contribute corrections to the leading-order cross-section are shown in Figure 2.5.

We now return to the scale parameter μ, which is often the cause of some confusion. In order to calculate the functions $\mathcal{F}_{ij}$ in perturbation theory, one must perform subtractions in the course of renormalization and factorization. The subtractions are done at a specific mass scale, denoted by μ, which one is free to choose. In a calculation done to order α_S^n, one finds that changing μ

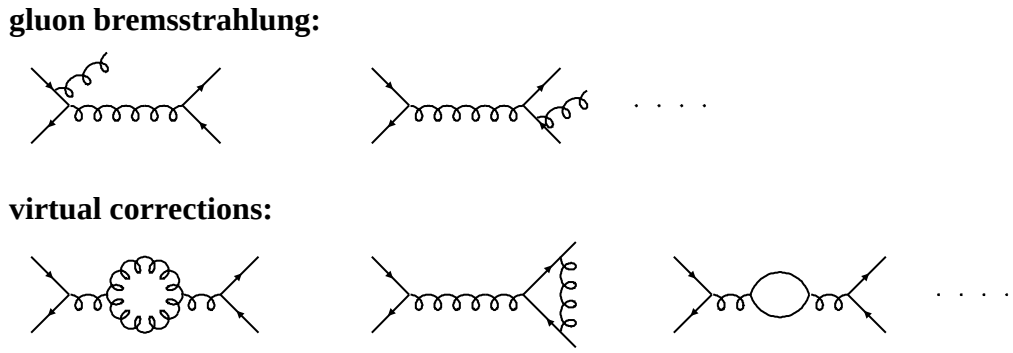

Figure 2.5: Example Feynman diagrams of processes which contribute corrections to the leading-order calculation of the $t\bar{t}$ production cross-section.

results in corrections of order α_S^{n+1}. An important point then is that μ is an unphysical parameter; the theoretical predictions obtained at a given order in perturbation theory are (should be) invariant under changes of μ, provided one has a well-behaved perturbation series. The invariance manifests itself in the following way: Although the coefficient of the correction obtained *is* different for different choices of μ, the scale dependence of the correction (its dependence on μ) alters the result such that the physical prediction is in the end the same. For the production of the known heavy quarks, the degree to which the perturbation series is well behaved turns out to be dependent on the mass of the quark itself. The current theoretical view is that, for the top quark (assuming $m_t \sim 175$ GeV), including higher-order corrections tends to stabilize the prediction with respect to changes in μ, whereas for the b quark the behavior is the opposite. In the analysis presented in this thesis, we use a theoretical value for the $t\bar{t}$ cross-section at $\sqrt{s} = 1.96$ TeV calculated to next-to-leading-order (NLO) [18]:

$$\sigma_{t\bar{t}} = (6.7 \pm 0.5)\,\text{pb}.$$

m_t [GeV]	μ	σ_{ref}(CTEQ6M) [pb]	$\Delta\sigma$ [pb]
170	$m_t/2$	7.97	0.57
170	m_t	7.83	0.54
170	$2m_t$	7.29	0.49
175	$m_t/2$	6.82	0.47
175	m_t	6.70	0.45
175	$2m_t$	6.23	0.42
180	$m_t/2$	5.86	0.40
180	m_t	5.75	0.38
180	$2m_t$	5.35	0.35

Table 2.2: Range of $t\bar{t}$ cross-section predictions at $\sqrt{s} = 1.96$ TeV for different values of m_t and mass scale (μ), using the CTEQ6M set of structure functions. The theoretical uncertainty, $\Delta\sigma$, is defined in the text.

This calculation uses the CTEQ6M set of structure functions and $\mu = m_t$. The same reference contains a comprehensive summary of the ranges of values obtained by varying several input parameters; Tables 2.2 and 2.3 give some representative examples. In Table 2.2, $\Delta\sigma$ represents the uncertainty due to PDFs, and is computed from

$$\Delta\sigma = \frac{1}{2}\sqrt{\sum_{i=1}^{n_{PDF}} (\sigma_{i+} - \sigma_{i-})^2},$$

where the sum is over pairs of uncertainties in the fits to the PDFs, and each pair corresponds to the fit obtained from varying the fit parameters by their own $\pm\sigma$ uncertainties. (In the equation $\sigma_{i\pm}$ are the computed cross-section values.)

Calculation of the $t\bar{t}$ cross-section is a topic of current theoretical research, however, and new estimates appear frequently as techniques evolve.

m_t [GeV]	σ_{min} [pb]	σ_{ref}(CTEQ6M) [pb]	σ_{max} [pb]
170	6.79	7.83	8.69
175	5.82	6.70	7.41
180	5.00	5.75	6.34

Table 2.3: Range of cross-section predictions at $\sqrt{s} = 1.96$ TeV for the combined study of the CTEQ6, MRST, and MRST with α_S variation sets of structure functions. The reference values are calculated using the CTEQ6M set.

2.3 Standard Model decays of $t\bar{t}$ to dileptons

The SM includes mixing between the six known quarks via the charged-current weak interactions. Using constraints from unitarity, the experimentally determined value of the CKM matrix element $|V_{tb}|$ is between 0.9989 – 0.9993 [19], hence the the matrix elements $|V_{ts}|$ and $|V_{td}|$ are suppressed by roughly a factor of a thousand. Top quarks will therefore decay almost exclusively to a real W boson and a b quark:

$$\begin{aligned} t \;&\longrightarrow\; W^+ + b \\ &\qquad\quad \hookrightarrow\; l^+ + \nu \end{aligned}$$

$$\begin{aligned} t \;&\longrightarrow\; W^+ + b \\ &\qquad\quad \hookrightarrow\; q + \overline{q'} \end{aligned}$$

where the charged lepton, l, can be either e, μ, or τ, and q and q' are first- or second-generation quarks. We characterize the possible final states by the decays of the W bosons, shown here in Table 2.4. Note that the branching ratios for the hadronic W decays include a factor of 3 from *color* (QCD) degrees of freedom. Analyses involving top quarks then fall naturally into the following three categories:

	Decay	Branching ratio
W^-	$e^-\overline{\nu}_e$	1/9
	$\mu^-\overline{\nu}_\mu$	1/9
	$\tau^-\overline{\nu}_\tau$	1/9
	$\overline{u}d$	3/9
	$\overline{c}s$	3/9

Table 2.4: Standard Model decays of the W^- boson in $t\overline{t} \rightarrow W^+W^-b\overline{b}$ events. W^+ decays to the charge-conjugate modes with the same branching ratios.

dilepton In the dilepton channel both W bosons decay leptonically. Processes involving τ leptons are generally not included due to the difficulty in identifying them in the detector. This channel is often referred to as the "golden mode," since it has the least background of the three channels; it suffers statistically, however, due to a low branching fraction: $(1/81 + 1/81 + 2/81) = 4/81$, approximately 5%. Dilepton events exhibit two high-p_T leptons, at least two energetic jets, and missing transverse energy from the neutrinos in the final state.

lepton+jets In the lepton+jets channel one W boson decays leptonically and the other hadronically. As in the dilepton channel, τ leptons are generally not included. The ability to identify b jets in the detector is crucial to the success of this analysis. The branching fraction is considerable: $(12/81 + 12/81) = 24/81$, approximately 30%. Lepton+jets events exhibit one high-p_T lepton, four energetic jets, and missing transverse energy from the neutrino in the final state.

all-hadronic In the all-hadronic channel, both W bosons decay hadronically. This channel is plagued by a large QCD background, however it has the largest branching fraction of the three channels: $(18/81 + 18/81) = 36/81$, approximately 44%. All-hadronic events exhibit six jets in the final state.

In the remainder of this section we summarize the SM calculations of properties of $t\bar{t}$ decays [17].

The W bosons resulting from $t\bar{t}$ decays are either left-handed ($helicity = -1$) or longitudinally polarized ($helicity = 0$), with the corresponding matrix elements squared given by

$$\begin{aligned} \overline{\sum}|\mathcal{M}_L|^2 &= \tfrac{2G_F m_t^4}{\sqrt{2}}|V_{tb}|^2\left[2x^2(1-x^2+y^2)\right] \\ \overline{\sum}|\mathcal{M}_0|^2 &= \tfrac{2G_F m_t^4}{\sqrt{2}}|V_{tb}|^2\left[1-x^2-y^2(2+x^2-y^2)\right] , \end{aligned} \tag{2.6}$$

where $x = m_W/m_t$ and $y = m_b/m_t$. The total width for the decay $t \to Wb$ is:

$$\Gamma(t \to Wb) = \frac{G_F m_t^3}{8\pi\sqrt{2}}|V_{tb}|^2\left[(1-x^2)(1+2x^2) - y^2(2-x^2-y^2)\right]\mathcal{L}(x,y)\,, \tag{2.7}$$

with

$$\mathcal{L}(x,y) = (1-(x+y)^2)(1-(x-y)^2).$$

Since $m_t > m_W \gg m_b$, this result can be simplified by setting m_b and m_W equal to zero. This leads to corrections of $\sim 0.3\%$, and of order $(m_W/m_t)^4 \approx 4.3\%$, respectively. The expression for the width is then simply:

$$\Gamma(t \to Wb) = \frac{G_F m_t^3}{8\pi\sqrt{2}}|V_{tb}|^2 \approx 1.76\,\mathrm{GeV}\left(\frac{m_t}{175\,\mathrm{GeV}}\right)^3 , \tag{2.8}$$

which for a heavy top is larger than the typical hadronic scale. Correspondingly,

the lifetime of the top quark is

$$\tau_t = 1/\Gamma \approx 3.7 \times 10^{-25}\,\mathrm{s}. \tag{2.9}$$

This implies a unique situation for top quarks: they will decay *before* they have time to form bound states, *i.e.* as free quarks. The spin of a produced top quark will therefore be correlated with the spins of its daughter particles. In the case of the W, the polarization state (left-handed or longitudinal) determines the angular distribution of the leptons into which it decays. The branching fraction for longitudinal W's produced in top quark decays is predicted by the SM to be:

$$\mathcal{R}_{W_0} \equiv \frac{\Gamma(t \to bW_0)}{\Gamma(t \to bW)} = \frac{m_t^2}{m_t^2 + 2m_W^2}. \tag{2.10}$$

For $m_t = 175$ GeV the longitudinal polarization state is favored, with $\mathcal{R}_{W_0} = 70\%$. To examine the angular distribution of leptons from W decays, one can define a lepton helicity angle, θ_e^*, which is the angle of the (charged) lepton in the rest frame of the W, with respect to the original direction of the W (anti-parallel to the b quark). Provided the jet from the b quark can be identified, this angle can be expressed in terms of experimentally observable quantities as:

$$\cos\theta_e^* \approx \frac{b \cdot (e - \nu)}{b \cdot (e + \nu)} \approx \frac{4b \cdot e}{m_t^2 - m_W^2} - 1\,, \tag{2.11}$$

where b, e, and ν represent the respective four-momenta. By making some approximations about the decay width of the W, one obtains the following helicity amplitudes for left-handed and longitudinally polarized states:

$$\begin{aligned} |D_L|^2 &= \tfrac{G_F m_W^4}{\sqrt{2}} \tfrac{1}{4}(1 - \cos\theta_e^*)^2 \\ |D_0|^2 &= \tfrac{G_F m_W^4}{\sqrt{2}} \tfrac{1}{2} \sin^2\theta_e^*. \end{aligned} \tag{2.12}$$

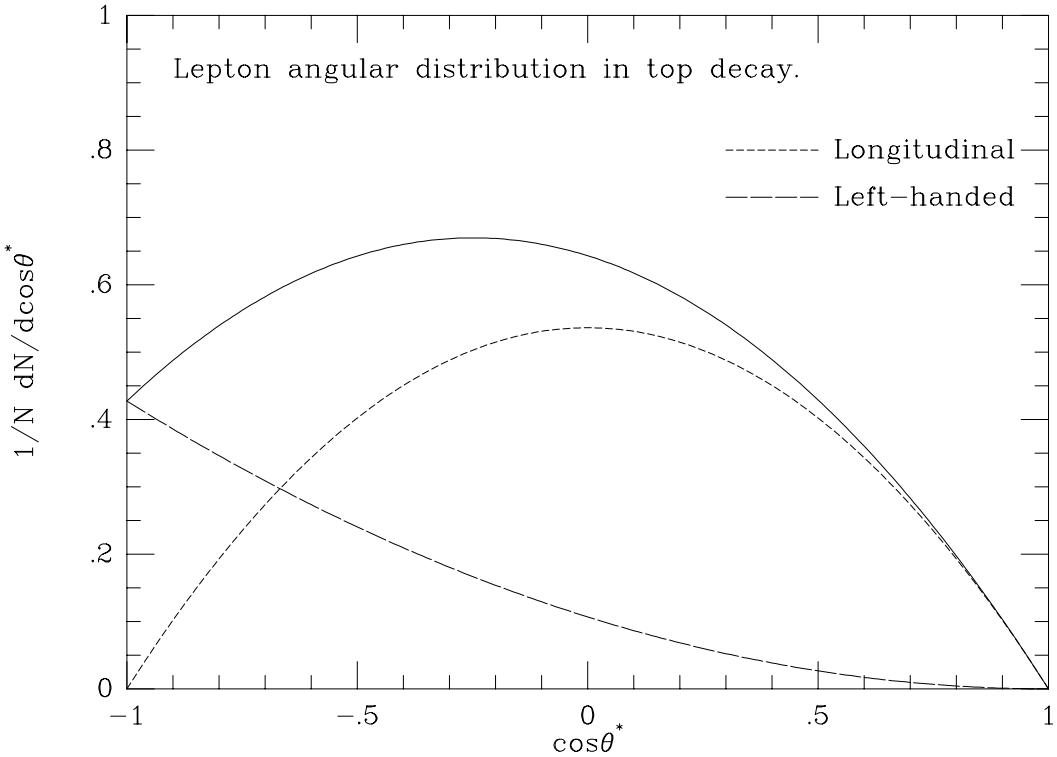

Figure 2.6: Charged lepton angular distributions from left-handed and longitudinal W bosons in $t\bar{t}$ decays [17].

These lead to a normalized angular distribution of the (charged) leptons, given by

$$\frac{1}{N}\frac{dN(W \to e\nu)}{d\cos\theta_e^*} = \frac{3}{4(m_t^2 + 2m_W^2)}\left[m_t^2 \sin^2\theta_e^* + m_W^2(1-\cos\theta_e^*)^2\right] , \qquad (2.13)$$

which is shown in Figure 2.6. Prospects for studying these distributions are discussed in chapter 8.

CHAPTER 3

Apparatus

Fermilab is currently the only laboratory in the world which can produce top quarks. In this chapter we describe the accelerators which make this possible, and the CDF detector, which allows us to study them.

3.1 Fermilab Run II accelerator complex

Run II at Fermilab consists of $p\overline{p}$ collisions at a center-of-mass energy of 1.96 TeV. Figure 3.1 provides a pictorial overview of the complex process which ultimately produces these collisions. Following this diagram, we describe the creation and acceleration of the proton and antiproton beams in the subsections below.

3.1.1 Proton beam

The creation of a proton beam begins with ordinary hydrogen gas (H_2). The hydrogen molecules are split electrostatically within a cesium-walled chamber, where some of them become ionized due to the low work function of cesium. The resulting H^- ions undergo their first stage of acceleration in a Cockcroft-Walton [20], which is a simple capacitor-diode voltage mutiplying array, much like that in a standard TV set. The Cockcroft-Walton accelerates the H^- ions

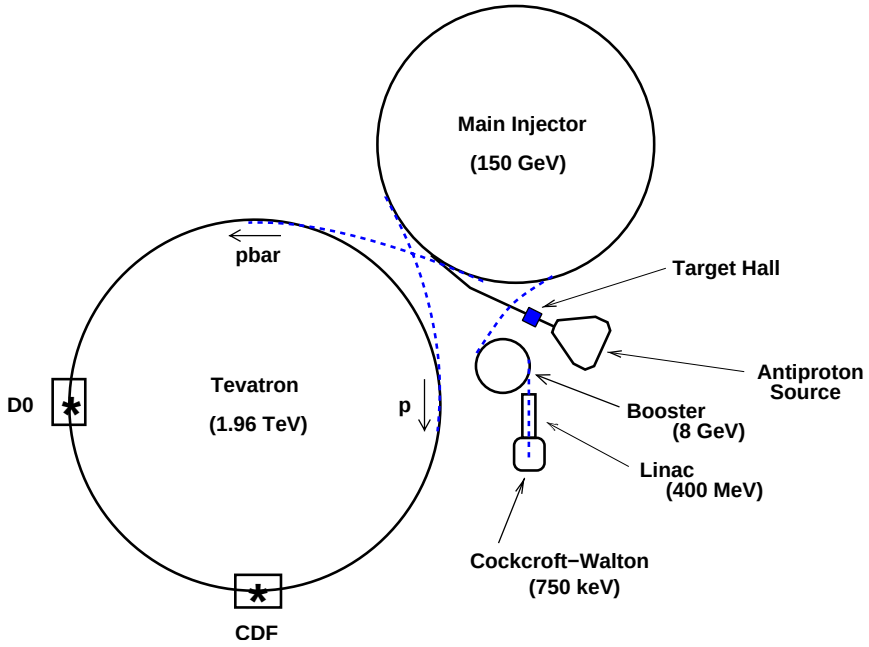

Figure 3.1: Pictorial overview of the Fermilab accelerator complex for Run II.

electrostatically to approximately 750 keV, where they enter a transfer section as continuous beam. The transfer section imparts a bunch structure to the beam, and injects it into the first stage of the Fermilab linear accelerator (linac), a standing-wave "Alvarez drift tube" linac [21]. The first section accelerates the ions to 116 MeV, where they pass through another coupling section and into the second stage, a 400 MeV side-coupled cavity linac. Upon exiting the linac, the ions pass through a thin carbon foil which removes the electrons. The beam (now composed only of protons) enters the booster, a 150 meter diameter synchrotron[1], which uses a multi-turn injection process since the time per revolution of a bunch (2.2 μs) is shorter than the pulse length of the linac (20 μs). The booster accelerates the proton beam to 8 GeV in a few hundreths of a second. From the

[1]A synchrotron works by simultaneously ramping the field in its bending magnets and the frequency of its RF cavity such that beam can gain energy while remaining in a stable orbit.

booster, the proton beam is transferred to the Main Injector (MI), which was a major part of the Run II upgrade to the Fermilab accelerator complex. In its collider injection mode, the MI (also a synchrotron) accelerates the proton beam to 150 GeV in a few seconds, and performs coalescing and cogging of the beam in preparation for injection into the Tevatron. The Tevatron is a superconducting synchrotron, approximately four miles in circumference, which accelerates the proton beam to its final energy of 980 GeV.

3.1.2 Antiproton beam

The creation of an antiproton beam is much more difficult, and begins with the Main Injector. In its antiproton mode the MI accelerates protons to 120 GeV and directs them to a nickel target, creating a spray of particles which contains a small number of antiprotons. The particles are produced into a large solid angle, and must be focussed in order to be collected. The focussing requirements are severe: The particles pass through a tubular piece of lithium which is made to support a current of 650 kAmps while they traverse it. This is known as the lithium *lens*, since the resulting magnetic field provides focussing which is everywhere directed radially inward. Upon exiting the lens, the particles are deflected by a pulsed magnet which selects antiprotons and other negatively charged particles. After a short distance the other particles decay, leaving an unruly beam of antiprotons. These are debunched and stochastically cooled [22], which increases the density of the beam by a factor of $\sim 18,000$. When enough antiprotons are circulating in the accumulator ring, they are transferred back into the MI, accelerated, and injected into the Tevatron in the opposite direction as the protons.

3.1.3 Colliding beams

In Run II the Tevatron operates with a 36 on 36 bunch structure (protons on antiprotons), with 396 ns spacing between bunches. At two points around the ring ("B0" and "D0") the beams are focussed by quadrupole magnets to achieve the highest luminosity possible within the detectors. The luminosity is given by

$$L = \frac{\gamma}{2\pi} f_o \, N_{\overline{p}} \, N_p \, B \, \frac{H}{\beta^* \, \epsilon_p \left(1 + \frac{\epsilon_{\overline{p}}}{\epsilon_p}\right)} \, , \tag{3.1}$$

where γ is the relativistic energy factor, f_o is the revolution frequency, N_p and $N_{\overline{p}}$ are the number of protons and antiprotons per bunch, B is the number of bunches of each type, β^* is the beta function at the center of the interaction region, ϵ_p and $\epsilon_{\overline{p}}$ are the proton and antiproton 95% normalized emittances, and H is the "hourglass form-factor" due to the bunch lengths. Although it depends explicitly on other quantities, increasing the proton and antiproton bunch intensities is the most direct way to increase luminosity. As of May 2003, the end date for the data set used in this analysis, the average peak luminosity was $3.7 \times 10^{31}\,\mathrm{cm}^{-2}\,\mathrm{sec}^{-1}$, and the average integrated luminosity per week was $5.9\,\mathrm{pb}^{-1}$. Both of these numbers are well short of the Run II goals, however much work was performed during the recent shutdown (Sept. – Dec. 2003) and the laboratory is hopeful that improvements will follow.

3.2 Collider Detector at Fermilab

The Collider Detector at Fermilab (CDF) is a multi-purpose detector designed to study the physics of high-energy $p\overline{p}$ collisions [23]. CDF provides charged particle tracking in a solenoidal magnetic field, time-of-flight measurement, electro-

magnetic and hadronic calorimetry, and muon detection. An elevation view of the detector is shown in Figure 3.2, and a cut-away diagram in Figure 3.3. The overall geometry of the detector is cylindrical, with the Tevatron beamline running through the center, along the axis of symmetry. CDF employs a right-handed global coordinate system, with the origin at the interaction point in the very center of the detector. The set of coordinates used $(r, \phi, z, x, y, \theta, \eta)$ is defined in Figure 3.4. The p and $\overline{p}$ beams circulating in the Tevatron are unpolarized, and bunches exhibit a longitudinal density profile such that the resulting distribution of collisions along the beam axis is Gaussian, with a width of about 30 cm. Since hadrons are composite objects, daughter particles from a $p\overline{p}$ collision are often produced with significant momentum along the $\hat{z}$ axis. It is thus useful to define two variables, *rapidity* and *pseudorapidity*:

rapidity (y) Rapidity (not to be confused with Cartesian y in Fig. 3.4) is defined as

$$y = \frac{1}{2} \ln \left(\frac{E + p_z}{E - p_z} \right) ,$$

where E is the energy of a particle, and p_z is the component of its momentum along the $\hat{z}$ axis. Rapidity is additive under Lorentz boosts in the $\hat{z}$ direction, and thus rapidity differences are invariant under such boosts. Particle production is empirically observed to be essentially flat in rapidity.

pseudorapidity (η) Pseudorapidity is defined as

$$\eta = -\ln \left(\tan \frac{\theta}{2} \right) ,$$

where θ is the polar angle measured from the $\hat{z}$ axis, as shown in Figure 3.4. Pseudorapidity is equivalent to rapidity for massless particles, and is approximately equivalent for particles with momentum much greater than

their rest mass. Pseudorapidity is experimentally convenient as a coordinate because the polar angle is easily measured within the detector.

Note that the detector is azimuthally symmetric about the $\hat{z}$ axis, and mirror symmetric about the plane transverse to the beamline, centered at $z = 0$.

Similar to the Fermilab accelerator complex, CDF is a complex entity which is comprised of many subsystems; those most important to this analysis are described in the following subsections, beginning nearest the interaction point and moving radially outwards.

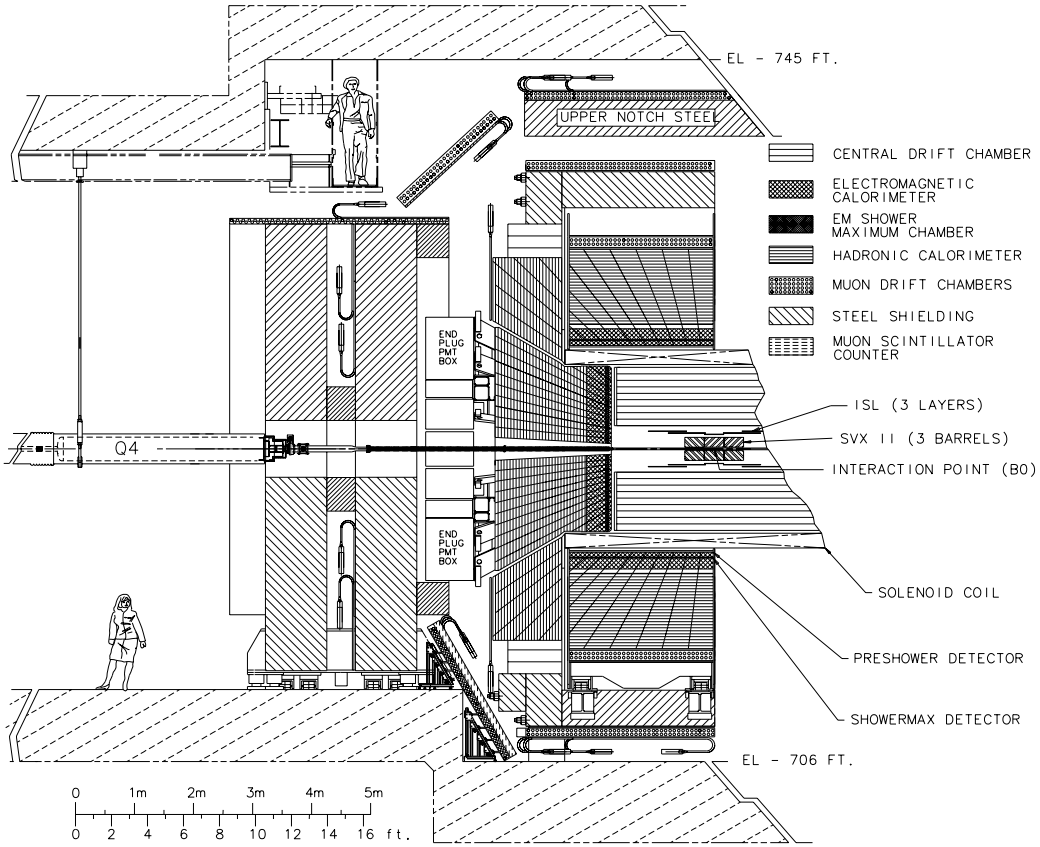

Figure 3.2: Diagram of one half of the CDF Run II detector.

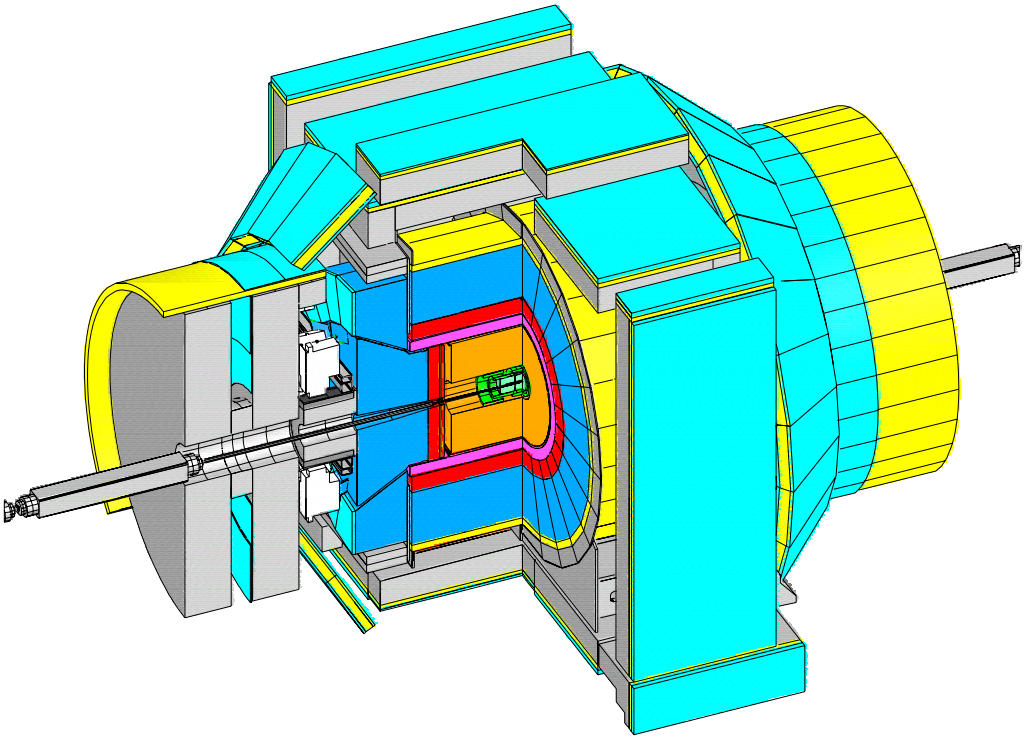

Figure 3.3: Cut-away view of the CDF Run II detector.

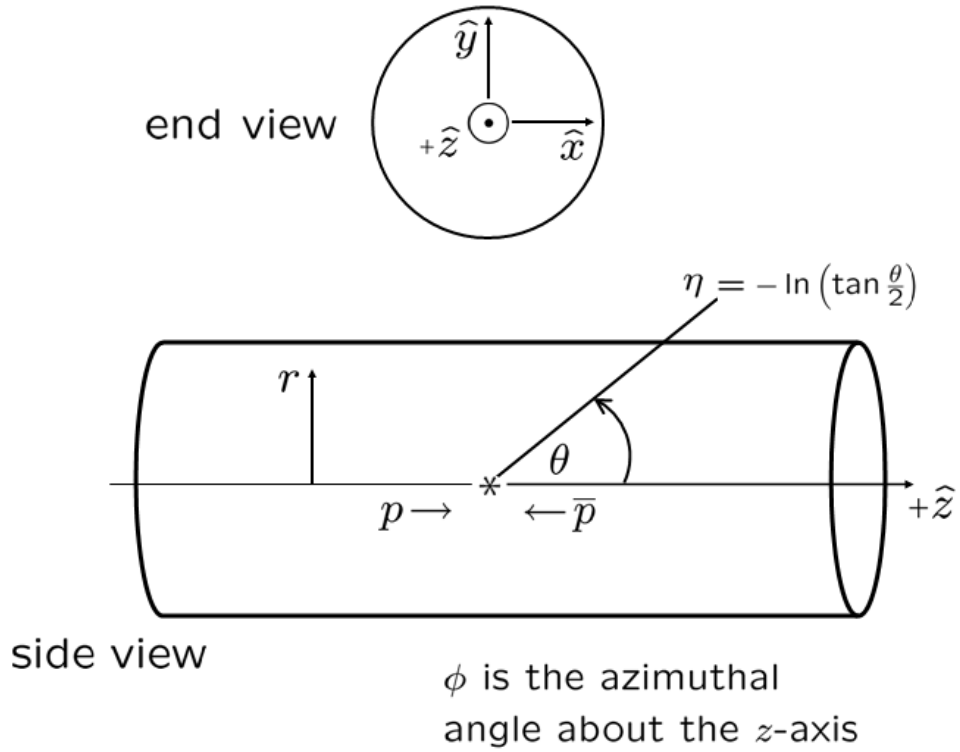

Figure 3.4: Definition of coordinates used with the CDF Run II detector.

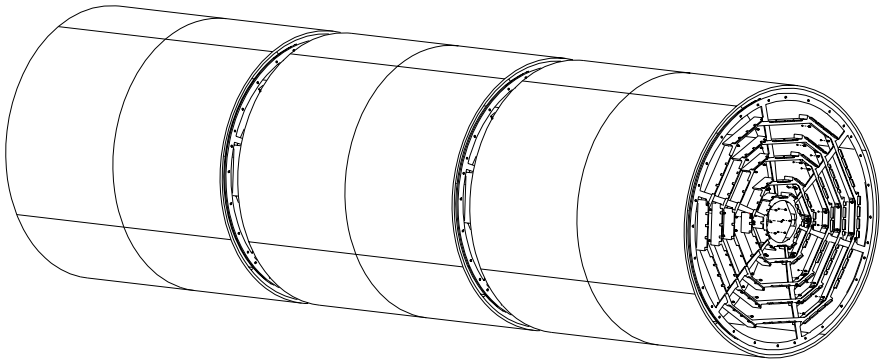

Figure 3.5: A three-dimensional drawing of the SVX detector.

3.2.1 Silicon tracking systems

Silicon tracking for Run II at CDF is composed of three independent subsystems: A layer of single-sided silicon mounted directly on the beampipe (known as 'Layer 00'), 5 layers of double-sided silicon located from $r = 2.44\,\text{cm}$ to $r = 10.6\,\text{cm}$ (known as 'SVX II'), and 1+2 layers of double-sided silicon located at $r = 22, 20,$ and 28 cm (known as 'ISL'). The Layer 00 detector is not yet usable for analysis, and will not be described further here. The SVX (Silicon Vertex detector) is segmented into three independent barrels, each 29 cm long, which together span a distance of 87 cm along the z-axis. Figure 3.5 shows a three-dimensional drawing of the SVX. The ISL (Intermediate Silicon Layers) detector consists of three independent sections, a central layer ($r = 22\,\text{cm}$, $0 < |z| < 25\,\text{cm}$), a mid-η layer ($r = 20\,\text{cm}$, $20 < |z| < 65\,\text{cm}$), and a high-η layer ($r = 28\,\text{cm}$, $42 < |z| < 87.5\,\text{cm}$). The structural and sensor designs for the SVX and ISL detectors are similar. A close-up view of an ISL sensor ladder is

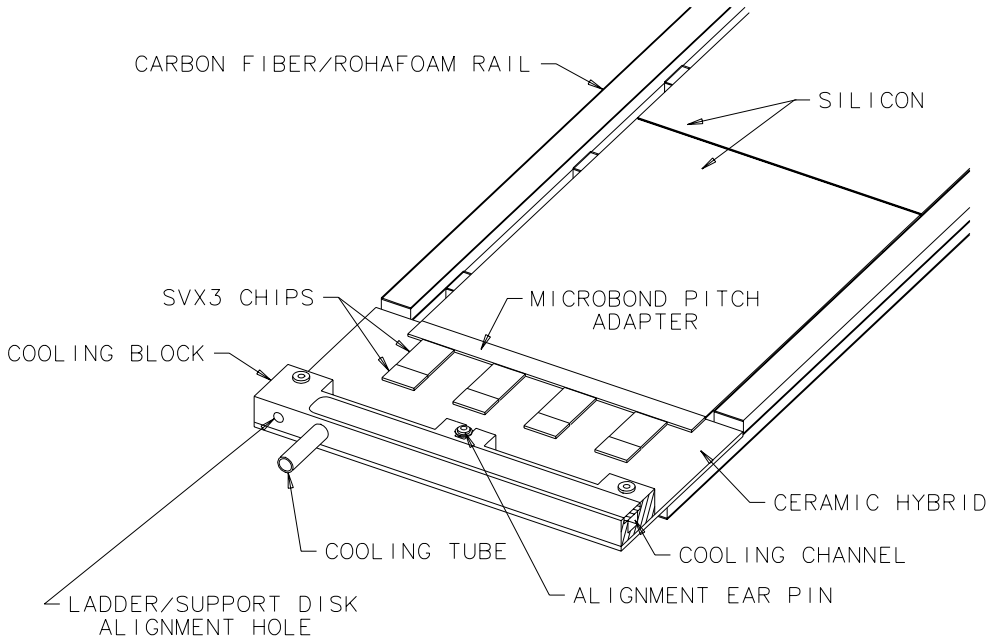

Figure 3.6: Close up view of an ISL sensor ladder.

shown in Figure 3.6. Together, the SVX and ISL detectors extend the reach of charged particle tracking at CDF to higher pseudorapidity. This is illustrated in Figure 3.7, which gives an overview of the designed tracking coverage for Run II. The silicon detectors also provide high spacial resolution near the interaction point, which is crucial for determining the precise location of vertices, including detached secondary vertices from b quark decays. The ability to identify jets which come from b quarks was of key importance in the Run I discovery of the top quark, and will be crucial to our ability to study the top sector with higher statistics in Run II.

3.2.1.1 RASNIK relative alignment system

To achieve optimum resolution for the identification of detached secondary

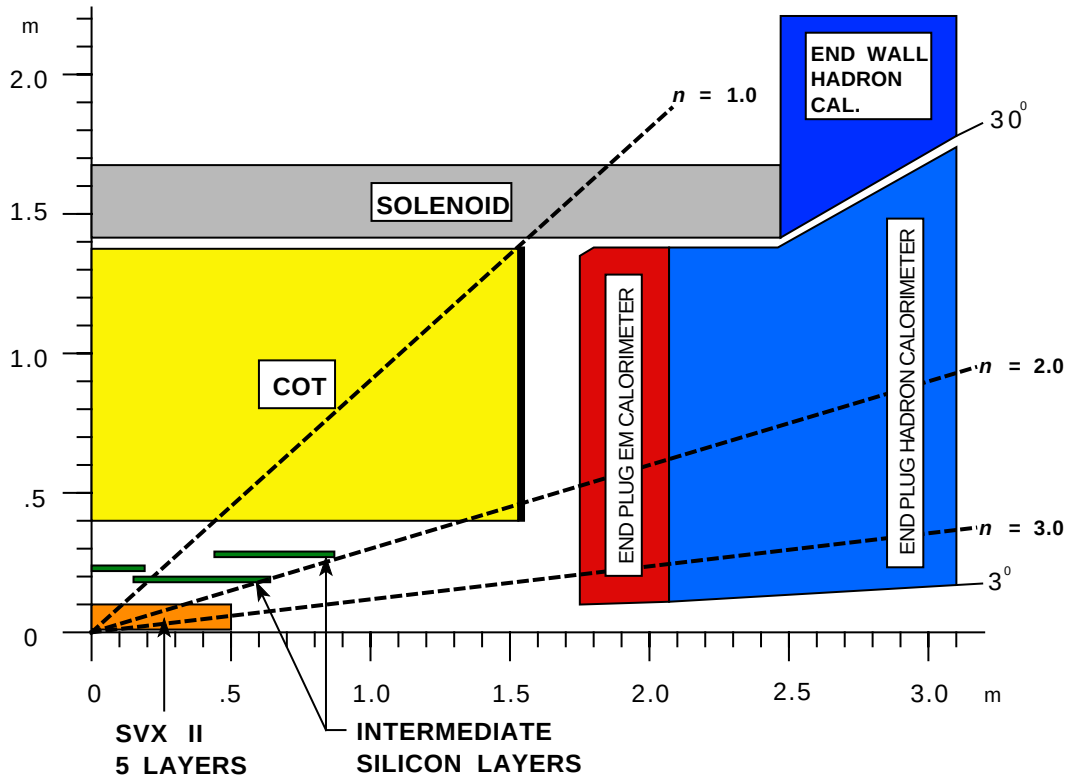

Figure 3.7: Design of the tracking volume for Run II at CDF.

vertices the components of the silicon trackers must remain stable relative to one another to approximately 10 μm. Detector alignment is typically accomplished with tracks taken over a long integration time, and alignment constants are thus only computed periodically. Without direct feedback from the tracker subsystems, such alignment periods could quickly become outdated if the detectors *in situ* are disturbed. In Run II, for the first time, CDF has installed a RASNIK[2] relative alignment system [24] on the silicon trackers, which provides measurements of relative position on the time scale of seconds with sensitivity better than 1 μm. For the CDF implementation we modified the original RASNIK design due to the severe space constraints and high-radiation environment present within the detector. With fewer distinct elements per system, the new design also reduces ambiguities in recorded RASNIK position data. In two years of running, the systems have exposed several sources of detector motion, and have demonstrated that the silicon trackers are extremely stable during data taking; this lends confidence that motions are not degrading the reconstruction and triggering capabilities of CDF. Plans for the future include mounting RASNIKs on the endplug calorimeters to track movements which occur during access periods (when the endplugs must sometimes be moved), and possibly installing systems on Tevatron magnets. Design, construction, installation, and operation of the RASNIK system for CDF was a major portion of the service work associated with this thesis. A NIM article has been published which provides more detailed information [25].

[2]The acronym 'RASNIK' stands for 'Relative Alignment System of NIKhef,' after the Nikhef Institute in the Netherlands, where the original technique was developed.

3.2.2 Central Outer Tracker

The Central Outer Tracker (COT) is the backbone of charged particle tracking for Run II at CDF. It is an open-cell drift chamber which provides coverage for the region $|\eta| < 1$, as shown in Figure 3.7. The COT is segmented into eight superlayers, located from $r = 40$ to 137 cm. Each superlayer holds a number of cells, the layout of which is shown in Figure 3.8. The cells are filled with Ar-Et gas (50:50 mixture + trace amount of isopropyl alcohol), which has a drift velocity of $\sim 200\mu$m/ns. Specifications for a given cell are a maximum drift length of approximately 0.9 cm, an operating drift field of 1.9 kV/cm, and a maximum drift time of about 175 ns. An end-on view showing how the cells and superlayers are organized is given in Figure 3.9. For high-p_T tracks such as those in $t\bar{t}$ events, the beam constrained momentum resolution of the COT is $\delta p_T/p_T^2 \leq 0.001\,(\mathrm{GeV/c})^{-1}$.

3.2.3 Magnetic field

The CDF detector features a 1.41 Tesla axial magnetic field throughout the tracking volume (approximately 2.8 m in diameter and 3.5 m long), which enables measurements of charge and momentum via the tracking detectors. The field points in the $-\hat{z}$ direction[3] of the CDF global coordinate system, as shown in Figure 3.4. The solenoid coil is superconducting, and employs an aluminum-stabilized NbTi conductor. The normal operating field of 1.41 T corresponds to a persistent current of 4650 Amps. The conductor is cooled indirectly via liquid helium, and reinforced structurally by an external support cylinder made of 5083 aluminum. The infrastructure also includes an iron return yoke. Although the

[3]The field is of course not perfectly axial, however the deviations are small and do not affect the analysis of the $t\bar{t}$ cross-section.

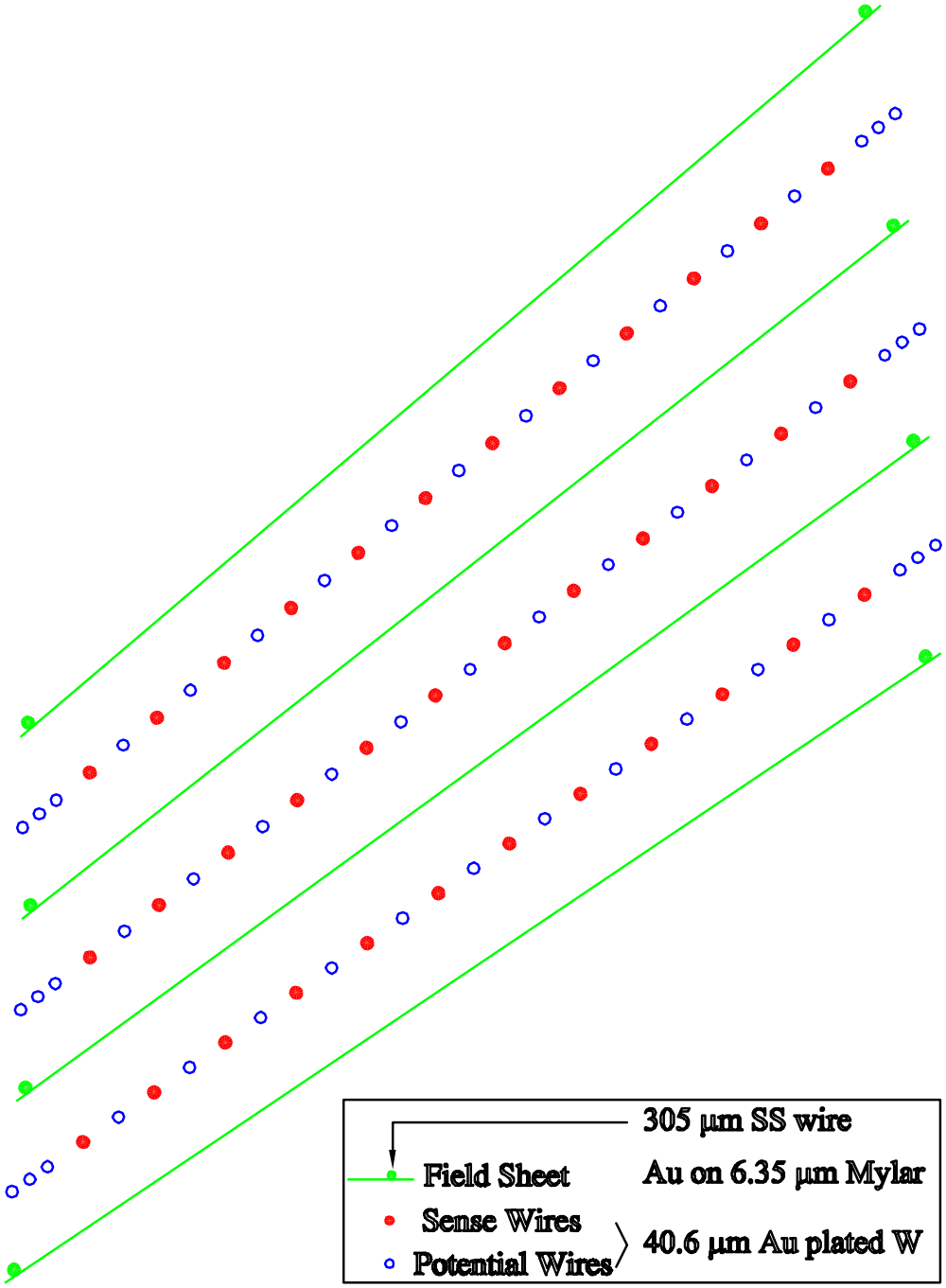

Figure 3.8: Close-up view of three COT cells within a superlayer which illustrates the position of the wires with respect to the field sheets.

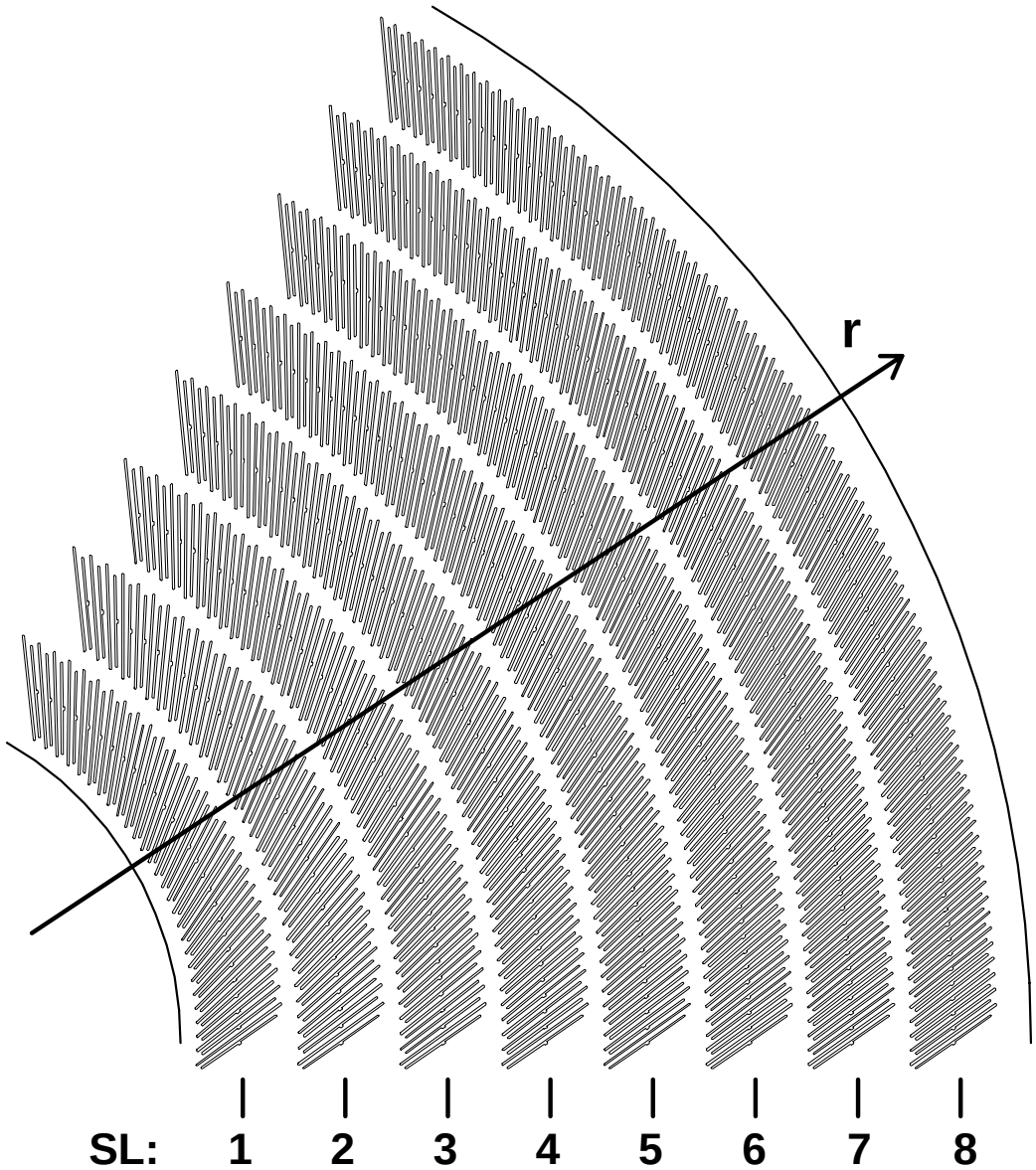

Figure 3.9: End-on view of a portion of the COT showing how cells are arranged to form superlayers.

solenoid was commissioned in the 1980's, and is subject to stresses during every thermal cycle, it was conservatively built and is expected to last throughout Run II.

3.2.4 Calorimetry

The calorimeter systems at CDF surround the tracking volume and solenoid, as shown in Figures 3.2 and 3.7, and provide energy measurement of electrons, photons, and jets. Each of the systems covers 2π in azimuth (ϕ), a range in pseudorapidity (η), and features an electromagnetic and a hadronic calorimeter. The calorimeters are segmented in η and ϕ to form projective *towers*, which point back to the (nominal) interaction region at $z = 0$. Towers exhibit a one to one EM:HAD matching geometry (with the exception of the two outer η rings in the endplugs), such that the ratio of electromagnetic to hadronic energy can be measured for an individual tower.

3.2.4.1 Central calorimeters

The central calorimeters at CDF are denoted as CEM (Central Electromagnetic), CHA (Central Hadron), and WHA (Wall Hadron). For Run II these systems are essentially unchanged, receiving only an electronics upgrade. The CEM and CHA are constructed in wedges which span 15° in azimuth and extend $\sim 250\,\mathrm{cm}$ in the positive and negative z direction. (There are thus 24 wedges on both the $+z$ and $-z$ sides of the detector, for a total of 48.) A wedge contains ten towers, each of which covers a range in pseudorapidity of approximately $\Delta\eta = 0.11$. This corresponds to a total span of $0 < |\eta| < 1.1$ for the CEM, and $0 < |\eta| < 0.9$ for the CHA. Note that the central calorimeters have two

phototubes per tower. The CEM is a lead-scintillator sampling calorimeter, approximately 19 X_0 (radiation lengths) in depth, and has an energy resolution of

$$\frac{\sigma(E)}{E} = \frac{14.0\%}{\sqrt{E_T}} \oplus 2\% \,,$$

where $\oplus$ denotes addition in quadrature. At a depth of approximately 6 X_0, the CEM contains a shower maximum detector called the CES. The CES employs proportional strip and wire counters in a fine-grained array to provide precise position and shape information ($\sim$2 mm resolution) for electromagnetic cascades. Figure 3.10 shows a three-dimensional view of a central calorimeter wedge and a close-up view of the CES.

The CHA is an iron-scintillator sampling calorimeter, approximately 4.5 λ_0 (interaction lengths) in depth, and has an energy resolution of

$$\frac{\sigma(E)}{E} = \frac{50.0\%}{\sqrt{E_T}} \oplus 3\%.$$

The WHA is also an iron-scintillator sampling calorimeter, spanning a range in pseudorapidity of $0.7 < |\eta| < 1.3$. The WHA has a depth of $\sim 4.5\,\lambda_0$, similar to the CHA, however it has worse energy resolution:

$$\frac{\sigma(E)}{E} = \frac{75.0\%}{\sqrt{E_T}} \oplus 4\%.$$

3.2.4.2 Endplug calorimeters

The Run II upgrade at CDF included new scintillating tile endplug calorimeters. As in the central region, there is an electromagnetic calorimeter (PEM) with a shower maximum detector (PES), and a hadronic calorimeter (PHA). Figure 3.11 shows the layout of the detector and coverage in polar angle ($3^\circ < \theta < 37^\circ$).

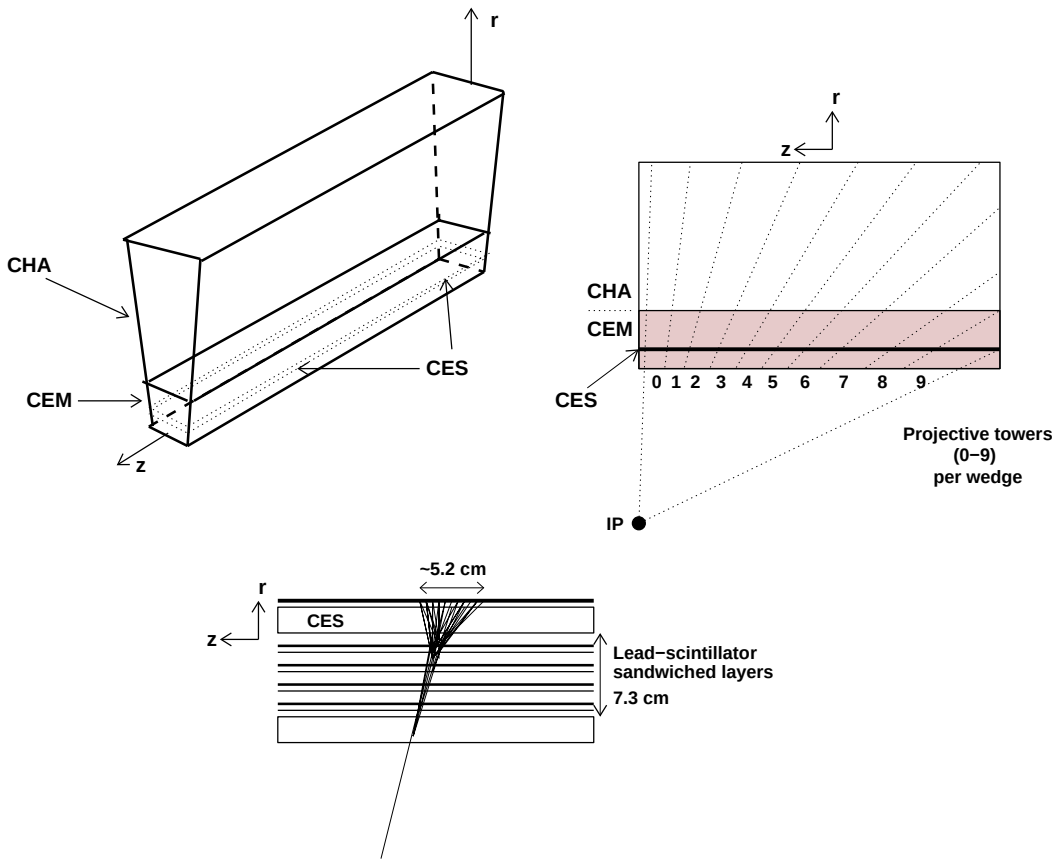

Figure 3.10: Top: Three-dimensional view of a central calorimeter wedge showing the location of each tower in pseudorapidity. Bottom: Illustration of the CES response to an EM shower.

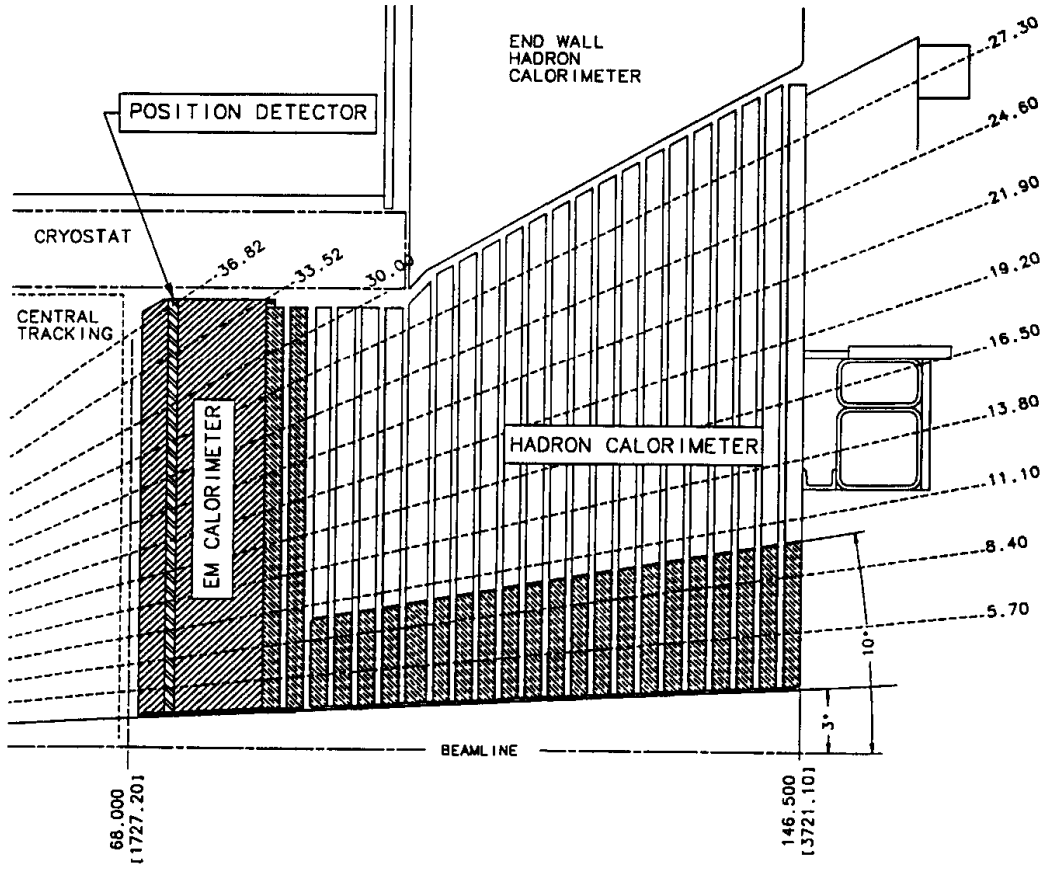

Figure 3.11: Detail drawing of an endplug calorimeter for Run II.

Each plug wedge spans 15° in azimuth, however from $1.1 < |\eta| < 2.11$ (37° to 14°) the segmentation in ϕ is doubled, and each tower spans only 7.5°. Figure 3.12 shows the plug tower geometry. Note that, in contrast to the central region, each plug tower is read out by a single phototube. The PEM is a lead-scintillator sampling calorimeter, approximately 21 X_0 in depth, and has an energy resolution of

$$\frac{\sigma(E)}{E} = \frac{16.0\%}{\sqrt{E_T}} \oplus 1\%.$$

The PHA is an iron-scintillator sampling calorimeter, approximately 7 λ_0 in

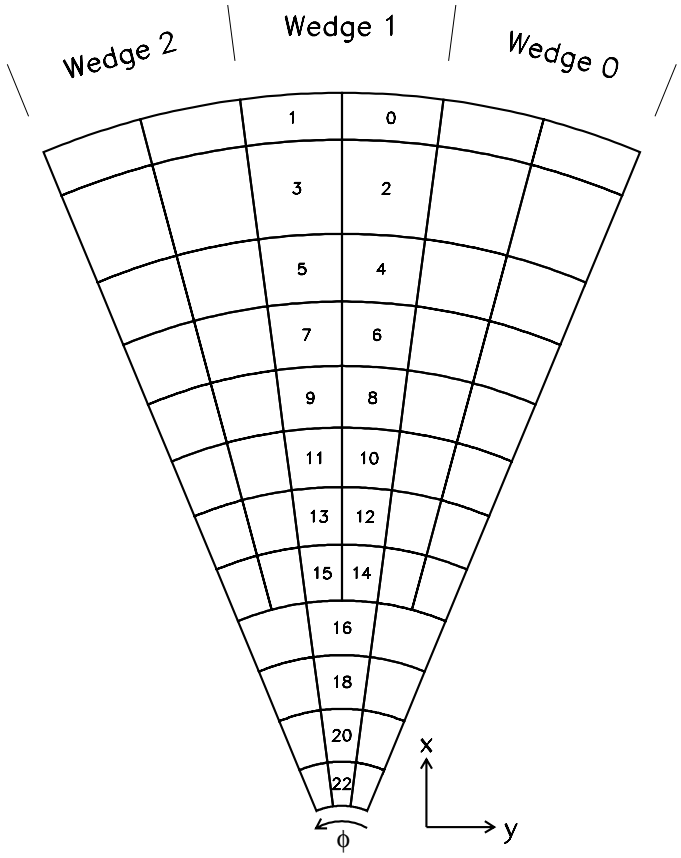

Figure 3.12: Tower geometry for the CDF Run II endplug calorimeters. Each wedge covers 15° in azimuth. As shown, towers 0–14 span the region $1.1 < |\eta| < 2.11$, and towers 16–22 span the region $2.11 < |\eta| < 3.6$.

depth, and has an energy resolution of

$$\frac{\sigma(E)}{E} = \frac{80.0\%}{\sqrt{E_T}} \oplus 5\%.$$

The PES shower-maximum detector is located about 6 X_0 deep within the PEM, and is constructed of two layers (denoted 'U' and 'V') of scintillating strips. The strips are 5 mm wide, and roughly square in cross-section. The PES is segmented into 45° sectors, with strips in the the U and V layers offset from the radial direction by +22.5° and −22.5° respectively. Position resolution of the PES is $\sim$ 1mm. There is also segmentation in pseudorapidity, with a low-η region ($1.13 < |\eta| < 2.60$) and a high-η region ($2.60 < |\eta| < 3.50$). Figure 3.13 shows a schematic layout of a PES 45° section. Fully assembled, an endplug calorimeter weighs over 100 tons, and must be readily movable to provide access to the COT and the silicon detectors; from start to finish, it takes about 4 hours to access and move one endplug, and provide a platform such that internal work can be performed. Table 3.1 shows a comparison summary of the central and endplug calorimeters for Run II.

3.2.4.3 Missing transverse energy

In practice we use the calorimeters to measure the missing energy as well as the deposited energy in an event. The quantity which can be defined is the missing tranverse energy, denoted by the symbol $\not\!\!E_T$. This quantity allows, for example, the "detection" of neutrinos, which are otherwise unobservable at CDF. A more detailed discussion of $\not\!\!E_T$ is included in section 4.5.

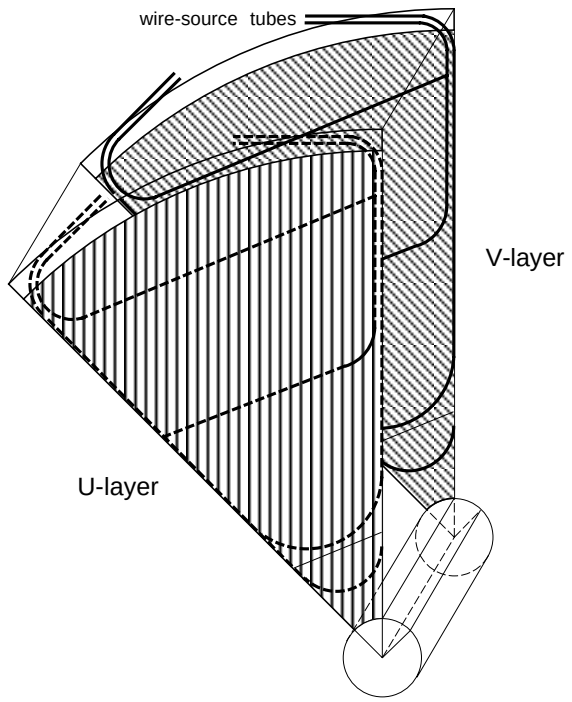

Figure 3.13: Schematic drawing of a 45° section of the PES detector. The segmentation into a low- and high-η region is shown. The PES is calibrated using a radioactive source, which traverses the indicated path during calibration and is retracted into a shielded box when not in use.

	Central	Plug
EM:		
Thickness	19 X_0, 1λ	21 X_0, 1λ
Sample (Pb)	0.6 X_0	0.8 X_0
Sample (scint.)	5 mm	4.5 mm
WLS	sheet	fiber
Light yield	160 pe/GeV	300 pe/GeV
Stoch. res.	$14.0\%/\sqrt{E_T}$	$16.0\%/\sqrt{E_T}$
Sampling res.	$11.6\%/\sqrt{E_T}$	$14.0\%/\sqrt{E_T}$
ShowerMax. seg. (cm)	$1.4\phi \times (1.6 - 2.0)z$	0.5 wide strips
Pre-shower size	$1.4\phi \times 65(z)$	by tower
Hadron:		
Thickness	4.5λ	7.0λ
Sample	1" C, 2" W	2 in. (Fe)
Sample (scint.)	10.0 mm	6.0 mm
WLS	finger	fiber
Light yield	$\sim$40 pe/GeV	30 pe/GeV

Table 3.1: A comparison of the central and endplug calorimeters for Run II. In the rows corresponding to light yield, photoelectrons is abbreviated as "pe."

3.2.5 Muon systems

In Run II there are four independent muon detectors: three covering the central region (CMU, CMP, CMX), and one covering further in pseudorapidity (IMU). The CMU and CMP detectors both cover approximately $|\eta| < 0.6$, and the CMX detector approximately $0.6 < |\eta| < 1.0$. The IMU detector was not fully integrated in time for this analysis, but will eventually provide triggerable coverage between $1.0 < |\eta| < 1.5$, and coverage suitable for muon identification from $1.5 < |\eta| < 2.0$. Figure 3.14 shows a plot of the effective muon coverage in $\eta - \phi$ space for this analysis. Each muon chamber contains a packed array of drift tubes, as illustrated in Figure 3.15, which form *stubs* from the trajectories of charged particles passing through the chamber. If a stub is matched to an extrapolated track, a muon is reconstructed in the CDF detector.

3.2.6 Trigger systems

For Run II, CDF employs a three-level trigger system to selectively capture interesting events. The levels are denoted simply as 'L1,' 'L2,' and 'L3,' with each subsequent level making more complicated decisions and requiring successively longer processing times. The crossing rate of the Tevatron under 36 on 36 bunch operation is 7.6 MHz, corresponding to 396 ns separation.

The L1 trigger operates with $5.5\,\mu$s latency to allow enough time for data transfer and decision making, implying that buffering capacity for 42 crossings must be built into the system in order for L1 to remain "deadtimeless." The L1 hardware is built using VME architecture, and receives information from the calorimeters, COT, and muon detectors as input to a L1 decision. The COT information is first processed by the 'XFT' (eXtremely Fast Tracker) before being

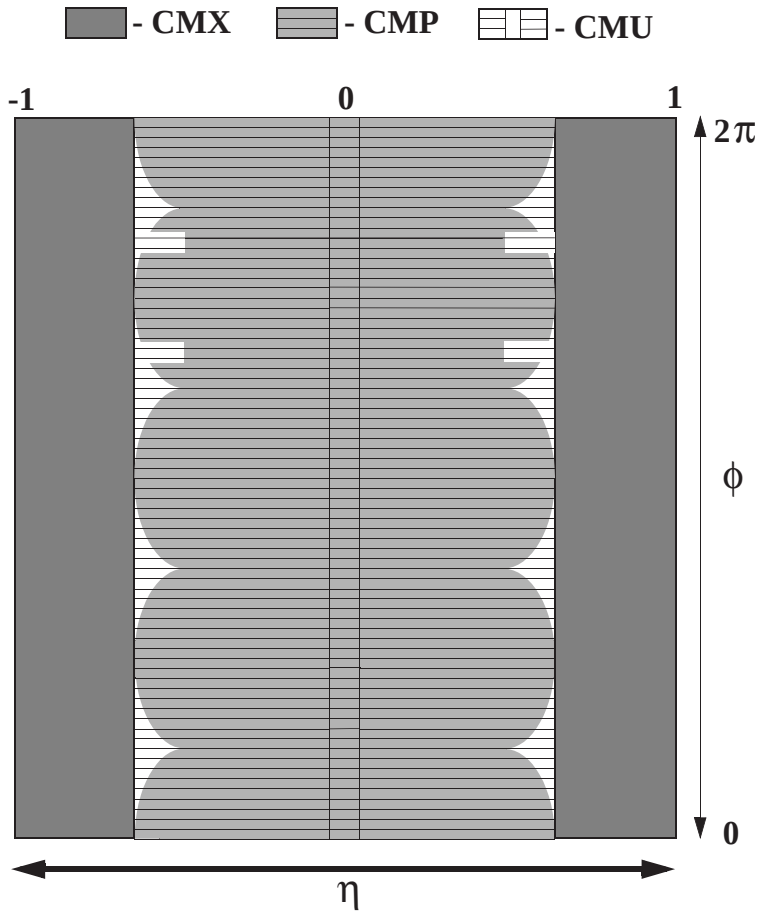

Figure 3.14: Map of the muon coverage for this analysis.

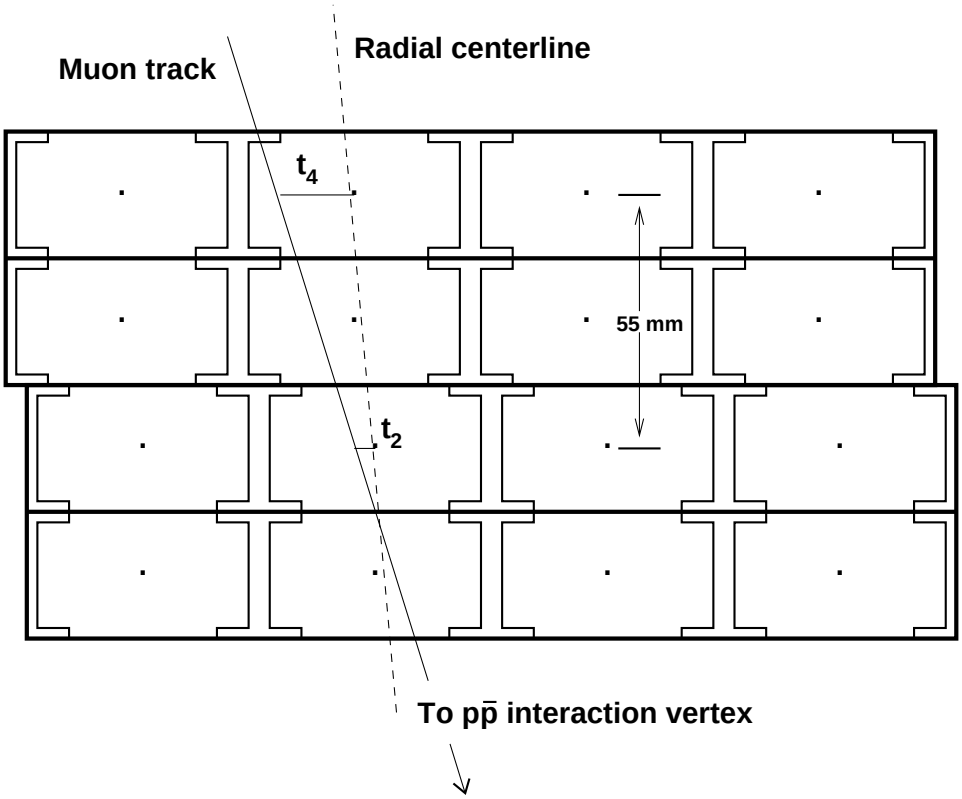

Figure 3.15: Cross-sectional view of drift tubes in a muon chamber. A stub is formed from the trajectory of a muon passing through the chamber, and the stub is matched to a track to become a reconstructed muon.

sent to the trigger, thus for the first time there is tracking information available at L1.

If an event is accepted at L1, it is transferred to one of four L2 buffers. The L2 trigger is thus also a buffered system, again based on VME architecture. It is designed to operate with an input rate of up to 40 kHz, while incurring no more than 10% deadtime. As input to a decision, L2 receives information from the calorimeters, muon detectors, COT, and also the silicon systems, via the 'SVT' (Silicon Vertex Tracker). The SVT input implies that CDF can trigger on displaced vertices, which has never been done before at a hadron collider.

The L3 trigger is software based, and is implemented using a farm of several hundred Linux CPUs. It features a maximum input rate of approximately 300 Hz, and uses the full event information to make a L3 decision. Data from L3 are monitored in real time by dedicated Linux PCs in the CDF control room. Events which pass the L3 trigger are sent to the Feynman Computing Center at a maximum rate of about 40 Hz. From there the data are written to tape and stored for further processing.

The logical flow of the trigger and data acquisition systems described above in the text is depicted graphically in Figure 3.16.

Having discussed the Fermilab accelerators and the CDF detector, we are now ready to describe how particles from the $p\overline{p}$ collisions are identified for physics analyses.

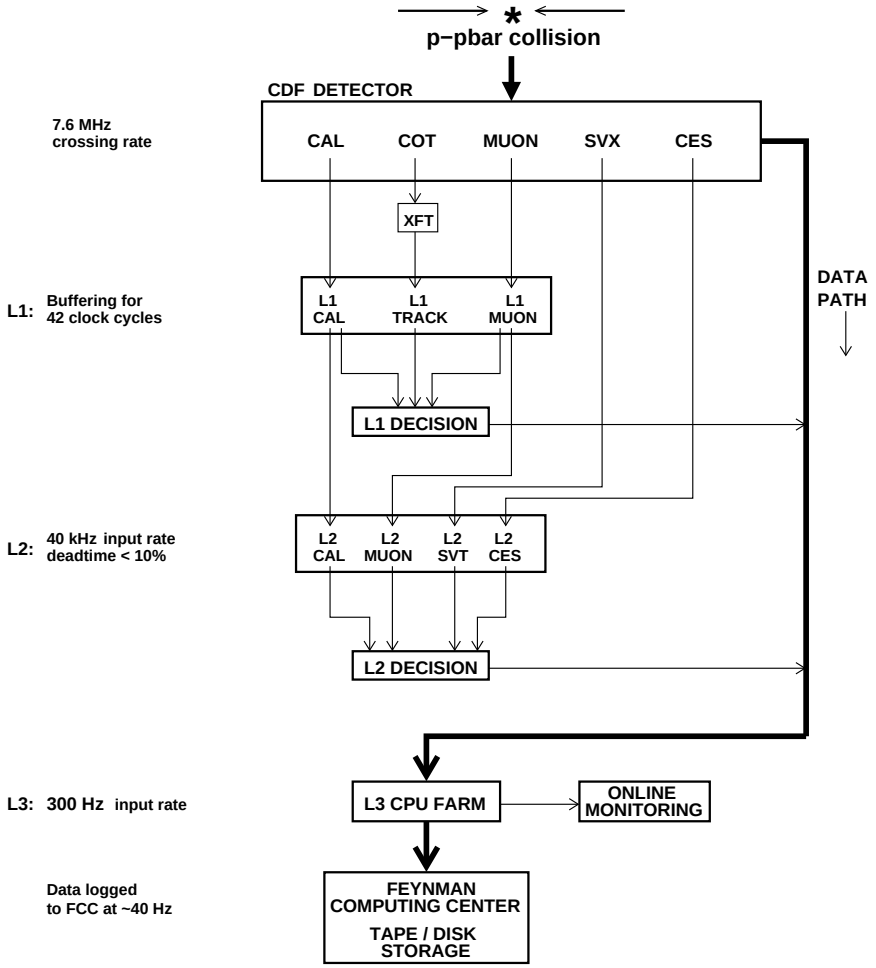

Figure 3.16: Block diagram of the Run II trigger system at CDF.

CHAPTER 4

Identification of leptons and jets

In this chapter we describe the identification of electrons, muons, and jets within the CDF detector. These definitions will be useful in understanding the primary data sets for the analysis and the full event selection for dilepton $t\bar{t}$ decays, which are described in the next chapter. Our efforts concentrated on developing plug electrons, and will be emphasized here.

4.1 Electrons in the endplug detectors

The work to develop plug electrons for Run II occurred in several steps over a time period of approximately two years. These studies are organized below into separate subsections.

4.1.1 Preliminary studies

Since the endplug detectors were completely redesigned and rebuilt for Run II, we started from scratch to develop the definition of a plug electron. To discern a useful set of identification variables, we obtained samples of test beam data, $Z \rightarrow e^+e^-$ Monte Carlo, and events from Run II data with at least one central electron passing the tight cuts listed below in section 4.2. The events from Run II data were additionally required to have an EM cluster in one of the end-

plugs which, when paired with the tight central electron (TCE), had an invariant mass close to that of a Z boson ($86 < M_{\ell\ell} < 97\,\mathrm{GeV}$). Enforcing these requirements provides a relatively pure sample of central/plug $Z \to e^+e^-$ events, where the plug clusters are unbiased since the parent data sample was selected using central electrons. We hand-scanned event dumps and event displays, and studied distributions from the three different samples to arrive at a calorimeter-based definition for plug electrons, which we will refer to as "PEM" electrons. These selection criteria are defined in section 4.1.2. Since adding tracks to plug electron ID can only be accomplished with the SVX and ISL detectors, which were not yet in a usuable state, we first pursued studies of the calorimeter-only definition.

To test the PEM electrons, we made a first pass measurement of the $W \to e\nu$ cross-section using only the endplugs [26]. During these studies we developed an ID variable using the plug shower maximum detector (PES). An analysis of plug test beam data (e^+) showed that the distribution of energy vs. strip for electrons in the U and V layers of the PES detector could be described by a Lorentzian, and that showers were contained transversely within a 9-strip region. These results are shown in Figure 4.1. The 9-strip cluster width corresponds to approximately one Molière radius[1]. When we examined the PES clusters in Run II data, however, we found broader PES clusters (less energy concentrated in the central few strips), and much more ragged structure in the tails. The large variations in transverse strip profile made it difficult to implement a Lorentzian fit for electron identification; we instead formed a simple ratio of the sum of the energy in the central 5 strips to the total energy of the 9-strip cluster. This ratio is essentially an isolation variable for PES clusters, and is applied independently to clusters

[1]The transverse development of electromagnetic showers can be described in terms of Molière radii: Approximately 90% (99%) of the energy of an EM shower will be contained within a cylinder of radius 1 R_M (3.5 R_M) centered on the shower axis [27].

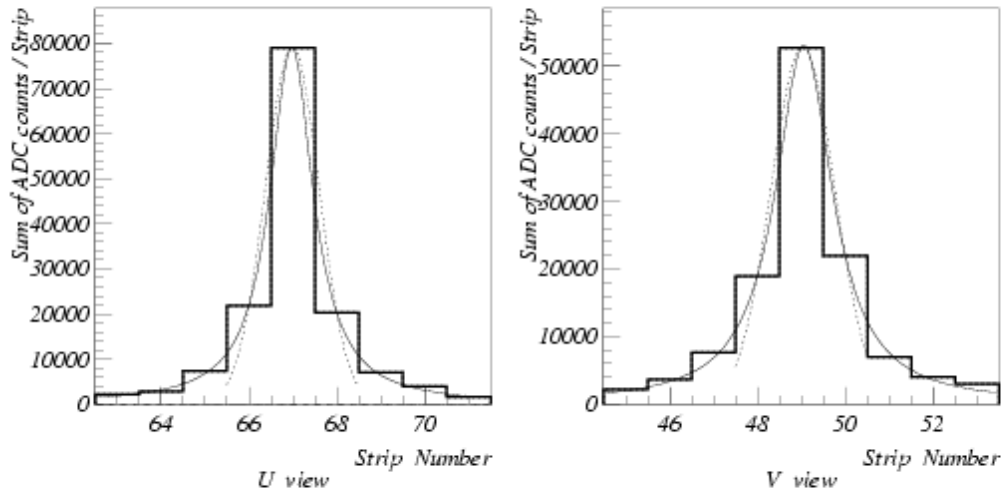

Figure 4.1: Average shower profile for test beam positrons incident on the U and V layers of the PES detector. The solid line is a 3-strip Lorentzian fit extrapolated to 9 strips; the dotted line corresponds to a Gaussian fit.

in both the U and V layers. The 5-strip numerator is robust with respect to the broad shape of the PES clusters, however the discriminating power of the variable to reject hadronic background is still reduced because of the broadened profile. Progress in understanding and correcting the source of the broadened clusters is discussed in section 4.1.7.

Using a Monte Carlo sample of $W \to e\nu$ events, we estimated the detector acceptance as a function of the E_T requirement placed on the reconstructed EM cluster. We selected a requirement of $E_T > 20$ GeV to provide rejection of low-energy hadronic background while maximizing the kinematic acceptance for electrons from W decays. Comparing generated and reconstructed particles, we measured an efficiency to reconstruct an electron in the endplugs of $\sim 96\%$. Including this efficiency, we obtained an acceptance of $(22.7 \pm 3.0)\%$ for a kinematical requirement of $E_T > 20$ GeV and an implicit fiducial requirement of

$1.2 < |\eta| < 2.11$. We measured the efficiency of the PEM identification variables using a procedure similar to that discussed in section 4.1.3, and obtained an overall efficiency of $(77.0 \pm 3.4)\%$. We searched for $W \to e\nu$ events in a sample of $8.67\,\mathrm{pb}^{-1}$ of data. Applying the PEM selection criteria reduced the number of events from 267,888 to 7,604. Because of the limited number of available samples of Monte Carlo and data events, we estimated the background contamination in our signal sample by analyzing a set of two-dimensional plots of identification variables. Each plot is divided up into four regions ("boxes" labeled A, B, C, and D), as shown in Figure 4.2, and the number of background events in the signal region, box C, is estimated as $A \cdot (D/B) = 2794 \pm 363$ events. Our ability to estimate the background fraction using this method was hampered because of poor statistics, which may have been responsible for some inconsistent estimates between several of the two-dimensional plots we analyzed. To calculate the cross-section times branching ratio we used the following definition

$$\sigma \cdot B(W \to e\nu) = \frac{\mathrm{N_{sig}} - \mathrm{N_{bgd}}}{\epsilon_{id} \cdot Acceptance \cdot \int \mathcal{L}\, dt}.$$

We obtained a measured value of (3.26 ± 0.61) nb, where the error is statistical only. The latest NNLO theoretical prediction is (2.731 ± 0.002) nb.

Since the PEM electrons do not have associated tracks, we expect that samples of events selected using *only* the PEM criteria will exhibit a larger background contamination than other leptons. When adding plug electrons to a $t\bar{t}$ measurement, however, one has many other selection criteria to apply, which should greatly reduce the background fraction. To determine whether the PEM electrons would be suitable for a measurement of the $t\bar{t}$ cross-section, we tested the definition directly in that context by performing preliminary studies of the signal and background contributions from PEM electrons to the analysis as a

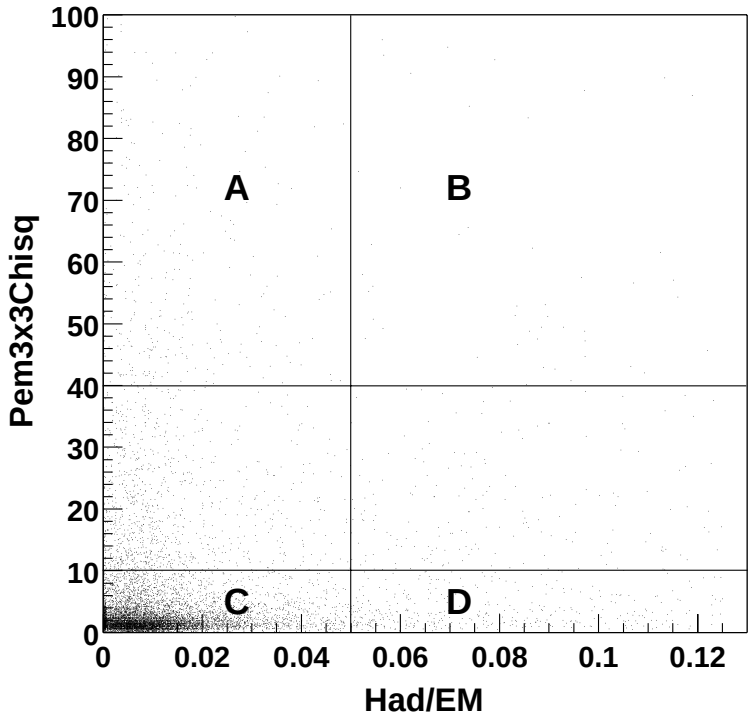

Figure 4.2: A distribution illustrating the method used to estimate the background fraction in the $W \to e\nu$ cross-section measurement using PEM electrons. Here *pem3x3Chisq* vs. *Had/EM* is shown, with all other selection requirements applied. The number of background events in the signal region, box "C," is estimated as the product $A \cdot (D/B)$.

whole. We estimated the relative contributions to the acceptance and physics background processes (WW, $Z \to \tau^+\tau^-$) using Monte Carlo samples, and studied side bands to the signal region using events from Run II data to estimate the fake background from QCD processes. (These background studies are mentioned here simply to give a flavor for the validation process we followed. The background estimates for the actual analysis are described in chapter 6.) These studies showed that the event topology associated with dilepton $t\bar{t}$ decays is sufficiently rare that PEM electrons could be included, and would provide a large gain in acceptance

for a relatively small loss in purity.

Concurrent with these studies, a new approach to tracking in the plug region, "Phoenix" tracking, became available [28]. The Phoenix algorithm improved the tracking efficiency for $|\eta| > 1.1$ by using position information from the endplug calorimeters to aid the silicon pattern recognition code: One constraining endpoint for a track is taken using the interaction vertex, and the other from the PES position of an EM shower. The calorimeter energy of the corresponding PEM cluster is taken as the momentum, which provides a curvature (unsigned). Since two points plus a curvature determine a unique helix, this is sufficient to create two hypothetical track trajectories, one for each possible charge. The algorithm uses these trajectories as input and reruns the silicon pattern recognition code. If neither of the tracks can be reconstructed, the algorithm finishes without appending a track to the event record. If only one of the tracks can be reconstructed, it is appended to the event record as a Phoenix track. If both tracks can be reconstructed, the algorithm calculates two $\chi^2_{/dof}$ values which quantify the goodness of fit with respect to each hypothetical $(+/-)$ trajectory[2]. The algorithm selects the track (signed) corresponding to the lower $\chi^2_{/dof}$ as the best match, and appends it to the event record as a Phoenix track. If a PEM electron has an associated Phoenix track, it is promoted to a "Phoenix plug electron," which we refer to as "PHX" henceforth.

4.1.2 Plug ID variables for the $t\bar{t}$ cross-section analysis

For the $t\bar{t}$ cross-section measurement we retain both PEM and PHX electrons because the Phoenix tracking efficiency is still low compared with the COT effi-

[2]A better goodness of fit measure would be a function, $P(\chi^2, dof)$, which estimates the probability of obtaining that χ^2 value given the number of degrees of freedom.

ciency. Below we define the variables used to identify PEM and PHX electrons, and list the associated cut values in Table 4.1.

$\mathbf{E_T}$ The transverse energy of an electromagnetic cluster in the PEM calorimeter. $E_T = E \times \sin\theta$. Although energy is a scalar, we create a two-dimensional vector definition because it is often convenient experimentally to work with quantities defined in the plane perpendicular to the beam axis.

Had/EM The ratio of the hadronic energy to the electromagnetic energy of a given cluster in the calorimeter.

Isolation energy The sum of the energy in the calorimeter (Had+EM) in a cone of radius ($\Delta R = \sqrt{(\Delta\eta)^2 + (\Delta\phi)^2}$) surrounding a given cluster (excluding the energy of the cluster itself). Unless otherwise noted, a cone size of $\Delta R = 0.4$ is implied for isolation variables. In practice we enforce a requirement on the isolation ratio:

$$\text{Isol} = \frac{\text{Isolation}\, E_T\, (0.4\,\text{cone})}{\text{EM}\, E_T}.$$

Pem3x3Chisq An algorithm which compares the electromagnetic shower profile of a given PEM cluster to shapes derived from test beam data.

PesProfileRatio5by9 A simple ratio formed using PES clusters which is essentially an isolation variable for the shower maximum detector:

$$\frac{\text{Sum of the energy in the central 5 strips of a PES cluster}}{\text{Sum of the energy in (all) 9 strips of a PES cluster}}$$

It is applied separately to both layers (U and V) of a PES 2-d cluster.

Plug fiducial region In the endplugs, the fiducial region we define spans a

Variable	PEM cut value	PHX cut value
E_T	> 20.0 GeV	> 20.0 GeV
fiducial	$1.2 < \|\eta_{PES}\| < 2.5$	$1.2 < \|\eta_{PES}\| < 2.5$
$\frac{leakage-corrected\,Isolation\,E_T\,(0.4\,cone)}{EM\,E_T}$	< 0.1	< 0.1
Had/EM	< 0.05	< 0.05
pem3x3FitTowers$\neq 0$	yes	yes
χ^2_{PEM3x3}	< 10.0	< 10.0
pesProfileRatio5by9 (U & V layers)	> 0.65	> 0.65
$\Delta R_{(pem3x3Fit\,\text{coords.}-\text{PES coords.})}$	< 3.0 cm	< 3.0 cm
Si track (Phoenix track)		yes
$\|z0_{\text{track}}\|$		< 60 cm
$\Delta R_{(\text{track}-\text{PES})}$		< 3 cm

Table 4.1: Plug electron ID cuts. *Si track* implies a 2-d Phoenix track.

range in pseudorapidity of $1.2 < |\eta| < 2.5$. The region $|\eta| < 1.2$ is excluded because of the geometry of the PES detector, which does not provide useable coverage there. We exclude the region $|\eta| > 2.5$ primarily because the rate of increase in the acceptance falls rapidly with repect to the increase in background at high pseudorapidity.

ΔR The matching distance between the Pem3x3Fit coordinates (returned by the Pem3x3Chisq algorithm) and the PES coordinates of a given PEM cluster. To guard against failures in the Phoenix tracking algorithm, a ΔR matching requirement is also enforced between the PES coordinates and the extrapolated Phoenix track.

4.1.3 PEM electron ID efficiencies

To determine efficiencies for the PEM electron ID variables we use cen-

tral/plug Z events from Run II data. We start from a common CDF data sample of events which have at least one tight central electron (TCE), and apply the official "good run" list for summer 2003 conferences. The good run list is created by detector experts and operations personnel, and ensures that the detector was properly calibrated and functioning well during the specified runs. The event selection is as follows:

- Require that the TCE additionally satisfy tighter requirements than those listed in section 4.2 ($Lshr < 0.1$, $Isol < 0.05$) to further reduce background.
- Require a fiducial plug EM cluster ($1.2 < |\eta| < 2.5$) with $E_T > 20$ GeV.
- Require that the central and plug clusters have an invariant mass consistent with that of a Z boson, ($81 < M_{Inv} < 101\,\mathrm{GeV}$).

Applying these selection criteria yields a sample of 4,041 events which are used to estimate the efficiencies. Figures 4.3 and 4.4 show distributions of the variables; Table 4.2 summarizes the results. Uncertainties are calculated using binomial statistics. The overall efficiency of the ID cuts is measured to be $(84.3 \pm 0.6)\%$.

4.1.4 PEM ID efficiency scale factor

Monte Carlo samples currently available at CDF do not model the data well enough such that differences can be ignored. We determine a relative scale factor between data and Monte Carlo which will be applied to the acceptance and Monte Carlo-based background estimates. Although the background contamination in our central/plug Z sample is very small, the procedure to measure the efficiencies described here does not subtract background; to obtain the final scale factor, we use a background subtracted plug ID efficiency (0.877 ± 0.051) calculated

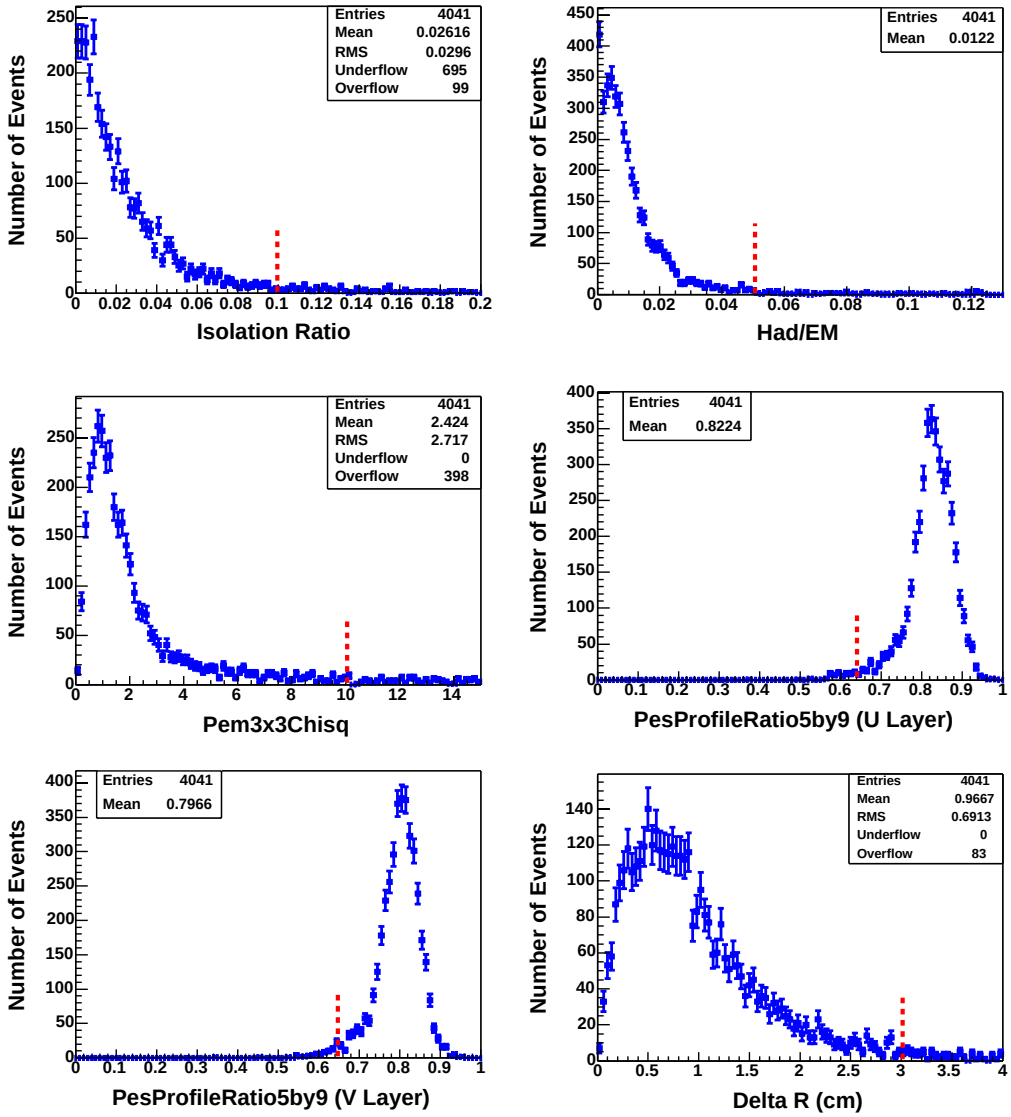

Figure 4.3: Distributions of the plug electron ID variables for the candidate central/plug Z events. For these plots none of the cuts (indicated by the dashed vertical lines) have been applied.

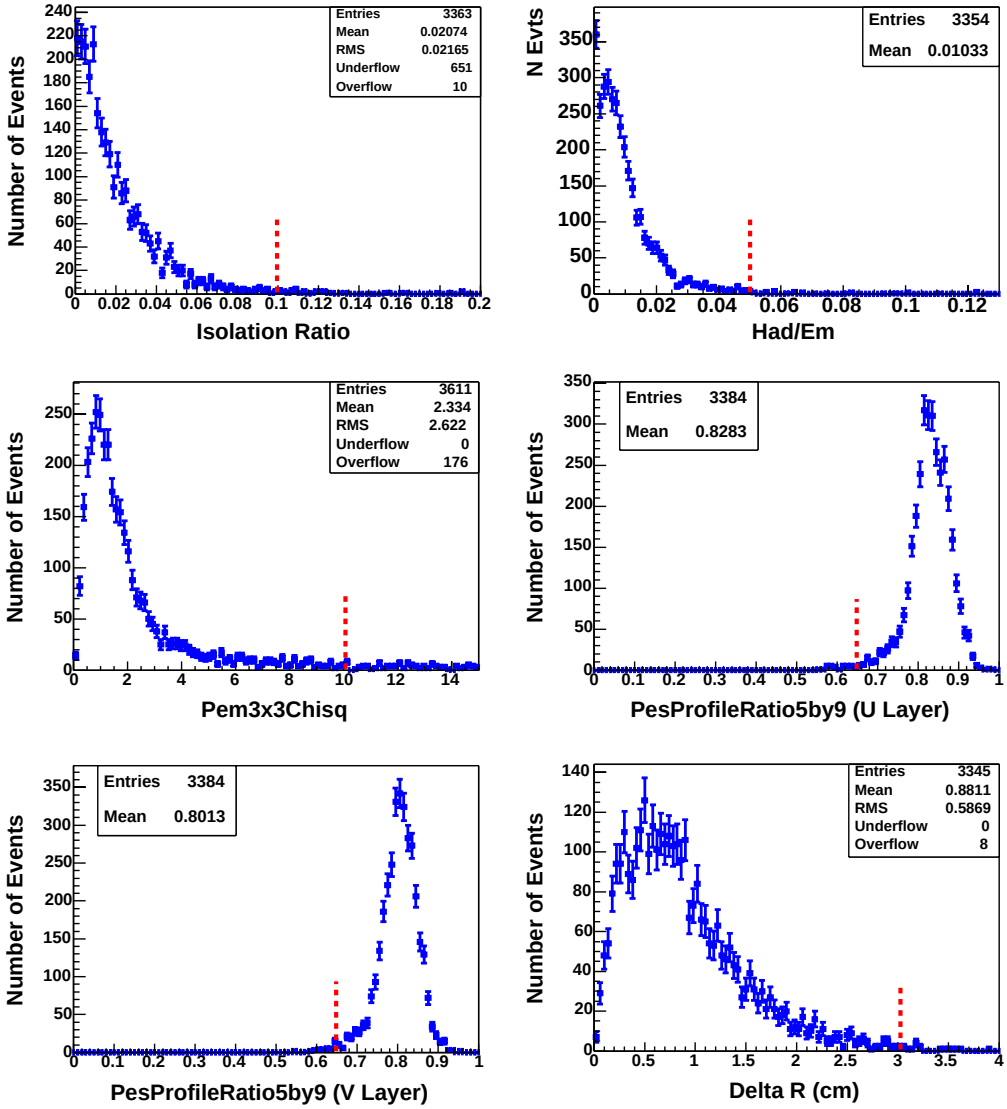

Figure 4.4: 'N-1' distributions of the plug electron ID variables for the candidate central/plug Z events. Cut values are indicated by the dashed vertical lines.

Variable and cut value	Eff. [%] each cut *only*	Eff. [%] 'N-1'
$\frac{Isolation\ energy\ (\text{cone of } 0.4)}{EM\ E_t} < 0.1$	96.0 ± 0.4	98.7 ± 0.2
$Had/EM < 0.05$	97.3 ± 0.4	98.9 ± 0.2
$pem3x3Chisq < 10.0$	89.2 ± 0.7	91.9 ± 0.4
$pesProfileRatio5by9 > 0.65$ (U & V layers)	97.1 ± 0.4	98.0 ± 0.2
$\Delta R_{pem-pes} < 3.0$ cm	96.6 ± 0.4	99.2 ± 0.1
Overall efficiency: $(84.3 \pm 0.6)\%$		

Table 4.2: Efficiencies of plug electron ID variables. Here 'N-1' implies all other cuts have been applied *except* the cut in question. The uncertainties are statistical only.

in a recent CDF measurement of the Z boson cross-section [29]. Figure 4.5 summarizes the results. The average scale factor is found to be 0.96 ± 0.05.

4.1.5 Background rejection

To estimate the background rejection of the PEM electron ID variables we use events from official QCD data sets. These data samples contain primarily dijet events where at least one jet has $E_T > 20$ GeV. The good run list is applied. The event selection is as follows:

- Require at least one central jet ($|\eta| < 1.0$) with $E_T > 25$ GeV to satisfy the trigger requirements.
- Require a fiducial plug ($1.2 < |\eta| < 2.5$) EM cluster with $E_T > 20$ GeV.
- Require $\not\!\!E_T < 15.0$ GeV to remove real electrons from leptonic W boson decays[3], and veto electrons from leptonic Z decays by requiring that the

[3]We received a comment [30] that requiring $\not\!\!E_T < 15.0$ GeV in a sample which is overwhelmingly dominated by hadronic activity could be causing a bias, because it is essentially a

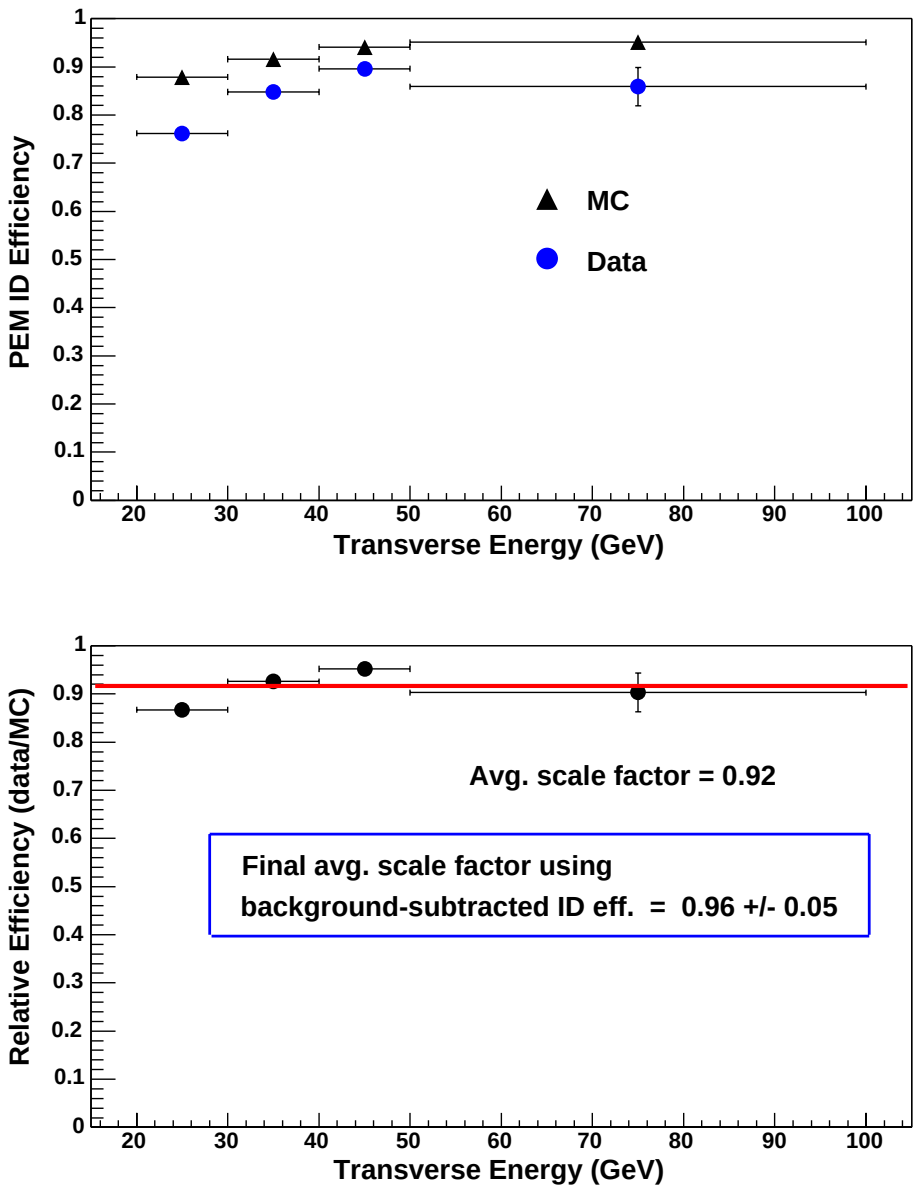

Figure 4.5: Plug ID variable efficiency and relative efficiency (data/MC) vs. E_T. Note that a background subtracted ID efficiency (see text for reference) is used to compute the average scale factor which is used in the analysis (0.96 ± 0.05).

Variable and cut value	Additional rejection [%] (see caption)
$\frac{total\ isolation\ (\text{cone of } 0.4)}{EM\ E_t} < 0.1$	50.0
$Had/EM < 0.05$	48.8
$pem3x3Chisq < 10.0$	69.6
$pesProfileRatio5by9 > 0.65$ (U & V layers)	32.3
$\Delta R_{pem-pes} < 3.0$ cm	$4.5^{\dagger}$
$\frac{\#\ passing all ID cuts}{total\ \#\ of\ candidate\ events}$: $(1.9 \pm 0.4)\%$	

Table 4.3: Background rejection of plug electron ID variables. † For completeness the numbers for the ΔR variable are included; there are implicit cuts on ΔR in the electron reconstruction code which obscure the effect of this cut. 'Additional rejection' is computed at N-1 and implies:
#(N-1) ≡ # of evts passing all cuts but the one in question.
#(N) ≡ # of evts passing all cuts.
The value listed is then: [#(N-1) - #(N)] / [#(N-1)]

invariant mass, in combination with any other EM cluster in the event, does not fall within the window ($76 < M_{Inv.} < 106$ GeV).

Applying these selection criteria yields a sample of 1,153 events which are used to estimate the additional background rejection afforded by each variable (calculated at N-1), and the overall background rejection when all ID requirements are applied. Figures 4.6 and 4.7 show distributions of the variables; Table 4.3 summarizes the results. The number of background events passing all ID cuts is measured to be $(1.9 \pm 0.4)\%$.

4.1.6 Validation of PHX electrons

To validate the PHX plug electrons, we measure $\sigma \cdot B(W \rightarrow e\nu)$ and $\sigma \cdot B(Z \rightarrow$

requirement that the jets be well measured. This is a good observation; the effects of varying (and removing) the $\not\!\!E_T$ cut were studied, and the results appear to be insensitive to the choice of the $\not\!\!E_T$ cut.

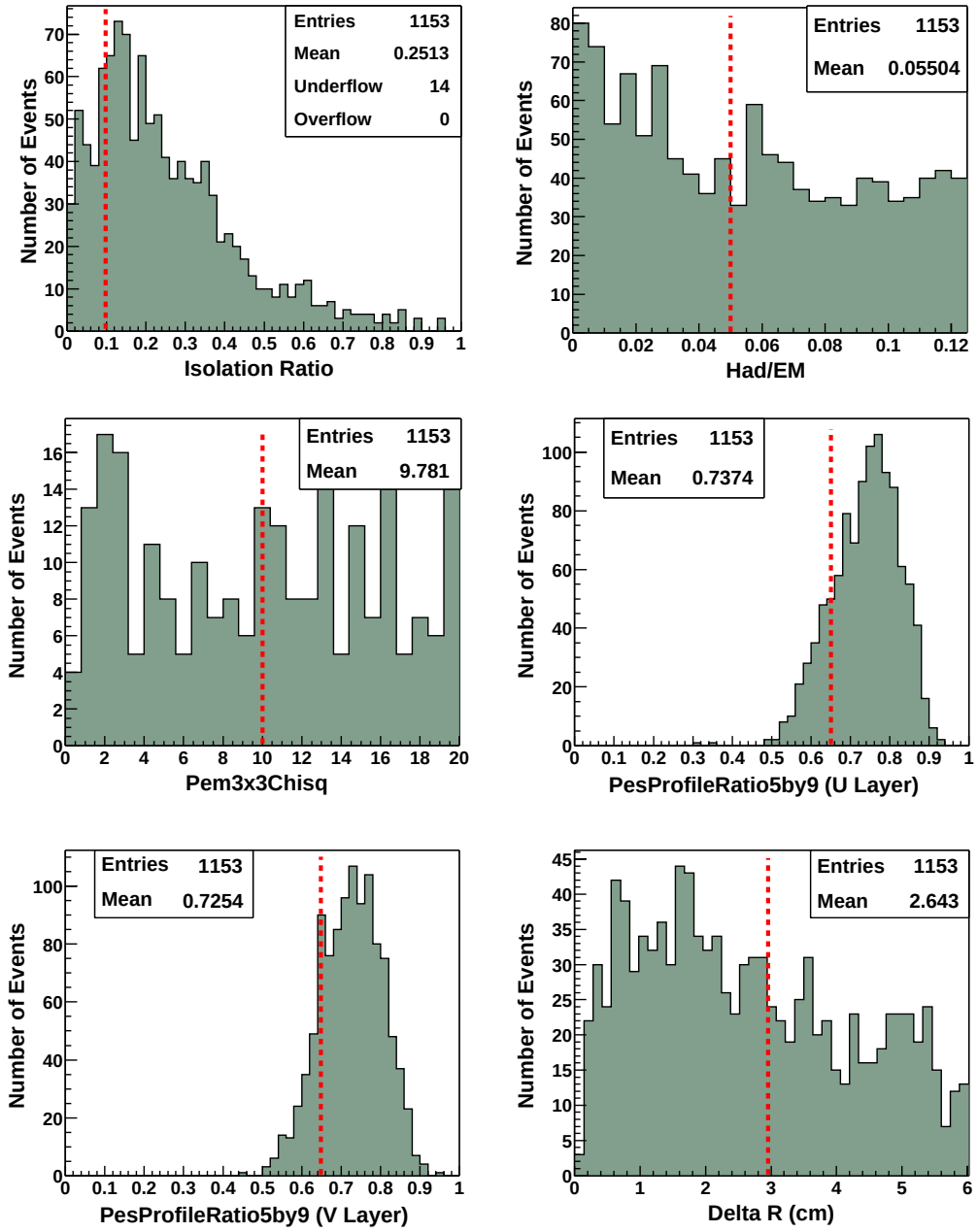

Figure 4.6: Distributions of the plug electron ID variables for background (QCD jets) events. In these plots none of the cuts(indicated by the dashed lines) have been applied.

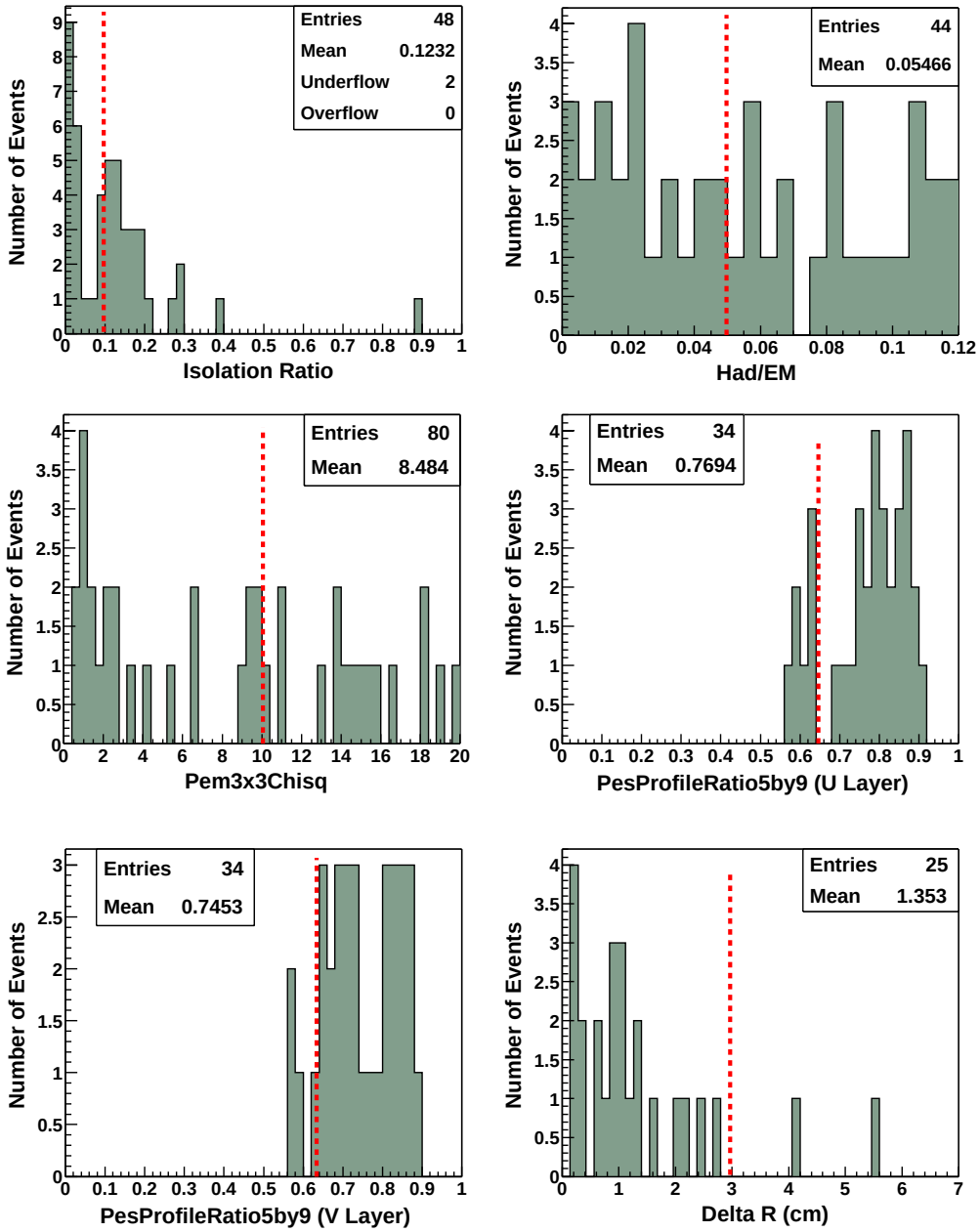

Figure 4.7: 'N-1' distributions of the plug electron ID variables for background (QCD jets) events. Cut values are indicated by the dashed lines.

e^+e^-) using events in an official plug data set. These measurements are performed to build confidence that the PHX plug electrons are suitable for use in a measurement of the $t\bar{t}$ cross-section.

4.1.6.1 Plug W cross-section

To select $W \to e\nu$ events we require a PHX plug electron, and additionally require $\not\!\!E_T > 25$ GeV. No back-to-back requirement is made on the ϕ angle between the electron and the $\not\!\!E_T$ because the endplugs do not have significant cracks in azimuthal coverage as exist in the CEM detector[4]. After applying these requirements 20,215 W candidates remain. We estimate the background fraction to be 3.5% (707 events) [31]. The acceptance is estimated to be 0.16 using an official $W \to e\nu$ Monte Carlo data set. We measure a relative scale factor between data and Monte Carlo for PHX plug electrons of 0.986; Figure 4.8 shows distributions used in this calculation. We use a value for the trigger efficiency taken from a recent CDF measurement [32]: ($\epsilon_{trig} = 0.874$). The integrated luminosity used in the calculation of the cross-section is 57.5 pb^{-1}. Figure 4.9 shows distributions of the electron E_T, $\not\!\!E_T$, and transverse mass. Using the following definition,

$$\sigma \cdot B(W \to e\nu) = \frac{\mathrm{N_{sig}} - \mathrm{N_{bgd}}}{\mathcal{A}_{total} \cdot \int \mathcal{L}\, dt},$$

the measured cross-section is (2.46 ± 0.25) nb, in good agreement with the latest NNLO theoretical prediction of (2.731 ± 0.002) nb [33] and a recent CDF measurement of (2.64 ± 0.18) nb [34].

[4]This cut was shown to have little effect for measuring W electrons in the endplugs in our preliminary analysis of the $W \to e\nu$ cross-section [26].

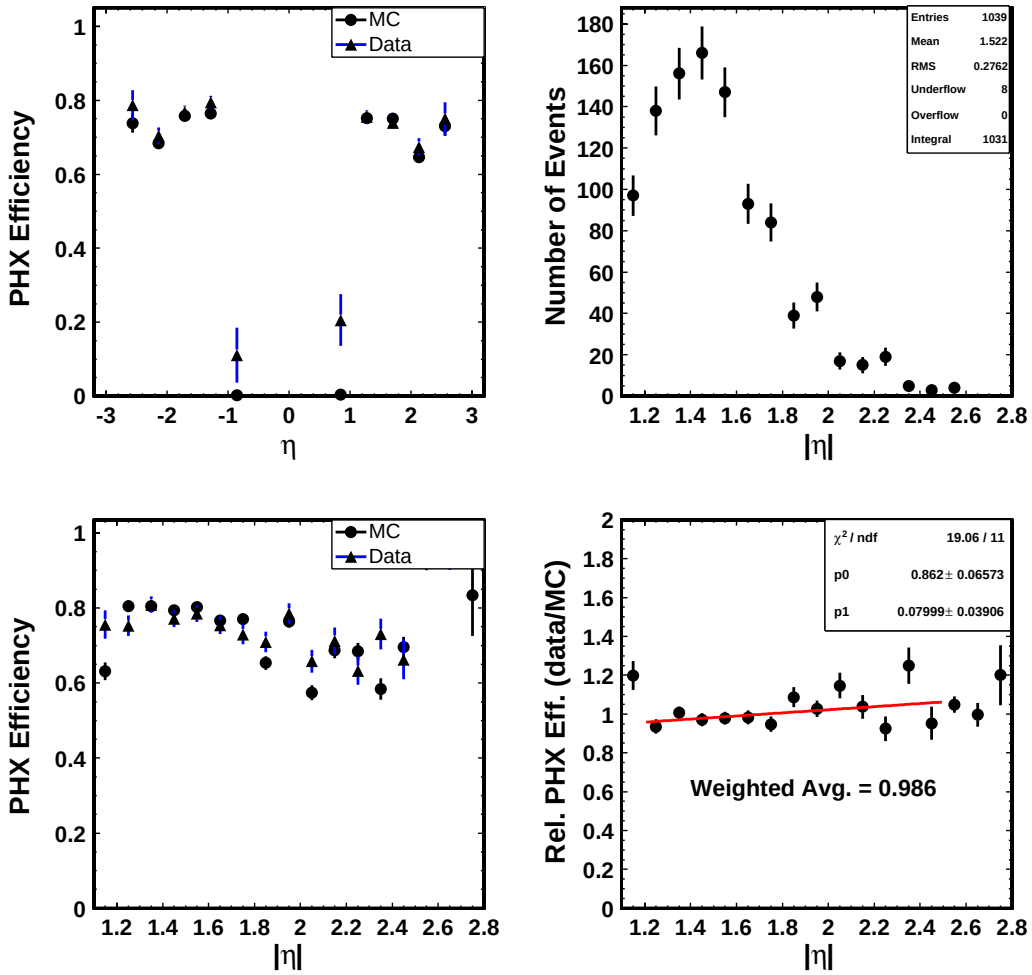

Figure 4.8: Distributions used in the determination of the data/Monte Carlo scale factor for PHX plug electrons.

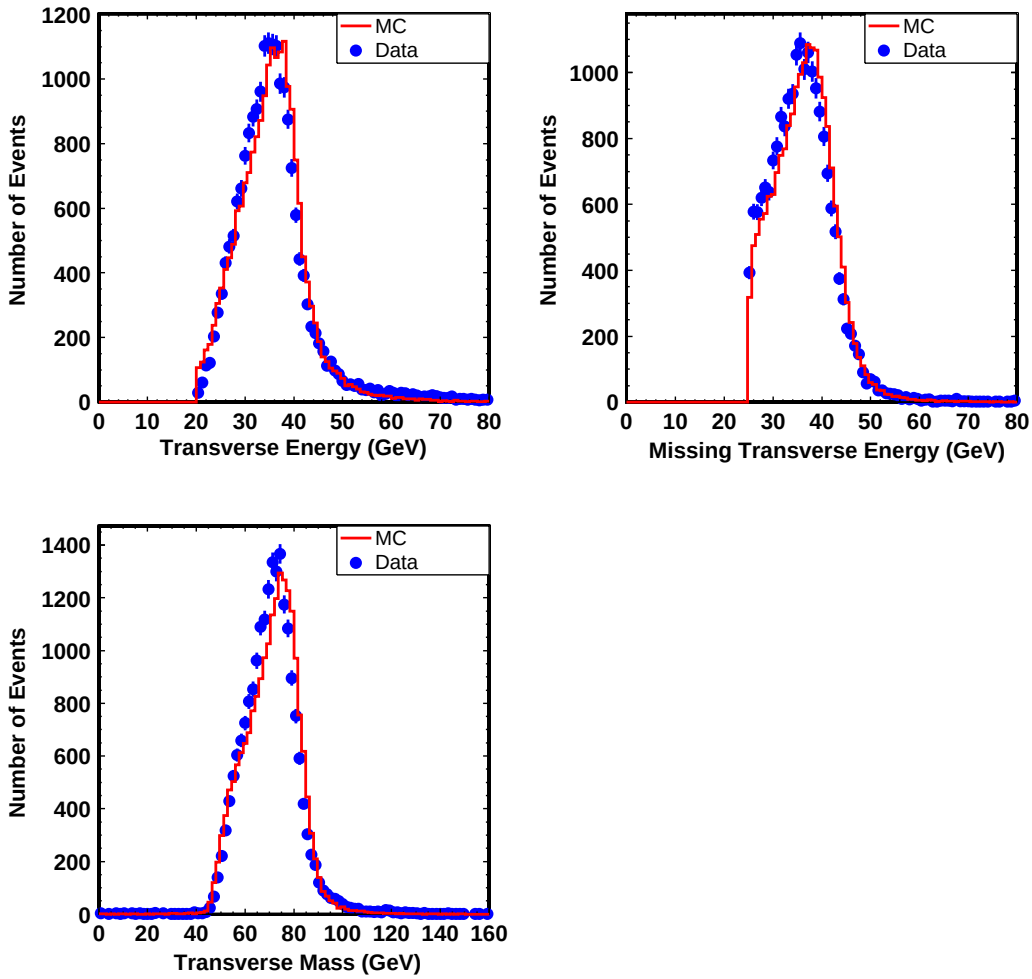

Figure 4.9: Distributions of electron E_T, $\not{E}_T$, and transverse mass from our W boson cross-section measurement using PHX plug electrons.

4.1.6.2 Plug/plug Z cross-section

To select $Z \to e^+e^-$ events, we require two PHX plug electrons which have an invariant mass between 81 and 101 GeV. After applying these requirements 578 candidates remain. We estimate backgrounds using numbers from a recent CDF measurement of the Z cross-section [35], and scale according to the number of observed events. The predicted backgrounds are 13 events (QCD fakes), 2.4 events (W's), 0.5 events ($Z \to \tau^+\tau^-$). The acceptance is estimated to be 0.04 using an official $Z \to e^+e^-$ Monte Carlo data set. We apply a relative scale factor between data and Monte Carlo of $0.986^2 = 0.972$, as described in the previous subsection. The trigger efficiency is calculated as $(1-(1-0.874)^2) = 0.984$. The integrated luminosity used in the calculation of the cross-section is 57.5 pb^{-1}. Figure 4.10 shows distributions of the electron E_T and invariant mass. Using the following definition,

$$\sigma \cdot B(Z \to e^+e^-) = \frac{\mathrm{N_{sig}} - \mathrm{N_{bgd}}}{\mathcal{A}_{total} \cdot \int \mathcal{L}\, dt},$$

the measured cross-section is (248.4 ± 25.0) pb, in good agreement with the latest NNLO theoretical prediction of (250.5 ± 3.8) pb [33] and a recent CDF measurement of (260.9 ± 18.2) pb [36].

4.1.7 Future improvements to the PES ratio variable

Currently we use only one quality variable involving the PES detector for plug electron ID. This is the *pesProfileRatio5by9* variable, described in section 4.1.1. Because of the broader than expected PES clusters currently observed, the variable is optimized using studies with central/plug Z events from Run II data, and the requirement on the ratio (> 0.65) is set to maintain a high signal

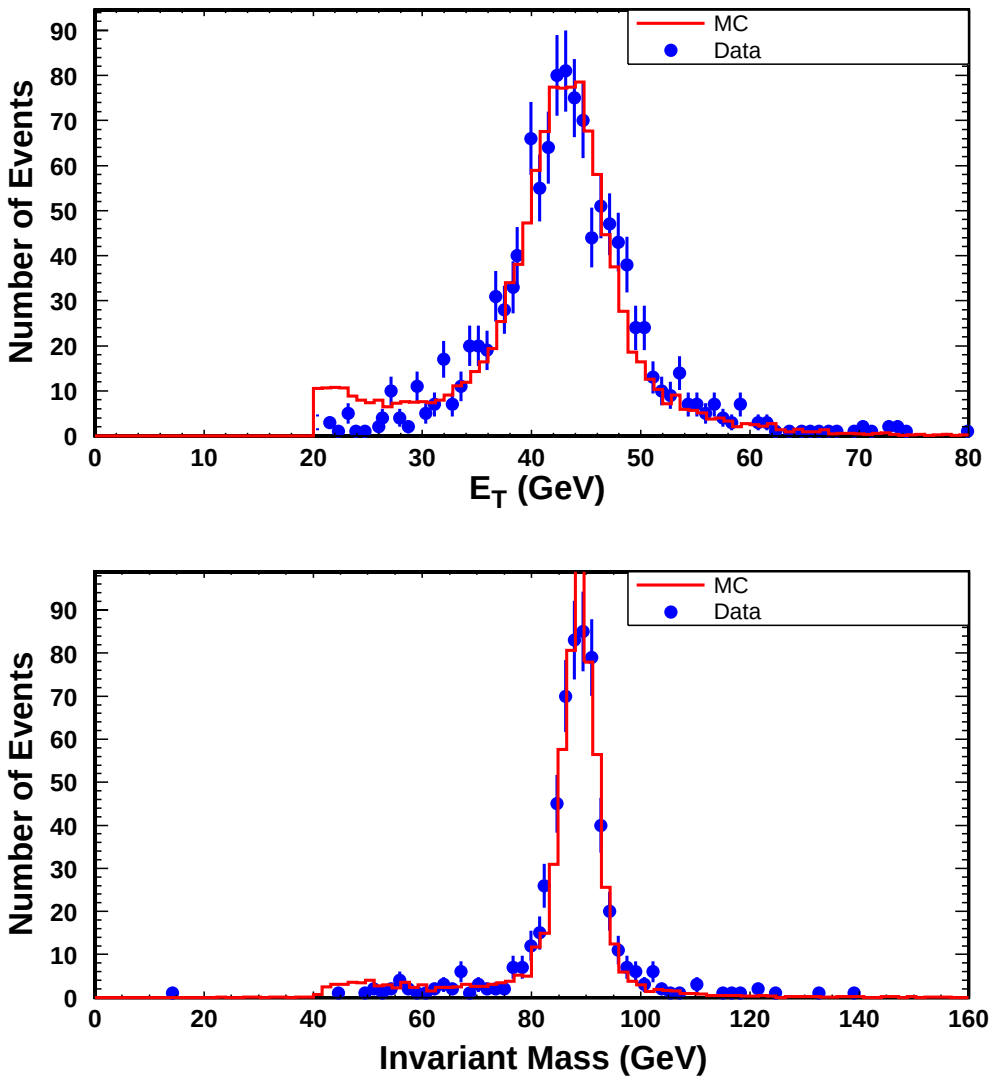

Figure 4.10: Distributions of electron E_T and invariant mass from our plug/plug Z cross-section measurement.

efficiency. The resulting background rejection afforded by the variable is not as large as many of the other plug electron ID variables (*eg.* Had/EM, Isolation). Recently, the cause of the broad PES clusters was understood to be a hardware problem which produces increased optical cross-talk between neighboring channels in the PES multianode phototubes [37]. Work was performed during the recent (September – November, 2003) shutdown in an effort to reduce this cross talk; preliminary indications are that the efforts were successful. The definition of the PES ratio variable will have to be revisited, and the cut value reoptimized, to realize any possible gains for electron identification. The reduced cross-talk may also improve the prospects for implementing a Lorentzian fit to PES clusters.

4.2 Electrons in the central detector

Since the central calorimeter is essentially unchanged for Run II, much of the knowledge accumulated in Run I regarding electrons in the central region can be directly applied here. The variables used for identifying central electrons have been extensively studied within the Run II framework [38]. We therefore forego a discussion of efficiencies and simply define the variables and associated cut values below. Variables which have the same definition as that given in the previous section on plug electrons (E_T, *Had/EM*, *Isolation*) will not be defined again here.

$\mathbf{p_T}$ The transverse momentum of a track in the COT. $p_T = p \times \sin\theta$. Because of the axial field, the component of momentum in the plane perpendicular to the beam axis is the quantity measured by the tracker.

E/p The ratio of the CEM energy of a cluster to the momentum of a given track.

z0 The location in z of the intersection between a track and the beam axis.

Lshr The lateral shower profile of a CEM cluster. This variable compares the energy in the seed tower of a cluster to the energy in the adjacent towers, and quantifies the degree to which a given shower profile is like that measured from test beam electrons [39]:

$$L_{shr} = 0.14 \cdot \frac{\sum_i \left(E_i^{obs} - E_i^{exp}\right)}{\sqrt{\left(0.14\sqrt{E_{EM}}\right)^2 + \sum_i \left(\Delta E_i^{exp}\right)^2}},$$

where the sum is over towers adjacent to the seed tower in the same wedge, E_{EM} is the total electromagnetic energy of the cluster, the $(0.14\sqrt{E_{EM}})$ term is from calorimeter energy resolution, and the $(\Delta E_i^{exp})^2$ term is the uncertainty in the expected energy.

Δx and Δz The distance in the $r - \phi$ (Δx) and $r - z$ (Δz) planes between the CES cluster position and that of a COT track extrapolated to the CES detector.

$\chi^2_{\mathbf{strip}}$ The χ^2 of a comparison between the CES z-strip shower profile of a given shower and that from test beam.

Table 4.4 lists the specific cut values used with these variables. Note that both "tight" and "loose" sets of central electron ID requirements are defined for analyses at CDF; in this analysis we use only the tight requirements.

4.3 Muons

The situation for central muons in Run II is similar to that of central electrons. Muon identification has also been extensively studied and validated within the Run II framework [40]. We therefore forego a discussion of efficiencies and simply

Variable	Cut value
E_T (2-tower EM sum$\times \sin\theta_{track}$)	> 20.0 GeV
Track P_T (COT-only beam-constrained track)	> 10.0 GeV
E/P (for $E_T < 50.0$ GeV only)	< 2.0
$\lvert z0_{track}\rvert$	< 60.0 cm
Had/EM	$< 0.055 + 0.00045 \times (E/\text{GeV})$
$\frac{leakage-corrected\,Isolation\,E_T\,(0.4\,cone)}{Em\,E_T}$	< 0.1
$Lshr$ (using track-based CES cluster, $z0_{track}$)	< 0.2
charge-signed Δx	$-3.0 < Q_{trk} * \Delta x < 1.5$ cm
$\lvert\Delta z\rvert$	< 3.0 cm
χ^2_{strip}	< 10.0
Track type	PADtrack
Fiduciality	($\lvert x_{CES}\rvert < 21.0$ cm, $9.0 < \lvert z_{CES}\rvert < 230.0$ cm, Tower 9 excluded, Most of tower next to chimney included)
COT Track quality	3 axial & 3 stereo SL with ≥ 7 hits each

Table 4.4: Tight central electron (TCE) identification requirements.

define the variables and associated cut values in this section.

$\mathbf{p_T}$ The transverse momentum of a track in the COT. $p_T = p \times \sin\theta$. Because of the axial field, the component of momentum in the plane perpendicular to the beam axis is the quantity measured by the tracker.

z0 The location in z of the intersection between a track and the beam axis.

$\mathbf{\Delta x}$ The track-stub matching distance in a muon chamber.

d0 The point of closest approach (impact parameter) of a track, relative to the beamline.

Cosmic-ray filter Cosmic rays can be identified in the CDF detector as dimuon events, where the two muons are approximately back-to-back. Since cosmic rays appear randomly in time and do not originate from a $p\overline{p}$ collision, such events can be identified using timing information and the impact parameter of the tracks with respect to the beam axis. Events with identified cosmic-ray muons are removed.

Table 4.5 lists the specific requirements used with these variables. Note that there are four types of central muons defined at CDF, one for each muon chamber: CMU, CMP, CMUP, CMX. (A 'CMUP' muon has a stub in both the CMU and CMP chambers.) In this analysis we also allow so-called "CMIO" muons, where the acronym stands for "Central Minimum-Ionizing Object." These are tracks which behave as muons, but are not fiducial to any of the four central muon chambers and thus cannot have a stub. Figure 4.11 shows an η vs. ϕ map of the acceptance regions for CMIO muons [41]. Table 4.6 lists the selection requirements for CMIO muons.

Variable	Cut value
Track P_T (COT-only beam-constrained track)	> 20.0 GeV
$\|z0_{track}\|$	< 60.0 cm
Cosmic ray removal	(cosmic ray tagger)
Calorimeter Energy (Em)	$< 2.0 + \max(0, 0.0115\times(p\text{-}100))$ GeV
Calorimeter Energy (Had)	$< 6.0 + \max(0, 0.028\times(p\text{-}100))$ GeV
Fractional Calorimeter Isolation E_T	< 0.1
$\|\Delta x_{CMU}\|$	< 3.0 cm
$\|\Delta x_{CMP}\|$	< 5.0 cm
$\|\Delta x_{CMX}\|$	< 6.0 cm
Track type	PADtrack
$\|d0_{track}\|$ (corrected for beam-spot position)	< 0.02 cm (if track has Si hits) OR < 0.2 cm (if not)
COT Track quality	3 axial & 3 stereo SL with at least 7 hits each

Table 4.5: Central muon ID cuts.

Variable	Cut value
Track P_T (COT-only beam-constrained track)	> 20.0 GeV
$\|z0_{track}\|$	< 60.0 cm
Cosmic ray removal	(cosmic ray tagger)
Fractional Calorimeter Isolation E_T	< 0.1
Calorimeter Energy (EM)	$< 2.0 + \max(0, 0.0115\times(p\text{-}100))$ GeV
Calorimeter Energy (Had)	$< 6.0 + \max(0, 0.028\times(p\text{-}100))$ GeV
Calorimeter energy (EM+Had)	> 0.1 GeV
$\|d0_{track}\|$ (corrected for beam-spot position)	< 0.02 cm (if track has Si hits) OR < 0.2 cm (if not)
COT Track quality	3 axial & 3 stereo SL with at least 7 hits each

Table 4.6: CMIO muon ID cuts.

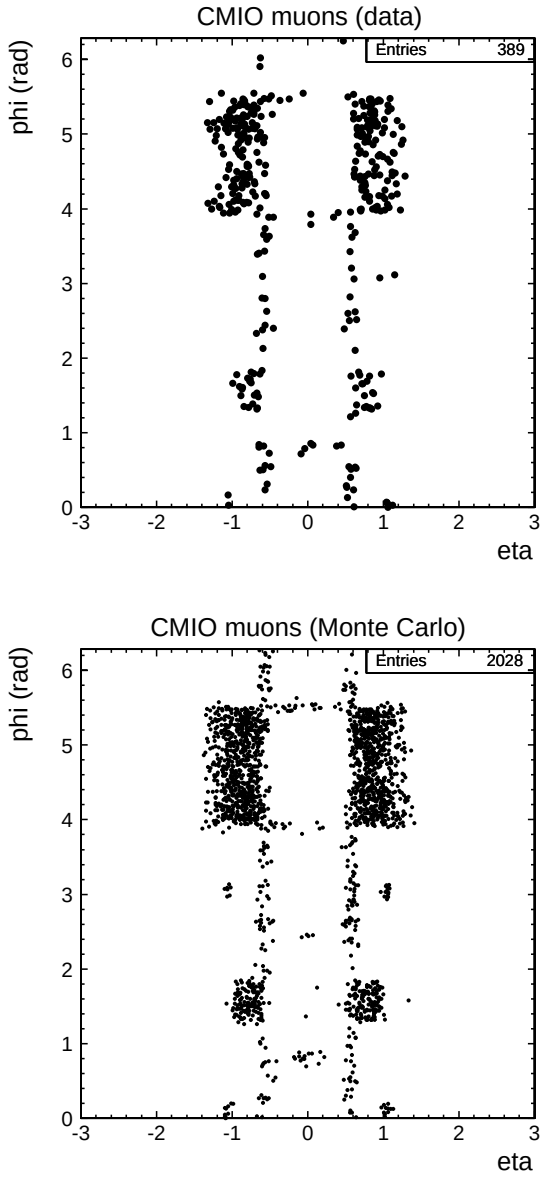

Figure 4.11: Distributions of the η vs.ϕ map for CMIO muons from data (top) and Monte Carlo (bottom).

4.4 Jets

The fragmentation processes of quarks and gluons to form colorless states are not yet well understood. Phenomenological models exist, however calculations from first principles within the framework of QCD are still an active subject of theoretical research. In the CDF detector, hadronic jets generally appear as many-tower clusters in the calorimeters, accompanied by many tracks[5]. Several different types of algorithms have been developed to cluster jets within the calorimeter, however the basic goal is the same: One wants to bound the jet within a readily defined portion of the detector, and provide an accurate estimation of its energy without including too much unrelated activity from the event. For this analysis, we use a relatively simple jet clustering approach which forms a cone of radius $R = \sqrt{(\Delta\eta)^2 + (\Delta\phi)^2} = 0.4$ around the highest energy tower in a local neighborhood, and sums the energy of towers within the cone. Because jets often cover a portion of the calorimeter which is large compared to the size of an individual tower, a non-neglible fraction of the total jet energy is typically absorbed by non-active material in the detector. These effects are known, and trying to understand how best to deal with them is the (large) subject of *jet corrections*, which will be touched on briefly in the following chapter. To select jets for this analysis, we require (corrected) $E_T > 15$ GeV, and $|\eta_{jet}| < 2.5$. Note that due to the way objects are defined at CDF, perfectly good electrons will be counted as jets and are thus explicitly removed from jet collections to avoid double counting.

[5]Jets do not always appear as many particles, and do not always deposit energy over a large area. For instance, a jet will sometimes fluctuate to a single pion.

4.5 Missing transverse energy

The incident p and $\overline{p}$ beams have their momenta aligned along the z axis. Thus in any given collision, although the energy flow along the beam axis is not precisely measured at CDF, the net transverse energy flow must sum to zero by conservation of momentum. As mentioned previously, we create a two-dimensional vector definition of energy, and use the variable E_T. In practice when one sums the total vector E_T of each tower in an event, a value different from zero is obtained. This missing transverse energy is defined as

$$\not{E}_T \equiv -\left(\sum_{towers} E_T\right) ,$$

and has two primary sources:

- Real $\not{E}_T$ from neutrinos.
- $\not{E}_T$ from mismeasured jets, *etc.* due to cracks and fluctuations in calorimeter response.

When performing the analysis, we correct event quantities (calorimeter energy, track p_T, *etc.*) to the extent possible, and recompute the $\not{E}_T$ on an event-by-event basis. In addition to these corrections, we also correct the $\not{E}_T$ for muons, which are minimum-ionizing particles in the calorimeters but should not contribute to the missing energy of an event.

For dilepton $t\overline{t}$ events, which have two neutrinos, a study of $\not{E}_T$ distributions suggests topological requirements which are useful as event selection criteria. These requirements, and the corrections applied to event quantities, are discussed in the following chapter.

Having discussed the definitions of leptons, jets, and $\not\!\!E_T$, we are now ready to combine these into the full selection procedure for identifying dilepton $t\bar{t}$ events.

CHAPTER 5

Event selection and acceptance

The previous chapter discusses the identification of each of the constituent objects in the final states of dilepton $t\bar{t}$ decays. Building on these definitions, we now describe the higher level analysis variables used to select $p\bar{p} \to t\bar{t} \to jj\ell\bar{\ell}\not\!\!E_T$ events in the data, and discuss some of the specific efforts made to increase the acceptance for this decay channel.

5.1 Corrections to event variables

To estimate values for the event variables most precisely, we apply several corrections to the raw measured quantities from the detector.

5.1.1 Vertex correction

The calorimeter clustering algorithms use a default vertex located at $z = 0$. Using the track $z0$ of the highest-energy lepton in the event, we recluster calorimeter objects and calculate corrected values for E_T.

5.1.2 CEM and PEM energy corrections

To correct the energy response of the CEM, we apply three distinct correc-

tions in the following order [42]: "Face map" corrections (measured using test beam electrons) account for local variations in response within each tower. Next we apply tower-to-tower gain corrections, which we derive using an ensemble of the E/p distributions from each tower. These corrections gradually smooth the response of the towers by an iterative process which normally converges within ten cycles. The final step is a global shift of the corrected gain, which returns the absolute energy scale of the calorimeter to the proper value. Finally we apply time-dependent corrections, which account for effects such as the aging of phototubes and scintillator plastic.

Similar procedures yield face map, tower-to-tower, and absolute energy scale corrections for the PEM detector [43, 44, 45]. The data reprocessing performed for this analysis marks the first time that the full suite of PEM energy corrections was successfully included into the offline reconstruction.

5.1.3 Curvature corrections

Distortions in the superstructure of the COT result in a small false curvature of tracks. This is removed by studying the E/p distribution as a function of charge. The fix evolves with time and is dependent on the version of the reconstruction code used. In this analysis we use the following relation to correct for the effect [46]:

$$\text{corrcurv} = \text{curv} - 0.00042 - 0.00116 \times \sin(\phi_\mu^0 + 0.3).$$

The corrected curvature is applied to the transverse momentum of tracks, since $p_T \propto \frac{1}{\text{curv}}$.

5.1.4 Jet corrections

Many ongoing efforts to improve the measurement of jets at CDF fall under the broad heading of jet corrections. Below we summarize the seven cumulative levels of jet corrections which are currently defined:

Level 1 *Relative corrections.* These are extracted from dijet balancing, and attempt to make the response to jets uniform across the calorimeters by making E_T- and η-dependent corrections such that the energy scale is everywhere equal to the average scale between $0.1 < |\eta| < 0.6$.

Level 2 *Time-dependent corrections.* These are now replaced by the calorimeter time-dependent corrections, which are essentially the same.

Level 3 *Raw energy scale corrections.* These are a comparison between the results from photon–jet balancing in Run I and Run II, and are an attempt to recover the raw jet energy scale of Run I. These corrections are oriented towards Run I because the level 5 corrections are also (still) taken from Run I.

Level 4 *Multiple interaction corrections.* These are based on the number of identified primary vertices in an event, and are small because the data for this analysis were collected when we expect < 1 extra interaction per crossing (See Fig. 5.1). For technical reasons involving vertex-finding algorithms, Level 4 corrections are ignored in this analysis.

Level 5 *Absolute energy corrections.* These attempt to translate calorimeter energy (back) to particle energy by correcting the calorimeter response to the $\sum p_T$ of tracks within $\Delta R < 0.5$ of the jet direction. Level 5 corrections are still based on Run I.

Level 6 *Underlying event corrections.* These subtract underlying event energy (measured from minimum bias data) from the jet energy measured in the calorimeter. These are small and are ignored in this analysis.

Level 7 *Out-of-cone corrections.* These correct for (missed) energy outside the clustered jet, and are an attempt to translate particle-level jets back to parton-level jets. Level 7 corrections are ignored in this analysis.

We correct all jets in an event according to levels 1, 2, 3, and 5 before enforcing selection requirements.

5.1.5 Leakage correction to isolation

The clustering algorithms used with the CEM and PEM calorimeters [47, 48] are designed to locate electromagnetic showers with high efficiency in an environment with substantial amounts of hadronic activity. By construction these algorithms form clusters which generally do not contain the full energy of a shower. Unclustered shower energy (transverse to the cluster, in neighboring EM towers) is known as *leakage* energy, and affects the isolation variable used in electron identification. We employ a leakage-corrected isolation variable derived from studies of $Z \to e^+e^-$ events from data [49].

5.2 The H_T cut

Due to the large mass of the top quark, the total amount of energy deposited in the detector in $t\bar{t}$ decays is typically greater than in most other processes. We exploit this for event selection by constructing the variable H_T, which is defined

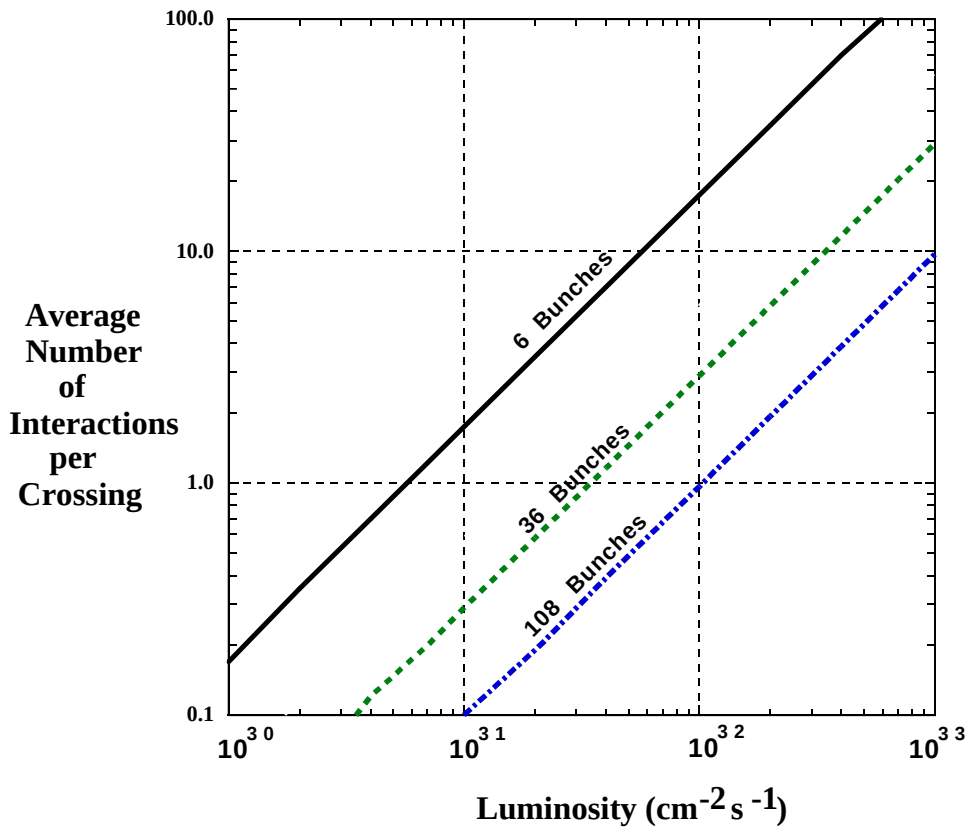

Figure 5.1: Average number of interactions per crossing as a function of instantaneous luminosity. The current running conditions (36 bunches, $\mathcal{L} \approx 5 \times 10^{31}$ cm^{-2}s^{-1}) correspond to approximately one interaction per crossing.

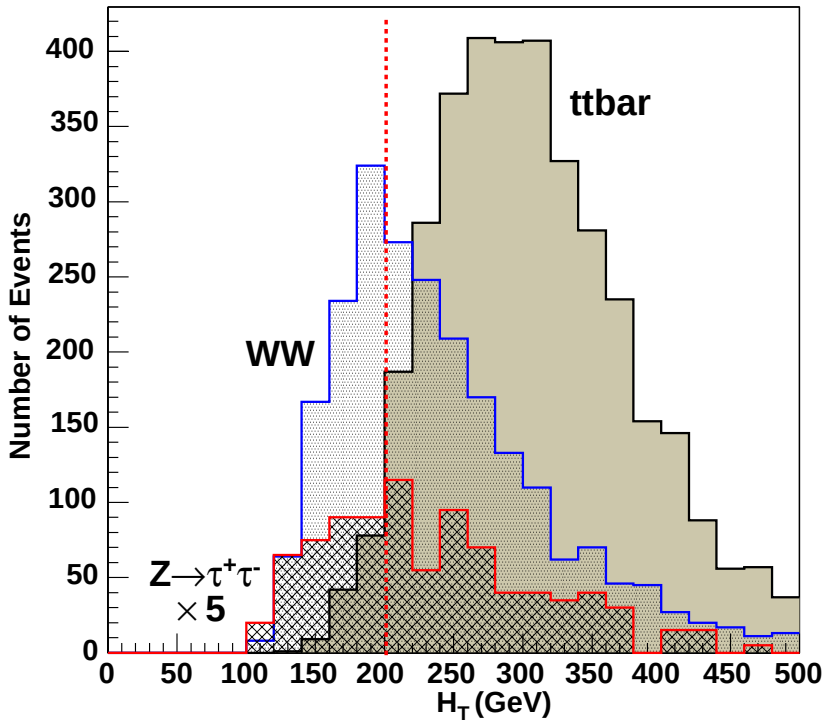

Figure 5.2: The H_T distribution for $t\bar{t}$ and the WW and $Z \to \tau^+\tau^-$ background processes.

as the scalar sum:

$$H_T \equiv \not{E}_T + \sum_{\text{leptons}} E_T \,(\text{or}\, p_T) + \sum_{\text{jets}} E_T \,,$$

where all quantities are fully corrected. Figure 5.2 shows Monte Carlo distributions of the H_T variable for $t\bar{t}$ and the WW, and $Z \to \tau\overline{\tau}$ background processes. The cut is placed at $H_T > 200$ GeV.

5.3 Non-isolated leptons

Since $t\bar{t}$ events typically deposit energy in the detector over a large number of calorimeter towers, the dilepton channel incurs a loss in acceptance due to the isolation requirements placed on the leptons. Backgrounds rise unacceptably if we remove the isolation requirement for both leptons in an event; however, we do allow events with one non-isolated TCE, CMUP, CMU, CMP, or CMX lepton to increase the acceptance. Jets are more likely to satisfy the selection requirements for CMIO, PHX, and PEM leptons, hence we always require that they be isolated. Including non-isolated leptons yields an acceptance increase of approximately 16%.

5.4 Topological $\not\!\!E_T$ requirements

Dilepton $t\bar{t}$ decays typically produce large $\not\!\!E_T$ in the detector which is not strongly oriented along the direction of the charged leptons or jets. This is in contrast to many of the background processes such as $Z + jets$, where the $\not\!\!E_T$ is usually due to a mismeasured jet, or $Z \rightarrow \tau^+\tau^-$, where the neutrinos from τ decay are usually boosted in the direction of the parent particle. We therefore make the following requirements as part of our dilepton event selection:

- $|\not\!\!E_T| > 25$ GeV
- If $|\not\!\!E_T| < 50$ GeV, additionally require $|\Delta\phi\,(\not\!\!E_T\,,\,\text{nearest}\,\ell\,\text{or jet})| > 20°$

To motivate these requirements, distributions of $\Delta\phi(\not\!\!E_T\,,$ nearest ℓ or jet) vs. $|\not\!\!E_T|$ for $Z \rightarrow \tau^+\tau^-$ Monte Carlo, $Z + jets$ data, and $t\bar{t}$ Monte Carlo are shown in Figure 5.3. All quantities are corrected before the cuts are applied.

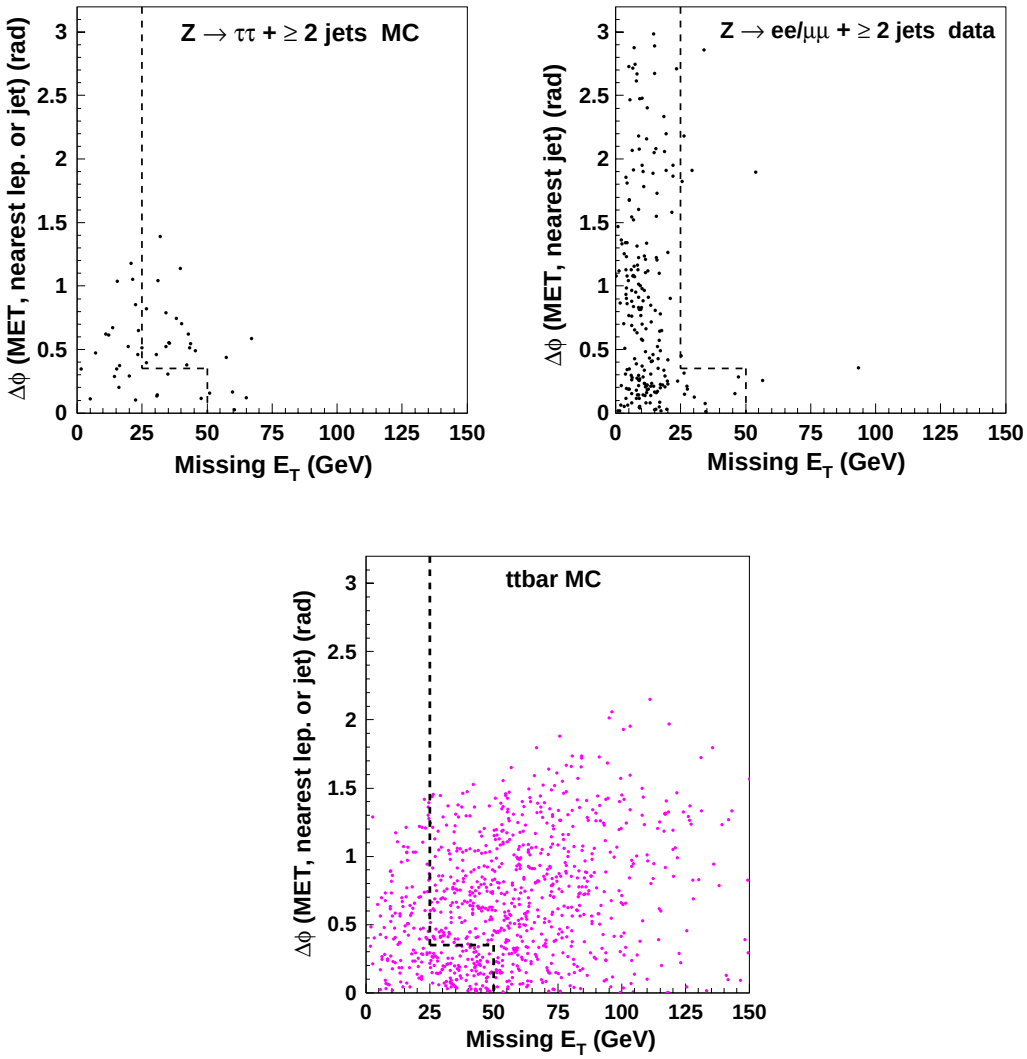

Figure 5.3: Distributions of $\Delta\phi\,(\not{E}_T\,,\,\text{nearest}\,\ell\,\text{or}\,\text{jet})$ vs. $|\not{E}_T\,|$ for $Z \to \tau^+\tau^-$ Monte Carlo, $Z + jets$ data, and $t\bar{t}$ Monte Carlo. The region to the left of the dotted line is excluded by the event selection criteria.

5.5 Jet significance

One source of background to same-flavor (ee, $\mu\mu$) dilepton events is the $Z+$ *jets* process. These events can be rejected efficiently without a sophisticated procedure, but they are still a difficulty because the production cross-section for Z bosons is approximately 35 times higher than that for $t\bar{t}$ at the energy of the Tevatron. Previous analyses in the dilepton channel swept away this issue by simply excluding events where the invariant mass of the lepton pair falls within the Z mass window, ($76 < M_{\ell\bar{\ell}} < 106\,\mathrm{GeV}$). Excluding this region, however, results in a loss in acceptance of approximately 24% for each same-flavor channel, as illustrated in Figure 5.4. This corresponds to a $\sim$12% loss in total acceptance. For this analysis we are willing to accept a loss in purity to regain $t\bar{t}$ events which fall under the Z peak. To explore a more sophisticated procedure which recovers events in this region efficiently, we repeat a thorough study performed in Run I [50, 51]: The $\not\!\!E_T$ in $Z + jets$ events is almost entirely due to mismeasured jets which deposit a non-negligible fraction of their energy in uninstrumented portions of the calorimeter. We therefore construct a variable which quantifies the degree to which mismeasurement of jets is a source of $\not\!\!E_T$ in an event. The variable is known as *jet significance*, which is defined as:

$$jetsig \equiv \frac{|\not\!\!E_T\,|}{\sqrt{\sum\left(\vec{E}_{T\,jet}\cdot\hat{\not\!\!E_T}\right)}}\,,$$

where the sum includes only jets in the same hemisphere as the $\not\!\!E_T$. The efficacy of this variable is improved by combining it with a requirement on the ϕ angle between the $\not\!\!E_T$ and the closest jet (to the $\not\!\!E_T$). Distributions of $\Delta\phi(\not\!\!E_T$, nearest jet) vs. *jetsig* are shown in Figure 5.5. By requiring

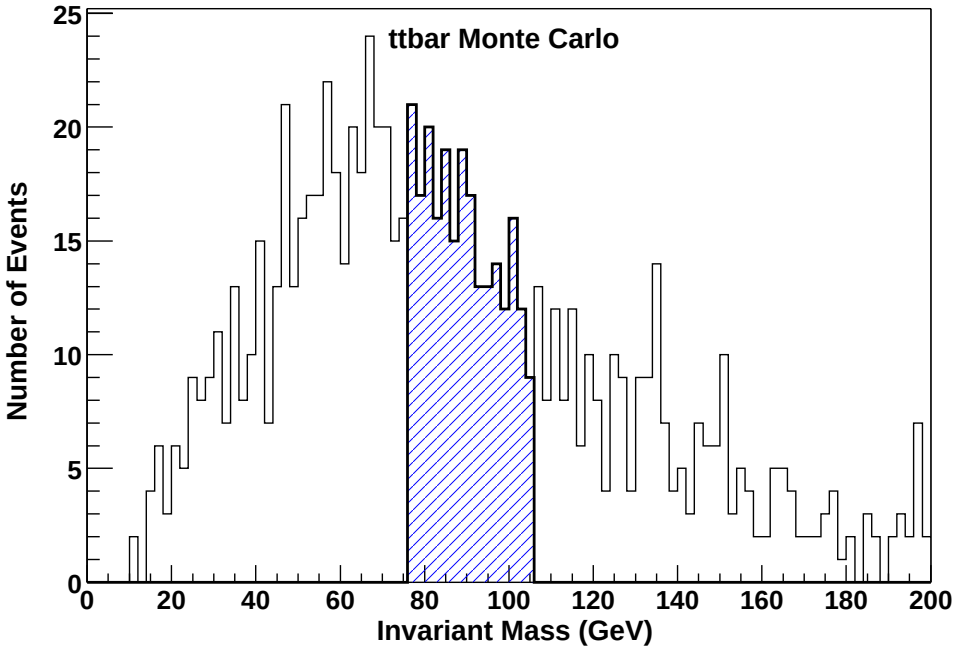

Figure 5.4: Invariant mass distribution for dilepton $t\bar{t}$ events in the ee channel. The shaded region corresponds to the Z mass window ($76 < M_{\ell\bar{\ell}} < 106\,\mathrm{GeV}$). Excluding this region represents a loss in acceptance of $\sim$24%.

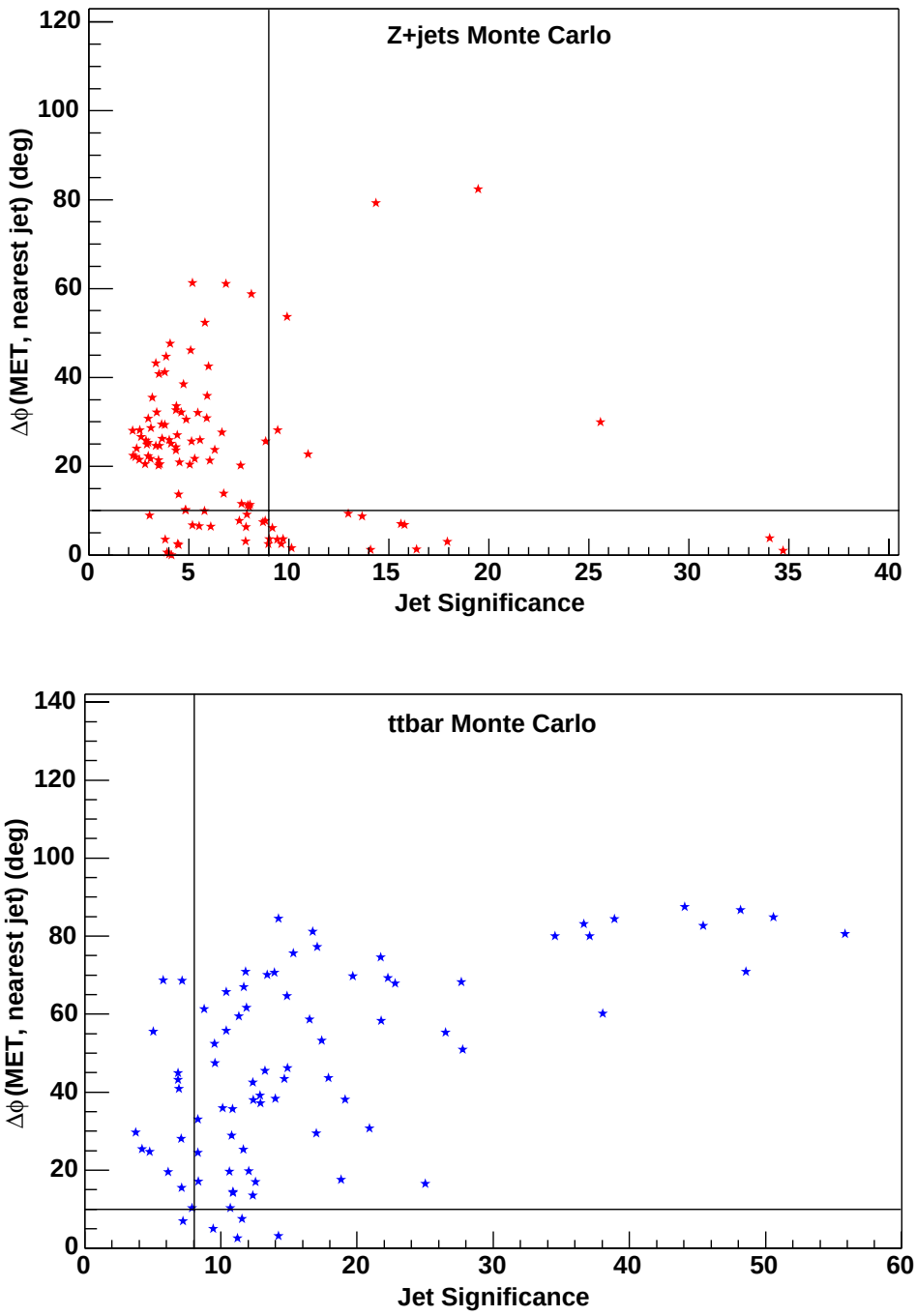

Figure 5.5: Monte Carlo distributions of $\Delta\phi\,(\not{E}_T\,,\,\text{nearest jet})$ vs. *jetsig* for $Z + jets$ events (top) and $t\bar{t}$ events (bottom). The selection requirements ($jetsig > 8$, $\Delta\phi > 10°$) are indicated by the lines.

- $jetsig > 8.0$
- $|\Delta\phi\,(\not\!\!E_T\ ,\ \text{nearest jet})| > 10^\circ$

we estimate that 87% of same-flavor $t\bar{t}$ events in the Z window can be kept, while rejecting 80% of $Z + jets$ events. This represents an increase in the overall acceptance of about 10%.

5.6 Data sets

We use three data sets for this analysis: one based on central electrons, one on central muons, and one on plug electrons [52, 53]. Each of these is created in a series of steps, described briefly below:

1. We begin with a data set comprised of events passing one or more specific level-three triggers. For the central electron data set:

   - Three triggers with overlapping requirements specify a CEM cluster with $E_T > 18$ GeV and $p_T > 9$ GeV, which also satisfies a relaxed set of ID requirements on the Had/EM, Lshr, and Δz variables.
   - Two triggers with overlapping requirements specify a CEM cluster with $E_T > 25$ GeV, $\not\!\!E_T > 15$ GeV, and isolation energy < 2 GeV. No track is required.
   - A trigger requiring two CEM clusters as specified above by the first bullet, but without track requirements.

   For the central muon data set:

   - A trigger requiring a track with $p_T > 18$ GeV, CMU and CMP stubs, and Δx matching requirements between the track and both stubs.

- Same as above but with only a CMX stub.

For the plug electron data set:

- Two triggers with overlapping requirements specify $\not\!\!E_T > 15$ GeV and a PEM cluster with $E_T > 20$ GeV, which also satisfies a relaxed set of ID requirements on the Had/EM and isolation ratio variables.
- Two similar triggers requiring one and two PEM cluster(s) with $E_T > 20$ GeV.

2. In the case of central electrons and muons, we refine the level-three trigger data set to a smaller intermediate sample by selecting events which satisfy a relaxed set of the identification requirements listed in the previous chapter. This is done because such intermediate data sets are useful for many low-level studies peformed in parallel. For technical reasons involving the CDF data-handling and offline code we ignore this step for the plug electron data set.

3. We create the final central lepton data set used for the analysis by requiring at least one lepton satisfying the full set of selection requirements listed in the previous chapter. We create the final plug electron data set using only additional level-three trigger requirements.

A specific bit is set in the event record corresponding to each trigger which fired in a given event. To measure the efficiency of a trigger, we isolate a sample of events in which a specific trigger should have fired, and compare to the number of events in the sample which have the corresponding trigger bits set. Efficiencies for the triggers relevant to this analysis are described in detail in references [54] and [40]. The results are used in chapter 7 in the calculation of the cross-section.

Primary	Secondary
TCE	CMU
CMUP	CMP
CMX	CMIO
PHX	PEM
	NITCE
	NICMUP
	NICMU
	NICMP
	NICMX

Table 5.1: Primary and secondary leptons defined for the analysis.

5.7 Decay channels in the analysis

As discussed in chapter 4, we define eight types of leptons: TCE, CMUP, CMU, CMP, CMX, CMIO, PEM, and PHX. Additionally we allow five of these to be non-isolated, which we denote by prepending with "NI," as follows: NITCE, NICMUP, NICMU, NICMP, and NICMX. We classify these simply as *primary* and *secondary* leptons, as shown in Table 5.1. We allow all possible combinations consisting of at least one primary lepton, and present all studies of acceptance and backgrounds with each possible category shown explicitly. The full complement of allowed channels is listed here in Table 5.2.

5.8 Dilepton event selection

Below we summarize the complete procedure used to select dilepton events:

1. Check good run list.

2. Check trigger path.

central/central			central/plug		plug/plug
e/e	e/μ	μ/μ	e/e	e/μ	e/e
TCE/TCE	TCE/CMUP	CMUP/CMUP	TCE/PEM	CMUP/PEM	PHX/PEM
TCE/NITCE	TCE/CMU	CMUP/CMU	TCE/PHX	CMX/PEM	PHX/PHX
	TCE/CMP	CMUP/CMP	PHX/TCE	CMUP/PHX	
	TCE/CMX	CMUP/CMX	PHX/NITCE	CMX/PHX	
	TCE/CMIO	CMUP/CMIO		PHX/CMUP	
	CMUP/TCE	CMX/CMX		PHX/CMU	
	CMX/TCE	CMX/CMU		PHX/CMP	
	TCE/NICMUP	CMX/CMP		PHX/CMX	
	TCE/NICMU	CMX/CMIO		PHX/CMIO	
	TCE/NICMP	CMX/CMUP		PHX/NICMUP	
	TCE/NICMX	CMUP/NICMUP		PHX/NICMU	
	CMUP/NITCE	CMUP/NICMU		PHX/NICMP	
	CMX/NITCE	CMUP/NICMP		PHX/NICMX	
		CMUP/NICMX			
		CMX/NICMX			
		CMX/NICMU			
		CMX/NICMP			
		CMX/NICMUP			

Table 5.2: Dilepton decay channels defined in the analysis. The implied ordering is A/B, where A must be a primary lepton, and B can be either a primary or secondary lepton. The lepton corresponding to A must be associated with a trigger which is recorded in the event. All possible combinations are shown explicitly.

3. Require two leptons, consistent with one of the allowed categories, selected according to the requirements listed in chapter 4.

4. Calculate the invariant mass of the lepton pair. If $76 < M_{ee,\mu\mu} < 106\,\mathrm{GeV}$, require $jetsig > 8$ and $\Delta\phi > 10^\circ$ ($\not\!\!E_T$, nearest jet).

5. Apply level 1,2,3 and 5 jet corrections to all jets in the event. Jet corrections include relative and absolute corrections, but do not include multiple interaction corrections.

6. Apply curvature corrections for muon p_T.

7. Correct the magnitude and phi angle of $\not\!\!E_T$ for muons and jets (corrected jet $E_T > 15$ GeV, $|\eta_{jet}| < 2.5$).

8. Require $|\not\!\!E_{T\ corrected}| > 25$ GeV.
   If < 50 GeV, additionally require $\Delta\phi$ ($\not\!\!E_T$, nearest ℓ or jet)$> 20^\circ$.

9. Require ≥ 2 jets (corrected $E_T > 15$ GeV, $|\eta_{jet}| < 2.5$).

10. Require $H_T > 200$ GeV ($\sum \{\not\!\!E_T$, ℓ's, jets$\}$, using corrected quantities).

11. Require oppositely charged leptons for all categories where both leptons are required to have an associated track.

12. Veto conversions[1] (tridents are kept).

13. Veto cosmic rays.

When these selection requirements are applied to the primary data sets we find a total of 10 events. These are discussed in detail in chapter 7, however this number

[1]Electrons which are produced from photons are known as conversions; tridents refer to electrons which radiate a bremsstrahlung photon that subsequently converts to an e^+e^- pair.

is useful as a comparison when reading the following chapter on the estimation of backgrounds to the analysis.

5.9 Acceptance

To estimate the acceptance for dilepton $t\bar{t}$ decays we use an official Monte Carlo sample of $398,037$ inclusive $t\bar{t}$ events. The sample is generated with $m_t = 175$ GeV, using version 6.216 of the Pythia Monte Carlo package. Assuming a theoretical cross-section of $\sigma_{t\bar{t}}^{NLO} = 6.7\,\mathrm{pb}$ [18], the effective luminosity of the sample is $59.4\,\mathrm{fb}^{-1}$. The event selection used for the acceptance estimates is the same as that listed in the previous section, except that:

- Curvature corrections are not applied to Monte Carlo events.
- The Monte Carlo version of jet corrections is used.
- The cosmic ray filter is not used.

We study the acceptance for each possible channel individually, and record the contribution at nine separate stages[2] as the identification requirements are sequentially applied. The first stage is denoted as "Geom-p_T," and implies that the leptons satisfy fiducial and kinematic requirements (E_T or $p_T > 20$ GeV) within the detector. The second and third stages, "ID" and "iso," imply that the leptons satisfy all of the remaining identification requirements described in chapter 4. Because the acceptance is determined from Monte Carlo events, the

[2]The ordering of the stages at which the acceptance is examined is chosen primarily to match that of the Run I measurement. It is somewhat arbitrary now and need not reflect the exact ordering used to select candidate events in the data.

fourth stage, "conv+cosm," implies only that the leptons pass the conversion filter. The fifth stage, "Z veto," implies that the requirements on the jet significance variable and the associated minimum separation in ϕ (between the $\not\!\!E_T$ and the nearest jet) are satisfied. Events in the $e\mu$ channel pass the Z veto filter by default. The sixth stage, "$\not\!\!E_T$" and "$\Delta\phi$," implies that the event satisfies the topological requirements on $\not\!\!E_T$. The seventh stage shows explicitly the number of jets present in events which have passed the requirements corresponding to the previous stages; only those events with ≥ 2 corrected jets may contribute to the acceptance. The eighth stage, "H_T," shows the number of events with ≥ 2 jets which satisfy the H_T requirement. The final stage, "OS," implies that the two leptons in the event have opposite charges. This does not apply to categories involving PEM electrons, for which there is no associated track and thus no charge information. Multilepton categories (3ℓ, 4ℓ, 5ℓ) are treated separately. They must have at least one primary lepton, and are not subject to the opposite-sign requirement.

The raw acceptance estimates, shown explicity for each possible channel, are summarized in Tables 5.3 – 5.6. Using corrected event variables, we estimate the total acceptance for $t\bar{t} \to jj\ell\bar{\ell}\not\!\!E_T$ events to be $(0.92 \pm 0.01)\%$. This includes a contribution of approximately 5% from events with one hadronic W decay (due to the non-isolated lepton categories), where one of the jets is misidentified as a lepton. To simplify background estimates, we require dilepton decays at the generator level, which reduces the estimate of the total acceptance to $(0.87 \pm 0.02)\%$. Note that approximately 12% of the acceptance is due to channels with a τ lepton, which subsequently decays to an electron or muon. To arrive at the acceptance value used in the calculation of the cross-section, we apply lepton ID efficiency scale factors to account for differences between data and Monte Carlo. These are summarized in Table 5.7. Including the scale factors and trigger efficiencies

	Dilepton Cut						NJets				
Category	Geom-Pt	ID	iso	conv+cosm	Z veto	$\not\!\!E_T$, $\Delta\phi\,(\not\!\!E_T\,,\,\ell\,j)$	0j	1j	2j	H_T	OS
TCE/TCE	51756	1013	982	758	702	588	9	77	502	490	485
TCE/NITCE				195	174	134	4	28	102	97	67
TCE/PHX	8076	389	389	339	326	278	2	46	230	222	208
PHX/NITCE				43	38	27	0	6	21	21	17
TCE/PEM	6827	151	139	138	130	100	0	11	89	88	88
PHX/PHX	467	40	40	40	39	33	0	4	29	27	22
PHX/PEM	518	30	30	30	28	21	0	3	18	18	18
Total ee	67644	1623	1580	1543	1437	1181	15	175	991	963	905

Table 5.3: Breakdown of the ee portion of the $t\bar{t}$ acceptance.

reduces the overall acceptance by 10.0%. The relative contributions of the central and plug detectors to the overall acceptance are: central/central (80.6%), central/plug (18.3%), plug/plug (1.1%), as shown in Table 5.8. Also shown in Table 5.8 are the relative contributions by lepton type: ee (24.8%), $e\mu$ (53.5%), $\mu\mu$ (21.7%). We estimate a total of 6.3 ± 0.7 dilepton $t\bar{t}$ events in $126\,\mathrm{pb}^{-1}$ of data.

5.10 Systematic uncertainties

We estimate systematic uncertainties for the acceptance calculation due to different Monte Carlo generators, Monte-Carlo modeling of QED and QCD initial- and final-state radiation (ISR/FSR), parton distribution functions (PDFs), jet corrections, and lepton ID scale factors [55].

To estimate the contribution from different Monte Carlo generators we compare the acceptance obtained with the Pythia sample to that from a sample generated with Herwig. We use Pythia to quote the central value of the acceptance because it provides a better treatment of ISR/FSR than the version of

	Dilepton Cut						NJets				
Category	Geom-Pt	ID	iso	conv+cosm	Z veto	$\not\!\!E_T$, $\Delta\phi\,(\not\!\!E_T\,,\,\ell\,j)$	0j	1j	2j	H_T	OS
CMUP/CMUP	2522	352	348	288	270	221	0	36	185	175	175
CMUP/NICMUP				60	53	45	1	1	43	42	38
CMUP/CMU	1202	123	100	81	77	63	1	11	51	50	50
CMUP/NICMU				19	18	16	0	1	15	15	11
CMUP/CMP	1327	189	168	145	140	115	1	15	99	95	95
CMUP/NICMP				23	22	16	0	0	16	16	11
CMUP/CMX	2625	267	266	209	195	156	0	18	138	132	132
CMUP/NICMX				30	25	22	0	0	22	22	13
CMX/NICMUP				27	25	18	0	0	18	17	13
CMUP/CMIO	4060	166	149	149	141	120	0	24	96	90	90
CMX/CMU	730	47	36	32	30	27	0	1	26	26	26
CMX/NICMU				4	3	3	0	0	3	3	3
CMX/CMP	707	76	64	57	51	41	0	0	41	38	38
CMX/NICMP				7	5	3	0	1	2	2	2
CMX/CMX	1030	60	60	48	45	38	0	5	33	32	32
CMX/NICMX				12	10	10	0	0	10	10	7
CMX/CMIO	2480	96	85	85	78	66	0	11	55	54	54
Total $\mu\mu$	16683	1376	1276	1276	1188	980	3	124	853	819	790

Table 5.4: Breakdown of the $\mu\mu$ portion of the $t\bar{t}$ acceptance.

Herwig currently available in the CDF offline code. The acceptance obtained with the Herwig sample was reweighted due to differences in the handling of branching fractions for W decays. We estimate a systematic uncertainty of 3.9% due to Monte Carlo generators. Note that this is much smaller than the overall statistical uncertainty on the cross-section measurement.

We estimate the systematic uncertainty due to ISR/FSR using two alternate $t\bar{t}$ Monte Carlo samples, both generated with Pythia. One has QED and QCD ISR/FSR explicitly turned off, and the other uses a different tune for the underlying event energy. We estimate a systematic uncertainty of 1.6% by adding in quadrature the relative differences between the central value of the acceptance and those obtained with each of the alternate Monte Carlo samples.

The systematic uncertainty due to PDFs is divided into three separate contributions:

	Dilepton Cut						NJets				
Category	Geom-Pt	ID	iso	conv+cosm	Z veto	$\not\!\!E_T$, $\Delta\phi\,(\not\!\!E_T\,,\,\ell\,j)$	0j	1j	2j	H_T	OS
TCE/CMUP	21711	1220	1202	945	945	745	4	94	647	630	625
TCE/NICMUP				137	137	107	0	5	102	100	84
CMUP/NITCE				104	104	84	4	11	69	67	52
TCE/CMU	5781	220	196	172	172	138	2	16	120	114	114
TCE/NICMU				21	21	12	0	0	12	9	9
TCE/CMP	5671	351	303	255	255	210	1	29	180	175	175
TCE/NICMP				48	48	39	0	1	38	36	32
TCE/CMX	12755	469	463	357	357	292	1	47	244	235	234
TCE/NICMX				52	52	37	0	2	35	35	27
CMX/NITCE				46	46	34	2	6	26	24	22
TCE/CMIO	21545	345	321	320	320	265	3	33	229	223	222
PHX/CMUP	1828	246	246	219	219	164	1	29	134	128	112
PHX/NICMUP				27	27	22	0	0	22	22	13
PHX/CMU	507	48	48	39	39	32	1	3	28	26	25
PHX/NICMU				9	9	8	0	1	7	7	6
PHX/CMP	469	73	73	62	62	48	0	3	45	42	39
PHX/NICMP				11	11	6	0	1	5	4	4
PHX/CMX	1091	77	77	68	68	49	2	5	42	39	38
PHX/NICMX				9	9	7	0	0	7	5	3
PHX/CMIO	1695	66	66	66	66	47	1	7	39	38	33
CMUP/PEM	1415	98	87	87	87	67	0	8	59	57	57
CMX/PEM	848	38	34	34	34	28	0	3	25	24	24
Total $e\mu$	55925	3251	3116	3088	3088	2441	22	304	2115	2040	1950

Table 5.5: Breakdown of the $e\mu$ portion of the $t\bar{t}$ acceptance.

	Dilepton Cut						NJets				
Category	Geom-Pt	ID	iso	conv+cosm	Z veto	$\not\!\!E_T$, $\Delta\phi\,(\not\!\!E_T\,,\,\ell\,j)$	0j	1j	2j	H_T	OS
3ℓ	184	146	128	68	67	51	3	19	31	28	–
4ℓ	0	0	0	0	0	0	0	0	0	0	–
5ℓ	0	0	0	0	0	0	0	0	0	0	–
Total 398037	140436	6396	6100	5975	5780	4653	43	622	3990	3850	3645

Table 5.6: Multilepton and general summary of the acceptance breakdown.

Lepton type	Scale factor
TCE	0.98 ± 0.01
NITCE	0.78 ± 0.07
PEM	0.96 ± 0.05
PHX	0.99 ± 0.01
CMUP	0.94 ± 0.01
CMX	1.00 ± 0.01
CMU	0.97 ± 0.02
CMP	0.96 ± 0.02
NI muons (all)	0.85 ± 0.09

Table 5.7: Summary of the lepton scale factors (data/MC) used to correct the acceptance.

	ee	$e\mu$	$\mu\mu$	Total
central/central	552	1596	790	2938 (80.6%)
central/plug	313	354	—	667 (18.3%)
plug/plug	40	—	—	40 (1.1%)
Total	905 (24.8%)	1950 (53.5%)	790 (21.7%)	3645

Table 5.8: Summary of the relative contributions to the acceptance by detector region and lepton type. As listed in the text, the percentages correspond to the fraction of the total acceptance. The total number of dilepton channel events (3645) corresponds to a total acceptance of 0.916%.

- The Monte Carlo sample from which we obtain the central value of the acceptance uses the CTEQ6M set of PDFs. We compare to another sample, also generated with Pythia, which uses the MRST72 set of PDFs, and find a difference in the acceptance of -1.6%.

- We compare to another Pythia sample, using the MRST75 set of PDFs, which additionally has a lowered value of the strong coupling constant, $\alpha_S = 0.112$. We find a difference in acceptance of -0.3% relative to the central value.

- We alter (3) parameters within the CTEQ6M set of PDFs to give the maximum variation between the quark and gluon distribution functions, and also shift the fits to the distribution functions by $\pm 1\sigma$ of the uncertainty on the fit. We take the half-difference divided by the half-sum as the systematic variation on each parameter, and add these in quadrature to obtain a total systematic uncertainty of 7.5% due to PDFs.

The values of these three contributions are summed in quadrature to give a total estimate of 7.7%.

We estimate the contribution from jet corrections following an official procedure suggested by the CDF jet corrections working group [56]. The details of the method will not be discussed here. We obtain an estimate of 5.6% for the total systematic uncertainty due to jet corrections.

To estimate the systematic uncertainty from lepton ID scale factors, we recompute the change to the acceptance with the scale factors shifted by their $\pm 1\sigma$ statistical uncertainties. This yields an estimate of 2.0%.

We treat these five separate contributions as uncorrelated, and arrive at a total systematic uncertainty on the acceptance estimate of 10.6%.

CHAPTER 6

Backgrounds

The backgrounds to dilepton top decays, which may also produce $jj\ell\bar{\ell}\not{E}_T$ final states, are diboson events (WW, WZ), $Z \to \tau^+\tau^-$ decays, Drell-Yan processes, and QCD "fakes." The latter implies that a jet, in $W+jets$ events, is misidentified as a lepton in the detector, and thus mimics a dilepton signature. We estimate the background contribution from WW, WZ, and $Z \to \tau^+\tau^-$ processes using Monte Carlo samples, and obtain the estimates for Drell-Yan and QCD fakes from data. The event selection used for all of the Monte Carlo based estimates is the same as that listed in chapter 5, with the same exceptions as for the acceptance estimate.

6.1 WW/WZ background

To estimate the expected number of WW and WZ background events we use two official Monte Carlo data sets, both generated using version 6.216 of the Pythia Monte Carlo package. The WW sample consists of $828,000$ $WW \to \ell\ell$ events, where leptonic decays of the W's are forced. Using $\sigma_{WW}^{NLO} = 13.25$ pb [57], and taking account of the branching ratio for both W's to decay leptonically, the effective luminosity of the WW sample is 557 fb^{-1}. The WZ sample consists of 1.39 million $WZ \to \ell\ell$ events, where leptonic decays of both the W's and Z's are forced. Using $\sigma_{WZ}^{NLO} = 3.96$ pb [57], and taking account of the branching ratio for two final state leptons, the effective luminosity of the WZ sample is

350 fb^{-1}. Both of these processes have real leptons and real $\not\!\!E_T$ from neutrinos. The energy spectrum associated with the WW and WZ processes is softer than that of $t\bar{t}$. Our primary handles to reject these backgrounds are the two-jet requirement and the H_T variable. The background estimates from WW, for each possible channel, are shown explicitly (as with the acceptance estimates) in Tables 6.1 – 6.4. Tables 6.5 – 6.8 show the estimates for the WZ process in the same fashion. We estimate the total contribution from both processes in 126 pb^{-1} to be 0.40 ± 0.17 events.

	Dilepton Cut						NJets				
Category	Geom-Pt	ID	iso	conv+cosm	Z veto	$\not\!\!E_T$, $\Delta\phi(\not\!\!E_T, \ell j)$	0j	1j	2j	H_T	OS
TCE/TCE	25088	12843	12679	11639	11553	8155	6543	1290	322	209	208
TCE/NITCE				702	689	494	353	102	39	25	25
TCE/PHX	4360	2776	2776	2684	2649	1872	1494	313	65	46	26
PHX/NITCE				61	61	47	36	8	3	2	1
TCE/PEM	14663	8775	8541	8454	8380	5885	4743	944	198	120	120
PHX/PHX	310	226	226	226	226	109	92	15	2	2	2
PHX/PEM	1459	1090	1090	1090	1085	849	698	130	21	11	11
Total ee	45880	25710	25312	24856	24643	17411	13959	2802	650	415	393

Table 6.1: Breakdown of the ee portion of the WW background estimate.

6.2 $\mathbf{Z \to \tau^+\tau^-}$ background

To estimate the expected number of $Z \to \tau^+\tau^-$ background events we use an official Monte Carlo data set. The sample consists of $422,363$ $Z/\gamma^* \to \tau^+\tau^-$ events, generated with version 6.216 of the Pythia Monte Carlo package. The τ leptons are decayed using the TAUOLA software package. The sample was filtered by requiring that the generated center-of-mass energy, E_{CM}, be greater than 30.0 GeV, and that there be two generator-level leptons with $E_T > 15$ GeV in the region $|\eta| < 2.5$. Using $\sigma = 335.3$ pb, and taking the filtering into account,

	Dilepton Cut						NJets				
Category	Geom-Pt	ID	iso	conv+cosm	Z veto	$\not\!\!E_T$, $\Delta\phi\,(\not\!\!E_T\,,\,\ell\,j)$	0j	1j	2j	H_T	OS
CMUP/CMUP	7290	4102	4075	3817	3793	2633	2100	433	100	71	71
CMUP/NICMUP				258	256	208	109	81	18	12	12
CMUP/CMU	3138	1690	1626	1580	1572	1073	846	193	34	25	25
CMUP/NICMU				46	46	34	16	13	5	1	1
CMUP/CMP	4048	2320	2247	2183	2167	1478	1162	259	57	41	41
CMUP/NICMP				64	64	51	18	26	7	5	5
CMUP/CMX	7328	3724	3722	3524	3499	2437	1921	430	86	57	57
CMUP/NICMX				102	101	75	42	23	10	6	6
CMX/NICMUP				96	92	74	26	32	16	9	8
CMUP/CMIO	7535	2825	2761	2761	2745	1991	1561	342	88	54	54
CMX/CMU	1615	780	758	733	728	508	405	93	10	9	9
CMX/NICMU				25	24	18	7	11	0	0	0
CMX/CMP	2048	1071	1023	996	982	698	593	80	25	14	14
CMX/NICMP				27	27	21	10	8	3	1	1
CMX/CMX	1910	899	897	847	843	547	451	70	26	18	18
CMX/NICMX				50	49	36	18	14	4	3	3
CMX/CMIO	4094	1464	1423	1423	1407	1028	862	138	28	21	20
Total $\mu\mu$	39006	18875	18532	18532	18395	12910	10147	2246	517	347	345

Table 6.2: Breakdown of the $\mu\mu$ portion of the WW background estimate.

the effective luminosity of the sample is $143\,\mathrm{fb}^{-1}$. As with the WW and WZ processes, these events have real leptons and real $\not\!\!E_T$ from neutrinos, and have an energy spectrum which is softer than that of $t\bar{t}$. The primary means to reject these events are the two-jet requirement and the topological cuts on $\not\!\!E_T$. Tables 6.9 – 6.12 summarize the background estimates for each possible channel. We estimate the total background contribution from $Z/\gamma^* \to \tau^+\tau^-$ events in 126 pb^{-1} to be 0.32 ± 0.11 events.

6.3 QCD fake background

The background we must consider from QCD fakes arises from $W + jets$ events with three or more jets, where one of the jets is misidentified as a lepton. We estimate the number of such events [58] by measuring the probability for a jet to fake each type of lepton defined for the analysis, and then apply these

	Dilepton Cut						NJets				
Category	Geom-Pt	ID	iso	conv+cosm	Z veto	$\not\!\!E_T$, $\Delta\phi\,(\not\!\!E_T\,,\ell\,j)$	0j	1j	2j	H_T	OS
TCE/CMUP	27080	14368	14264	13216	13216	9133	7375	1412	346	240	240
TCE/NICMUP				452	452	351	177	130	44	26	26
CMUP/NITCE				386	386	268	185	69	14	7	7
TCE/CMU	5780	2915	2825	2691	2691	1888	1530	290	68	45	45
TCE/NICMU				96	96	77	47	22	8	6	6
TCE/CMP	7220	3909	3789	3607	3607	2529	2030	385	114	75	75
TCE/NICMP				139	139	98	61	25	12	8	8
TCE/CMX	13512	6695	6654	6192	6192	4351	3538	649	164	104	104
TCE/NICMX				223	223	183	94	59	30	20	20
CMX/NITCE				175	175	130	87	30	13	9	9
TCE/CMIO	14821	5302	5149	5091	5091	3611	2868	589	154	105	105
PHX/CMUP	2337	1553	1553	1511	1511	1026	818	165	43	23	18
PHX/NICMUP				42	42	29	12	14	3	2	2
PHX/CMU	542	355	355	344	344	242	201	36	5	3	0
PHX/NICMU				11	11	9	3	6	0	0	0
PHX/CMP	643	403	403	395	395	269	225	32	12	9	5
PHX/NICMP				8	8	5	2	3	0	0	0
PHX/CMX	1265	802	802	787	787	584	479	91	14	5	2
PHX/NICMX				15	15	12	7	3	2	2	2
PHX/CMIO	1460	690	690	690	690	435	354	73	8	4	4
CMUP/PEM	7778	4855	4736	4736	4736	3240	2624	504	112	76	76
CMX/PEM	4177	2471	2409	2409	2409	1613	1308	250	55	29	29
Total $e\mu$	86615	44588	43629	43216	43216	30083	24025	4837	1224	798	783

Table 6.3: Breakdown of the $e\mu$ portion of the WW background estimate.

probabilities to events in the $W + jets$ data sample according to the following relation:

$$N_n^{fakes} = N_{n+1}^{obs} \times \left[1 - (1 - p_\ell^{fake})^{n+1}\right] \approx N_{n+1}^{obs} \times (n+1)\, p_\ell^{fake}\,,$$

where N_n is the number of events in the $W + jets$ sample with observed jet multiplicity n, and p_ℓ^{fake} is the probability for a jet to fake a given type of lepton. For all types of electrons, the probability is defined as the ratio:

$$p_e^{fake} = \frac{\#\,\text{EM clusters passing all electron ID requirements}}{\#\,\text{jets with}\, E_T^{corr.} > 15\,\text{GeV}}\,.$$

	Dilepton Cut						NJets				
Category	Geom-Pt	ID	iso	conv+cosm	Z veto	$\not\!\!E_T$, $\Delta\phi\,(\not\!\!E_T\,,\,\ell\,j)$	0j	1j	2j	H_T	OS
3ℓ	303	291	274	264	262	210	167	42	1	0	–
4ℓ	0	0	0	0	0	0	0	0	0	0	–
5ℓ	0	0	0	0	0	0	0	0	0	0	–
Total 827323	171804	89464	87747	86868	86516	60614	48298	9927	2392	1560	1521

Table 6.4: Multilepton and general summary of the WW background estimate.

	Dilepton Cut						NJets				
Category	Geom-Pt	ID	iso	conv+cosm	Z veto	$\not\!\!E_T$, $\Delta\phi\,(\not\!\!E_T\,,\,\ell\,j)$	0j	1j	2j	H_T	OS
TCE/TCE	9661	4752	4733	4175	2062	986	434	447	105	77	68
TCE/NITCE				443	250	87	43	34	10	7	6
TCE/PHX	2249	1276	1276	1210	620	275	129	127	19	11	7
PHX/NITCE				58	35	12	4	4	4	2	1
TCE/PEM	6790	3642	3423	3395	1748	824	330	399	95	73	73
PHX/PHX	186	138	138	138	71	23	12	8	3	1	1
PHX/PEM	642	428	428	428	221	107	47	50	10	6	6
Total ee	19528	10236	9998	9847	5007	2314	999	1069	246	177	162

Table 6.5: Breakdown of the ee portion of the WZ background estimate.

For all types of muons, the probability is defined as the ratio:

$$p_\mu^{fake} = \frac{\#\,\text{tracks passing all muon ID requirements}}{\#\,\text{jets with}\,E_T^{corr.} > 15\,\text{GeV} + \#\,\text{unmatched tracks with}\,p_T > 20\,\text{GeV}}\,,$$

where the matching distance between a jet and a track is a cone of $\Delta R < 0.4$ in $\eta - \phi$ space. We obtain the fake probabilities as a function of E_T and pseudorapidity, in bins of 2 GeV in energy and 0.1 in η. We use QCD jet samples to derive the fake probabilities because it is otherwise impossible to obtain a suitable number of jets and tracks. To avoid biasing our results, we remove real leptons from W events in the QCD data samples by requiring $\not\!\!E_T < 25$ GeV, and from Z events by rejecting EM clusters with an invariant mass between 76 and 106 GeV. The results are displayed in Figure 6.1; to simplify the bottom plot,

	Dilepton Cut						NJets				
Category	Geom-Pt	ID	iso	conv+cosm	Z veto	$\not\!\!E_T$, $\Delta\phi\,(\not\!\!E_T\,,\,\ell\,j)$	0j	1j	2j	H_T	OS
CMUP/CMUP	2031	1465	1463	1333	762	341	199	116	26	19	19
CMUP/NICMUP				130	74	34	14	13	7	6	6
CMUP/CMU	885	621	594	572	326	153	88	49	16	13	13
CMUP/NICMU				22	9	3	1	1	1	1	1
CMUP/CMP	1134	820	786	751	401	157	96	48	13	9	8
CMUP/NICMP				35	16	4	1	3	0	0	0
CMUP/CMX	2212	1512	1507	1377	748	338	186	121	31	22	19
CMUP/NICMX				54	27	9	1	8	0	0	0
CMX/NICMUP				76	35	11	4	4	3	3	2
CMUP/CMIO	2597	1156	1103	1103	588	273	170	85	18	16	16
CMX/CMU	496	309	289	277	147	56	34	18	4	4	4
CMX/NICMU				12	7	2	1	0	1	1	1
CMX/CMP	621	423	402	380	201	93	54	32	7	7	7
CMX/NICMP				22	10	5	2	2	1	1	1
CMX/CMX	585	369	366	338	188	84	50	32	2	1	1
CMX/NICMX				28	8	4	3	1	0	0	0
CMX/CMIO	1476	579	548	548	313	155	90	52	13	7	7
Total $\mu\mu$	12037	7254	7058	7058	3860	1722	994	585	140	110	105

Table 6.6: Breakdown of the $\mu\mu$ portion of the WZ background estimate.

the probabilities for all types of isolated and non-isolated muons appear grouped together into two sets of points. We apply the measured fake probabilities to the $W + jets$ data set, and obtain the estimates for the background contribution from QCD fakes shown in Table 6.13. The total contribution in $126\,\mathrm{pb}^{-1}$ is estimated to be 0.95 ± 0.31 events.

To investigate the contribution from semi-leptonic b quark decays to the categories with non-isolated leptons, we perform additional studies with Monte Carlo and data samples. We study ten $W + heavy\,flavor$ Monte Carlo samples, generated using the AlpGen matrix-element package and simulated with Herwig. Table 6.14 displays the results; we find expected contributions that are one to two orders of magnitude below those of the other backgrounds discussed in this section. Using two data samples enriched in b decays, we remeasure the electron and muon fake probabilities. The results are shown in Table 6.15; we do not observe any significant increase due to b jets. Examining the E_T spectrum of

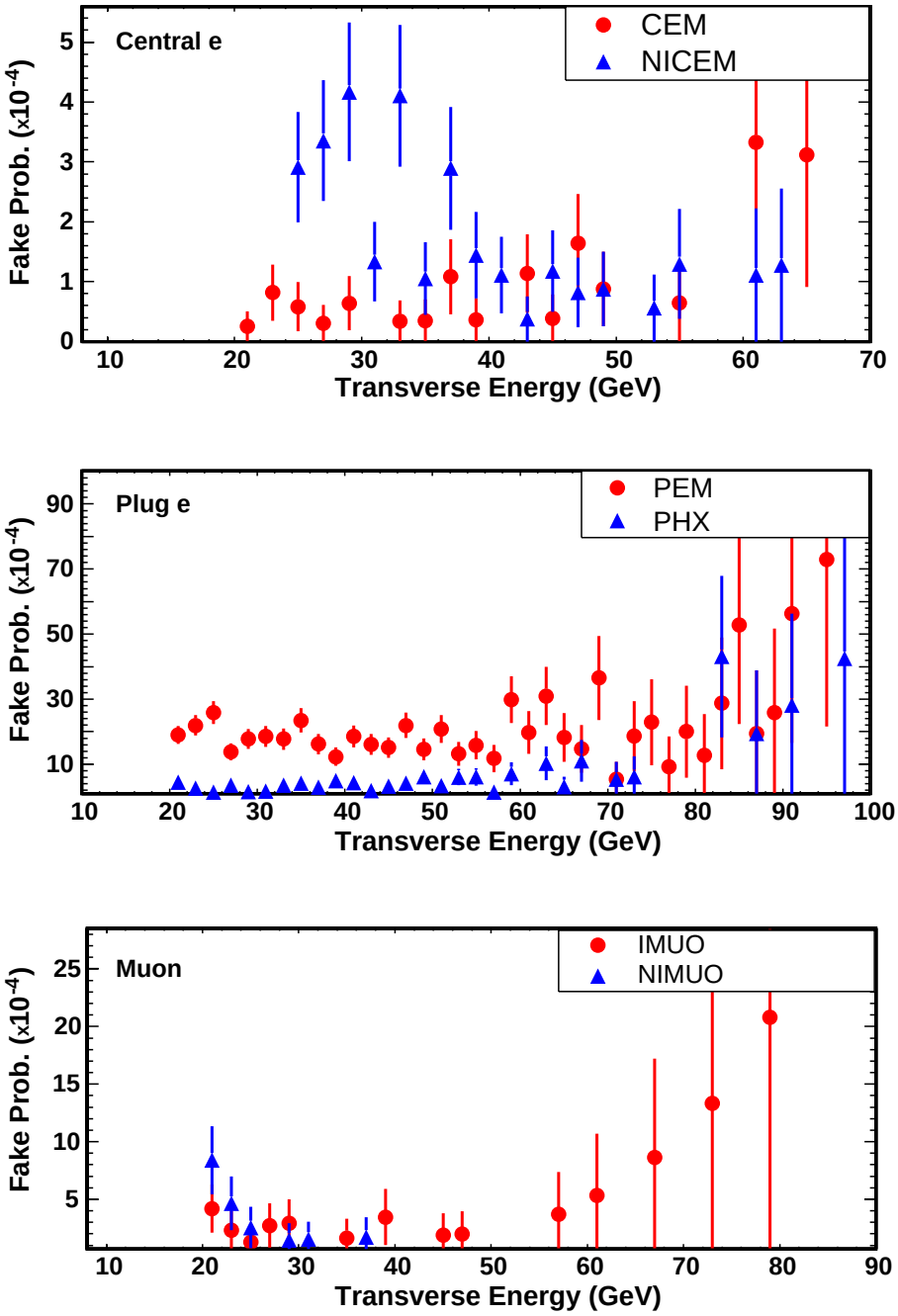

Figure 6.1: Fake probabilities for electrons and muons as a function of E_T, integrated over all η.

	Dilepton Cut						NJets				
Category	Geom-Pt	ID	iso	conv+cosm	Z veto	$\not\!\!E_T$, $\Delta\phi\,(\not\!\!E_T\,,\,\ell\,j)$	0j	1j	2j	H_T	OS
TCE/CMUP	2529	607	603	534	534	385	202	142	41	19	13
TCE/NICMUP				32	32	17	5	6	6	3	1
CMUP/NITCE				22	22	13	4	6	3	2	2
TCE/CMU	572	115	106	101	101	69	37	22	10	7	3
TCE/NICMU				3	3	2	0	1	1	1	0
TCE/CMP	713	165	152	135	135	91	55	31	5	5	3
TCE/NICMP				14	14	11	3	6	2	1	1
TCE/CMX	1417	294	291	259	259	175	91	62	22	17	7
TCE/NICMX				14	14	12	3	7	2	0	0
CMX/NITCE				13	13	11	6	3	2	2	2
TCE/CMIO	2169	289	270	267	267	199	108	63	28	21	10
PHX/CMUP	328	100	100	88	88	62	33	25	4	3	1
PHX/NICMUP				12	12	11	1	5	5	3	1
PHX/CMU	64	22	22	22	22	18	6	8	4	2	0
PHX/CMP	75	20	20	20	20	14	7	6	1	0	0
PHX/CMX	148	49	49	46	46	30	14	15	1	0	0
PHX/NICMX				3	3	2	1	0	1	0	0
PHX/CMIO	214	45	45	45	45	33	19	11	3	2	2
CMUP/PEM	939	311	304	304	304	205	108	76	21	12	12
CMX/PEM	504	140	136	136	136	102	56	35	11	5	5
Total $e\mu$	9672	2157	2098	2070	2070	1462	759	530	173	105	63

Table 6.7: Breakdown of the $e\mu$ portion of the WZ background estimate.

electrons in b decays from Monte Carlo, we test whether the kinematic requirement of $E_T > 20$ GeV is strongly reducing the effects of b jets: We lower the E_T threshold to 15 and then 10 GeV, and remeasure the fake probabilities in the QCD data samples. The results, shown in Figure 6.2, demonstrate that leptons from b decays are suppressed by the kinematic requirements enforced in the analysis.

6.4 Drell-Yan background

The Drell-Yan process refers to a lepton pair production mechanism which was first described by Sidney Drell and Tung-Mow Yan [59]. At leading-order,

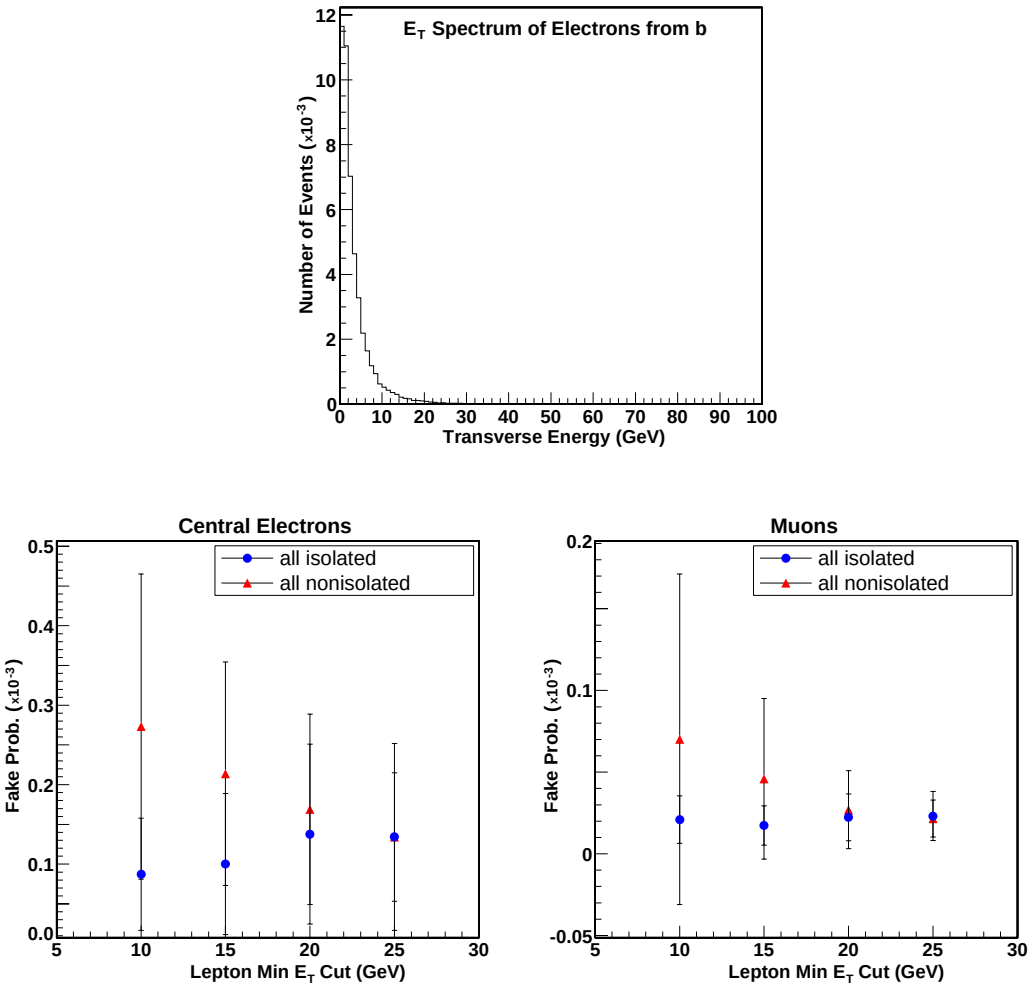

Figure 6.2: The top plot shows an E_T distribution from Monte Carlo of electrons from b decay. The bottom plots show the electron (left) and muon (right) isolated and non-isolated fake probabilities, as a function of E_T, from 10 to 25 GeV. The contribution from b quarks becomes apparent below 20 GeV, and steadily increases as the E_T threshold is lowered.

	Dilepton Cut						NJets				
Category	Geom-Pt	ID	iso	conv+cosm	Z veto	$\not\!\!E_T$, $\Delta\phi\,(\not\!\!E_T\,,\,\ell\,j)$	0j	1j	2j	H_T	OS
3ℓ	5680	5567	5449	5249	5142	3718	2979	633	106	101	–
4ℓ	16	16	14	10	9	9	8	1	0	0	–
5ℓ	0	0	0	0	0	0	0	0	0	0	–
Total 79203	46933	25230	24617	24234	16088	9225	5739	2818	665	493	330

Table 6.8: Multilepton and general summary of the WZ background estimate.

	Dilepton Cut						NJets				
Category	Geom-Pt	ID	iso	conv+cosm	Z veto	$\not\!\!E_T$, $\Delta\phi\,(\not\!\!E_T\,,\,\ell\,j)$	0j	1j	2j	H_T	OS
TCE/TCE	15822	10448	10433	9603	9576	180	30	99	51	36	36
TCE/NITCE				723	720	12	1	7	4	3	3
TCE/PHX	2911	2089	2089	1995	1985	37	5	23	9	4	4
PHX/NITCE				84	84	2	0	1	1	1	1
TCE/PEM	8498	5911	5689	5652	5634	91	16	58	17	9	9
PHX/PHX	903	740	740	740	740	3	0	3	0	0	0
PHX/PEM	1021	787	787	787	786	25	2	17	6	3	3
Total ee	29155	20015	19738	19584	19525	350	54	208	88	56	56

Table 6.9: Breakdown of the ee portion of the $Z \to \tau^+\tau^-$ background estimate.

the process is $q\overline{q} \to \gamma^*/Z \to \ell^+\ell^-$, where ℓ is an electron, muon, or tau. Drell-Yan events with ee and $\mu\mu$ final states do not have real $\not\!\!E_T$, and jets in such events must arise from gluon radiation. These jets exhibit a softer E_T spectrum than those from $t\overline{t}$ decays. In spite of these characteristics, these events are still a significant background to the dilepton analysis because the production cross-section is approximately 35 times that for $t\overline{t}$. We have introduced selection criteria to remove Drell-Yan events within the region previously excluded by the Z mass window cut, and thus consider the Drell-Yan background inside and outside the Z window separately [60].

Inside the Z window, we use the number of Z+n jet events (n = 0, 1, $\geq$ 2) in the data to normalize Monte Carlo events in each jet bin. For the 0 jet

	Dilepton Cut						NJets				
Category	Geom-Pt	ID	iso	conv+cosm	Z veto	$\not\!\!E_T$, $\Delta\phi$ ($\not\!\!E_T$, $\ell\, j$)	0j	1j	2j	H_T	OS
CMUP/CMUP	6298	3512	3502	3279	3273	42	7	23	12	8	8
CMUP/NICMUP				223	220	4	1	2	1	0	0
CMUP/CMU	2545	1341	1299	1258	1255	28	3	14	11	8	8
CMUP/NICMU				41	41	3	0	1	2	1	1
CMUP/CMP	3509	2066	1999	1946	1943	36	3	22	11	9	9
CMUP/NICMP				53	53	3	0	1	2	2	2
CMUP/CMX	5965	3115	3110	2904	2900	60	10	31	19	10	10
CMUP/NICMX				104	103	2	0	1	1	0	0
CMX/NICMUP				102	102	4	0	1	3	3	3
CMUP/CMIO	6405	2471	2389	2389	2385	48	11	25	12	5	5
CMX/CMU	1360	694	676	647	646	7	0	3	4	2	2
CMX/NICMU				29	29	1	1	0	0	0	0
CMX/CMP	1594	831	799	778	777	17	1	9	7	6	6
CMX/NICMP				21	21	0	0	0	0	0	0
CMX/CMX	1755	888	888	831	828	13	3	7	3	2	2
CMX/NICMX				57	55	0	0	0	0	0	0
CMX/CMIO	3190	1102	1066	1066	1063	36	2	26	8	4	4
Total $\mu\mu$	32621	16020	15728	15728	15694	304	42	166	96	60	60

Table 6.10: Breakdown of the $\mu\mu$ portion of the $Z \to \tau^+\tau^-$ background estimate.

case, we use an official Monte Carlo sample generated with version 6.216 of the Pythia Monte Carlo package. For n > 0 we use official samples of Z+n partons, generated with the AlpGen matrix element Monte Carlo package. The Monte Carlo samples, however, do not model the high tails of the $\not\!\!E_T$ distribution well, which is the region of interest. We apply scale factors, defined as the ratio of the area above $\not\!\!E_T$ = 25 GeV in the data to the area above $\not\!\!E_T$ = 25 GeV in the Monte Carlo, where the expected contributions to the data from WW, $Z \to \tau^+\tau^-$, and $t\bar{t}$ processes are first subtracted. We then extract the efficiency of the $\not\!\!E_T$, jet significance, and H_T requirements from the corrected Monte Carlo samples. Table 6.16 shows the expected background contribution to the ee and $\mu\mu$ channels. We estimate a total contribution of 0.34 ± 0.22 events inside the Z window.

Outside the Z window, we employ the following procedure to estimate the background contribution from Drell-Yan events:

	Dilepton Cut						NJets				
Category	Geom-Pt	ID	iso	conv+cosm	Z veto	$\not\!\!E_T$, $\Delta\phi\,(\not\!\!E_T\,,\,\ell\,j)$	0j	1j	2j	H_T	OS
TCE/CMUP	19937	12165	12147	11312	11312	211	28	121	62	38	38
TCE/NICMUP				374	374	8	0	7	1	1	1
CMUP/NITCE				419	419	13	0	4	9	7	7
TCE/CMU	4237	2522	2444	2341	2341	51	14	26	11	6	6
TCE/NICMU				95	95	2	1	0	1	0	0
TCE/CMP	5441	3401	3267	3141	3141	60	15	27	18	13	13
TCE/NICMP				106	106	6	0	2	4	0	0
TCE/CMX	9676	5596	5577	5196	5196	107	11	59	37	20	20
TCE/NICMX				188	188	5	0	3	2	2	2
CMX/NITCE				161	161	3	0	1	2	2	2
TCE/CMIO	10471	4507	4364	4344	4344	69	7	45	17	10	10
PHX/CMUP	1738	1004	1004	979	979	8	0	5	3	2	1
PHX/NICMUP				25	25	0	0	0	0	0	0
PHX/CMU	377	221	221	217	217	3	0	2	1	1	1
PHX/NICMU				4	4	0	0	0	0	0	0
PHX/CMP	459	286	286	276	276	4	0	2	2	1	1
PHX/NICMP				10	10	1	0	1	0	0	0
PHX/CMX	935	589	589	567	567	8	0	4	4	2	2
PHX/NICMX				22	22	0	0	0	0	0	0
PHX/CMIO	1880	817	817	817	817	6	1	3	2	2	2
CMUP/PEM	4991	2922	2837	2837	2837	42	2	26	14	7	7
CMX/PEM	3678	2267	2195	2195	2195	45	8	25	12	8	8
Total $e\mu$	63820	36297	35748	35626	35626	652	87	363	202	122	121

Table 6.11: Breakdown of the $e\mu$ portion of the $Z\to\tau^+\tau^-$ background estimate.

1. In the data, we determine the ratio (after lepton ID requirements but before other analysis cuts) of the number of events inside the Z window to the number outside. The strategy is to use this ratio to rescale the number of events inside the Z window which pass all analysis requirements, and thereby estimate the number of background events in the regions outside. This is expressed as

$$N_{out}^{bgd} = N_{in}^{pass} \times \left(\frac{N_{low} + N_{high}}{N_{in}} \right) ,$$

where the fraction is computed before high level analysis requirements are applied. This fraction is too simple, however, as it ignores both the contribution to N_{in}^{pass} from $t\bar{t}$, which is non-negligible, and correlations between

	Dilepton Cut						NJets				
Category	Geom-Pt	ID	iso	conv+cosm	Z veto	$\not\!\!E_T$, $\Delta\phi\,(\not\!\!E_T\,,\,\ell\,j)$	0j	1j	2j	H_T	OS
3ℓ	81	81	75	64	62	16	10	6	0	0	–
4ℓ	0	0	0	0	0	0	0	0	0	0	–
5ℓ	0	0	0	0	0	0	0	0	0	0	–
Total 422363	125677	72413	71289	71002	70907	1322	193	743	386	238	237

Table 6.12: Multilepton and general summary of $Z \to \tau^+\tau^-$ background estimate.

	0 jet	1 jet	$\geq$ 2 jets	After H_T	After OS
TCE	0.27 ± 0.03	0.17 ± 0.02	0.13 ± 0.01	0.07 ± 0.01	0.03 ± 0.01
NITCE	1.47 ± 0.08	0.93 ± 0.05	0.59 ± 0.03	0.30 ± 0.02	0.15 ± 0.01
PEM	4.33 ± 0.15	3.13 ± 0.15	1.29 ± 0.07	0.65 ± 0.03	0.65 ± 0.03
PHX	0.99 ± 0.07	0.64 ± 0.06	0.25 ± 0.03	0.13 ± 0.01	0.06 ± 0.01
IMUO	0.28 ± 0.03	0.27 ± 0.03	0.14 ± 0.01	0.07 ± 0.01	0.04 ± 0.01
NIMUO	0.24 ± 0.03	0.20 ± 0.02	0.09 ± 0.01	0.05 ± 0.01	0.02 ± 0.01
Total	7.58 ± 0.19	5.35 ± 0.17	2.50 ± 0.08	1.26 ± 0.04	0.95 ± 0.03

Table 6.13: Estimated contributions to dilepton backgrounds from QCD fakes in $126\,\mathrm{pb}^{-1}$. The errors are statistical only.

the invariant mass of the lepton pair and the other analysis requirements.

2. We estimate the contribution from $t\bar{t}$ with the same Monte Carlo sample used to determine the acceptance, assuming a theoretical cross-section of $\sigma_{t\bar{t}} = 6.7$ pb.

3. Using Monte Carlo samples, we calculate the fraction of events which pass the $\not\!\!E_T$, two-jet, and H_T requirements in each invariant mass region, and obtain the following nine factors:

$$\left[\epsilon^{low}_{\not\!\!E_T}, \epsilon^{low}_{2j}, \epsilon^{low}_{H_T}\right], \left[\epsilon^{in}_{\not\!\!E_T}, \epsilon^{in}_{2j}, \epsilon^{in}_{H_T}\right], \left[\epsilon^{high}_{\not\!\!E_T}, \epsilon^{high}_{2j}, \epsilon^{high}_{H_T}\right].$$

Sample	# events	Sample	# events
$W(\mu\nu)bb0p$	0.0022	$W(e\nu)cc0p$	0.064
$W(e\nu)bb0p$(old)	0.0066	$W(\mu\nu)cc0p$	0.038
$W(e\nu)bb0p$(new)	0.0035	$W(e\nu)c0p$	0.070
$W(e\nu)bb1p$	0.0046	$W(\mu\nu)c0p$	< 0.012
$W(e\nu)c1p$	0.0043	$W(\mu\nu)c1p$	0.026

Table 6.14: Expected contribution of fakes in 100 pb^{-1} from ten different $Wb\bar{b}$ Monte Carlo samples.

Lepton type	Fakes	# of b jets (+tracks)	Fake prob.
NICMUP	1	21,347	4.7×10^{-5}
NICMU	0	21,347	$< 4.7 \times 10^{-5}$
NICMP	1	21,347	4.7×10^{-5}
NICMX	0	21,347	$< 4.7 \times 10^{-5}$
NITCE	3	20,528	1.5×10^{-4}

Table 6.15: Fake probabilities of non-isolated leptons determined from a b-enriched data sample.

4. We correct the expression for N_{out}^{bgd} using these factors, and obtain:

$$N_{out}^{bgd} = \left(N_{in}^{pass} - N_{in}^{t\bar{t}}\right) \times \left(\frac{\epsilon_{\not{E}_T}^{low} \cdot \epsilon_{2j}^{low} \cdot \epsilon_{H_T}^{low} \cdot N_{low} + \epsilon_{\not{E}_T}^{high} \cdot \epsilon_{2j}^{high} \cdot \epsilon_{H_T}^{high} \cdot N_{high}}{\epsilon_{\not{E}_T}^{in} \cdot \epsilon_{2j}^{in} \cdot \epsilon_{H_T}^{in} \cdot N_{in}}\right)$$

   Note that this procedure does not rely on the Monte Carlo samples to predict absolute $\not{E}_T$ efficiencies, but rather the ratio of these efficiencies in the different invariant mass regions.

Table 6.17 shows the expected background contribution to the ee and $\mu\mu$ channels. We estimate a total contribution of 0.86 ± 0.55 events outside the Z window.

Combining the results for the invariant mass regions, we arrive at a total estimate for the Drell-Yan background contribution in 126 pb^{-1} of 1.20 ± 0.60 events.

Category	Expected # of events after all analysis requirements
ee	0.14 ± 0.08
$\mu\mu$	0.19 ± 0.12
Total inside	0.34 ± 0.15

Table 6.16: Drell-Yan background estimate for 126 pb^{-1} inside the Z window. The errors are statistical only.

Category	Expected # of events after all analysis requirements
ee	0.32 ± 0.24
$\mu\mu$	0.54 ± 0.50
Total outside	0.86 ± 0.55

Table 6.17: Drell-Yan background estimate for 126 pb^{-1} outside the Z window. The errors are statistical only.

6.5 Systematic uncertainties

We estimate systematic uncertainties for the WW and WZ processes due to Monte Carlo generators and the jet energy scale [55]. For Monte Carlo generators, we compare the estimates obtained with the default Pythia sample to those obtained with an AlpGen+Herwig sample. Since the Pythia generator has been extensively tested at CDF and the AlpGen+Herwig combination is new, we take the central value for the backgroud estimate from the Pythia sample. We take half the difference between the two estimates and assign a systematic uncertainty of 40%. For the jet energy scale, we compare the estimates obtained with the default set of jet corrections to those obtained with the shifted jet corrections ($\pm 1\sigma$) used to estimate the systematic uncertainty on the $t\bar{t}$ acceptance. We take half the difference between the estimates seen with the two shifted values, and divide by the estimate obtained with the default set of jet corrections to arrive

at a systematic uncertainty of 17%.

For $Z \to \tau^+\tau^-$ events, the largest sources of systematic uncertainty are due to the jet energy scale and the efficacy of the two-jet requirement. For the jet energy scale, we follow the same procedure used for the diboson processes, and obtain a systematic uncertainty of 32%. For the two-jet requirement, we determine the ratio (data to Monte Carlo) of the number of events with ≥ 2 jets under the Z peak, and multiply by this fraction to correct the number of background events with ≥ 2 jets in the $Z \to \tau^+\tau^-$ sample. This corresponds to a 10% systematic uncertainty from the two-jet requirement.

For QCD fakes, we estimate systematic uncertainties for each lepton type separately [58]. We use the measured fake probabilities to predict the number of fake leptons present in alternate QCD samples which were not used to measure the probabilities. Specifically, we take half of the largest difference seen between the predicted and observed number of fake leptons in each of the alternate QCD samples, and use these values as estimates for the systematic uncertainty. We find values between 21 and 50% depending on lepton type; the results are shown in Table 6.18.

Lepton type	Assigned systematic uncertainty
TCE	50%
NITCE	25%
PEM	35%
PHX	21%
IMUO	35%
NIMUO	25%

Table 6.18: Systematic uncertainties for each lepton type for the background estimate from QCD fakes.

For the Drell-Yan background estimate, we assign systematic uncertainties due to the jet energy scale and to the method itself [60]. To obtain the contri-

bution from the jet energy scale we use the same procedure as for the $Z \to \tau^+\tau^-$ estimate, and find a systematic uncertainty of 32%. The method used to obtain the background estimate inside the Z window employs scale factors which are calculated from the tails of $\not\!\!E_T$ distributions. These are subject to large statistical fluctuations in the data. We calculate a representative scale factor, and apply an additional uncertainty such that all scale factors are consistent with this value within errors. We assign this as a systematic uncertainty to the estimate for inside the Z window, and obtain a value of 50%.

A summary of the systematic uncertainties assigned to all of the background estimates is shown in Table 6.19.

Background	Source	Uncertainty [%]
WW/WZ	Monte Carlo generator	40
	Jet energy scale	17
$Z \to \tau^+\tau^-$	Two-jet requirement	10
	Jet energy scale	32
Drell-Yan (ee, $\mu\mu$)	Method	50
	Jet energy scale	32
QCD fakes	Method	21-50

Table 6.19: Summary of systematic uncertainties assigned to the background estimates.

6.6 Total expected background

Combining all of the estimates, we arrive at a total predicted background in $126\,\mathrm{pb}^{-1}$ of 2.9 ± 0.8 events, including statistical and systematic uncertainties. The largest contributions are from Drell-Yan and QCD fakes, as shown in Table 6.20.

Source	Predicted events in $126\,\mathrm{pb}^{-1}$
WW/WZ	0.40 ± 0.17
$Z \to \tau^+\tau^-$	0.32 ± 0.11
QCD fakes	0.95 ± 0.31
Drell-Yan (ee, $\mu\mu$)	1.20 ± 0.70
Total	2.87 ± 0.79

Table 6.20: Total predicted background from each process in $126\,\mathrm{pb}^{-1}$ including statistical and systematic uncertainties.

CHAPTER 7

Results

Assembling the estimates discussed in the previous chapters of the acceptance, backgrounds, efficiencies, and scale factors, we present the measured $t\bar{t}$ cross-section using the definition from Equation 1.1:

$$\sigma_{t\bar{t}} = \frac{\mathrm{N_{signal}} - \mathrm{N_{background}}}{\mathcal{A}_{\mathrm{total}} \cdot \int \mathcal{L}\ dt},$$

where $\mathcal{L}$ is the instantaneous luminosity and $\mathcal{A}_{\mathrm{total}}$ represents the product of the acceptance, scale factors, and trigger and lepton identification efficiencies. The total integrated luminosity is estimated using Cerenkov Luminosity Counters (CLCs), which measure the flux of particles at high pseudorapidity ($3.75 < |\eta| < 4.75$) from $p\bar{p}$ ineleastic scattering [61]. The data sets for this analysis correspond to $(125.8 \pm 7.5)\,\mathrm{pb}^{-1}$, where the uncertainty of 6% is derived from studies of:

- The total $p\bar{p}$ inelastic cross-section (measured in Run I and scaled to Run II energy).
- The CLC acceptance to $p\bar{p}$ inelastic processes.
- Detector stability.

Accounting for the specific integrated luminosities of the different detector sys-

tems, we arrive at a total denominator of

$$\mathcal{A}_{\text{total}} \cdot \int \mathcal{L}\, dt = (0.935 \pm 0.099_{syst} \pm 0.056_{lum})\,\text{pb}^{-1}.$$

We search for dilepton candidates in the data by applying the event selection procedure described in chapter 5 to the three primary data sets (also described in chapter 5), and find a total of 10 candidates (2 ee, 5 $e\mu$, 3 $\mu\mu$). A list of the candidate run and event numbers is given here in Table 7.1. Tables 7.2 – 7.6 show

Analysis category	Run number	Event number
TCE/TCE*	153374	2276742
TCE/PEM*	154208	966753
CMUP/NITCE*	151978	507773
TCE/CMP	143257	760520
TCE/CMX	155114	478702
TCE/CMX*	156484	3099305
TCE/CMIO	161633	963604
CMUP/CMP**	162820	7050764
CMUP/CMX*	154654	7344016
CMX/CMX	153325	599511

Table 7.1: Run and event numbers for the candidate events. Events with a * have a tagged b jet; events with a ** are double tagged.

an exhaustive breakdown of predicted signal, backgrounds, and observed events from the three primary data sets. These summary tables are fully corrected for lepton ID efficiency scale factors, trigger efficiencies, and the different integrated luminosities which correspond to each of the allowed analysis categories. Our measurement yields

$$\sigma_{t\bar{t}} = (7.6 \pm 3.4\, stat. \pm 1.5\, syst.)\,\text{pb}.$$

The latest theoretical prediction (NLO, with NLL gluon resummation) is [18]

$$\sigma_{t\bar{t}} = (6.7 \pm 0.5)\,\text{pb}.$$

Overall summaries of the analysis are shown in Table 7.7. Figures 7.1 – 7.7 show distributions of several kinematic variables from the 10 events, compared with the expected contribution from backgrounds and Standard Model $t\bar{t}$. In the plots the $t\bar{t}$ contribution is shown normalized to the theoretical prediction of 6.7 pb. The p_T distribution, shown in Figure 7.3, appears to disagree with the Standard Model prediction in the lowest bin (20 – 40 GeV). This discrepancy could be simply a statistical fluctuation, or could be due to a number of other factors, such as poor modeling in the Monte Carlo samples, incorrect treatment of structure functions, or the influence of new phenomena beyond the Standard Model[1]. The plots shown in Figure 7.7 of the $\Delta\phi$ vs. $\not\!\!E_T$ distributions from this analysis and the Run I measurement [62] are of particular interest: The distribution from the Run I analysis exhibited an intriguing number of $e\mu$ events with large $\not\!\!E_T$, and was a motivating factor for becoming involved with the analysis in Run II; the distribution obtained from this analysis, however, shows excellent agreement with the Standard Model.

7.1 b-tagged events

For this analysis we do not require any jets to have displaced secondary vertices as part of our selection criteria. Nevertheless, we observe 6 events with b-tags, where 5.5 are predicted. One $\mu\mu$ (CMUP/CMP) event is double tagged.

[1]Indications from recent studies at CDF with a newer 74 pb^{-1} of data are that this is simply a statistical fluctuation, which is disappearing.

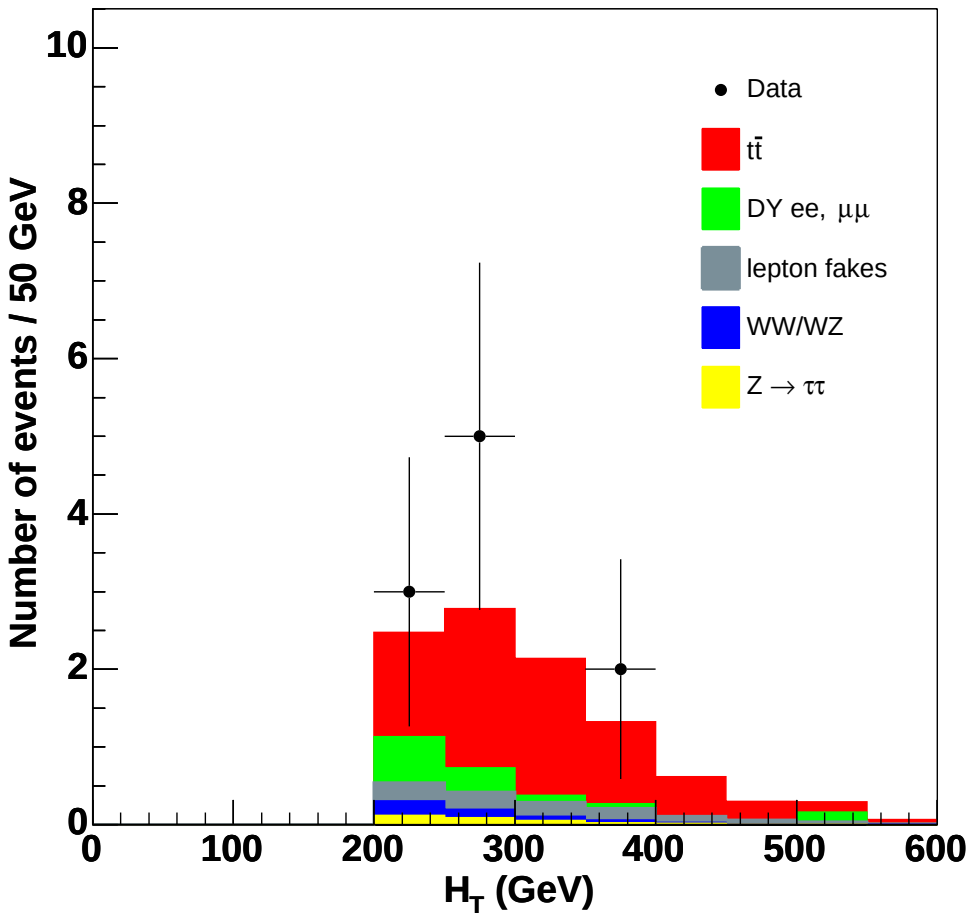

Figure 7.1: H_T distribution of the dilepton candidiates compared with the Standard Model prediction.

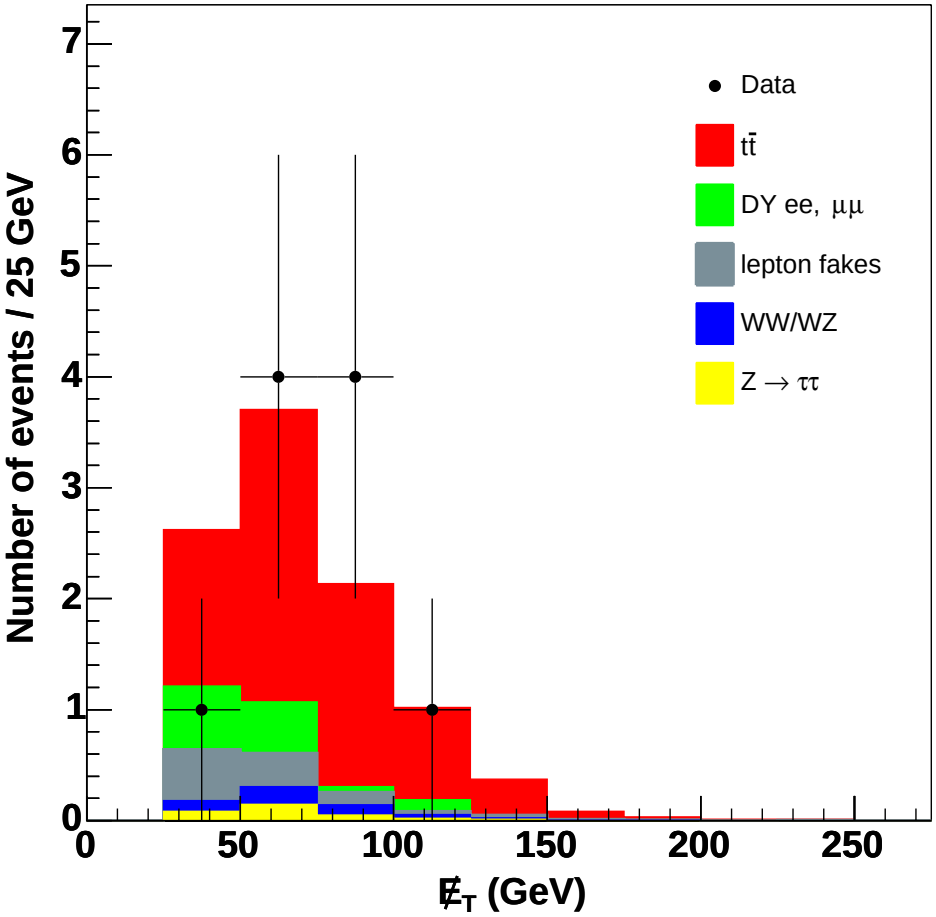

Figure 7.2: $\not{E}_T$ distribution of the dilepton candidates compared with the Standard Model prediction.

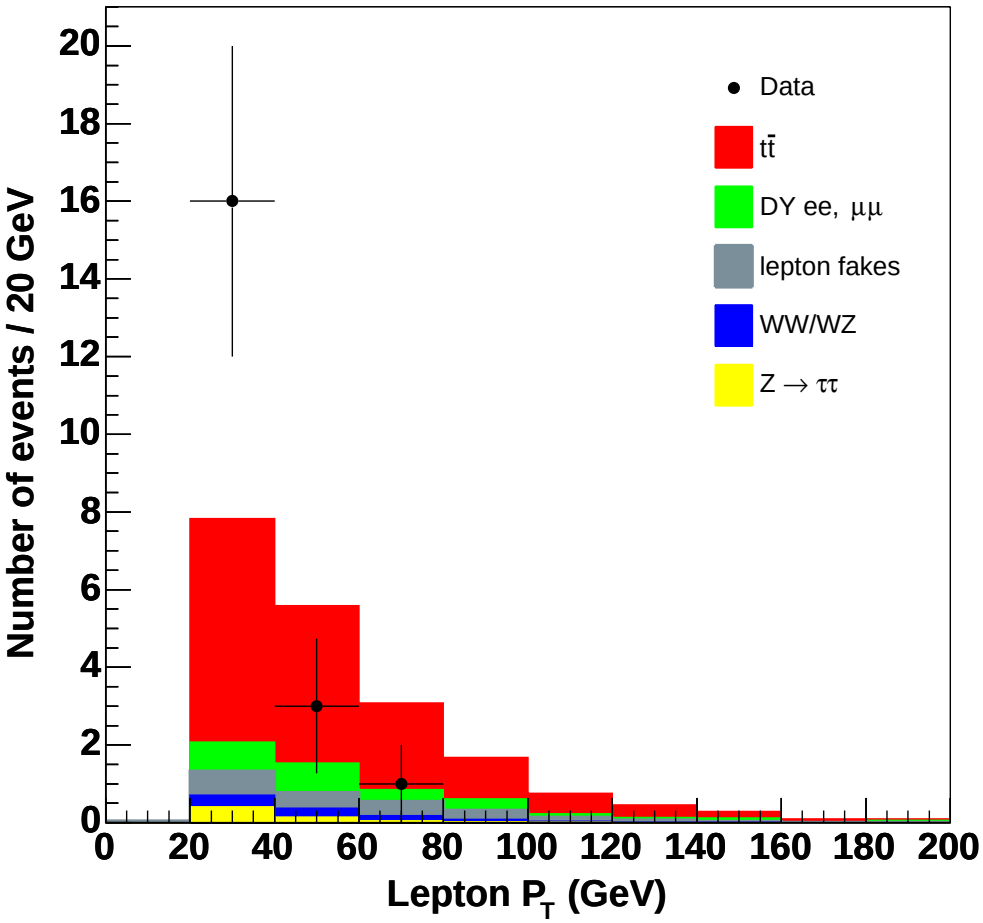

Figure 7.3: Lepton p_T distribution of the dilepton candidates compared with the Standard Model prediction.

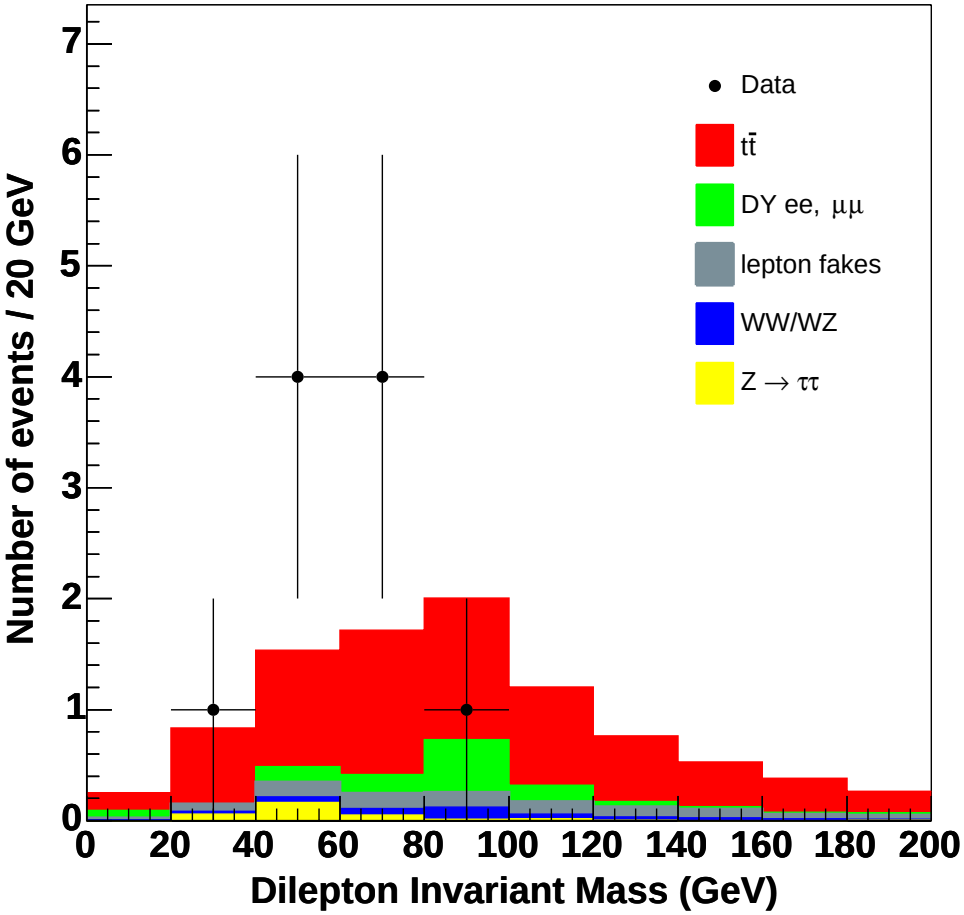

Figure 7.4: Invariant mass distribution of the dilepton candidates compared with the Standard Model prediction.

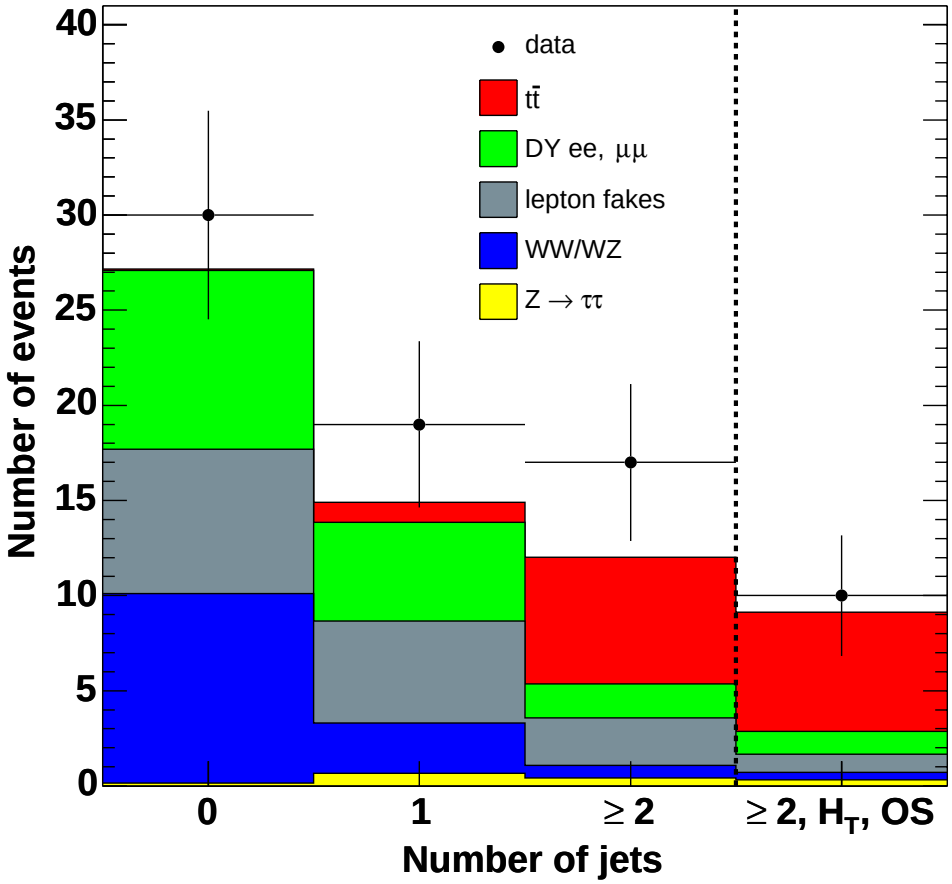

Figure 7.5: Distribution of the number of jets in the candidate events compared with the Standard Model prediction.

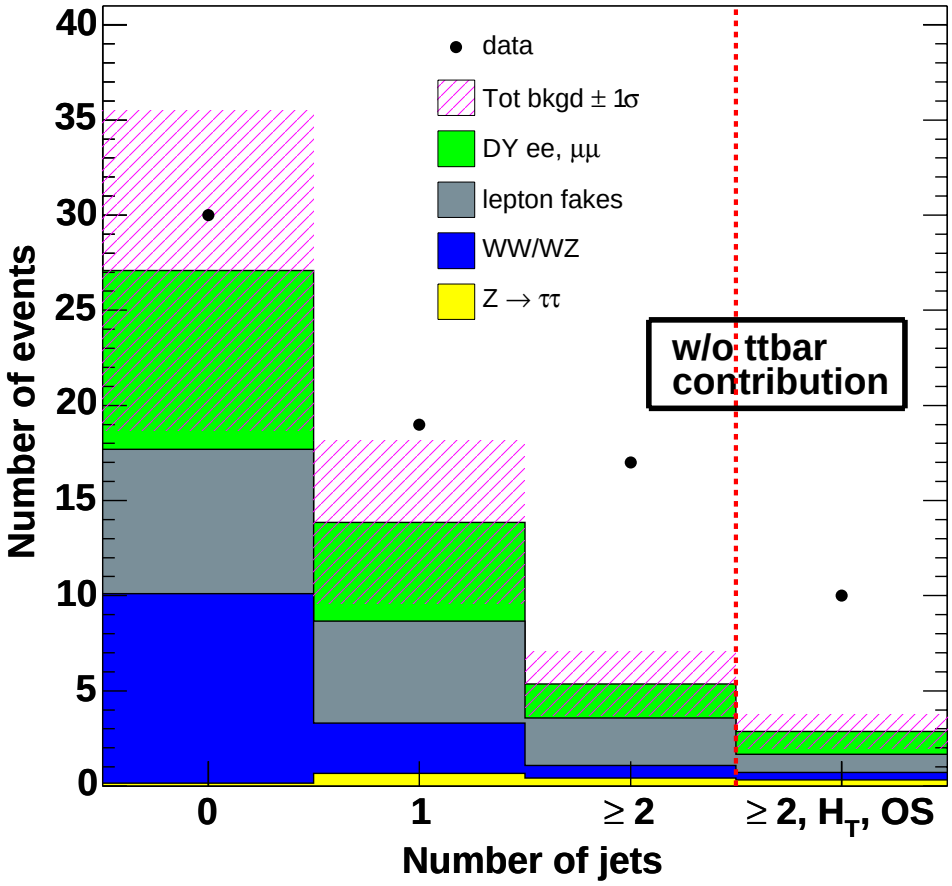

Figure 7.6: Distribution of the number of jets in the candidate events compared with the predicted Standard Model backgrounds. (No expected contribution from $t\bar{t}$ is shown.) The $\pm 1\sigma$ uncertainty on the total predicted background is indicated by the hatched fill pattern.

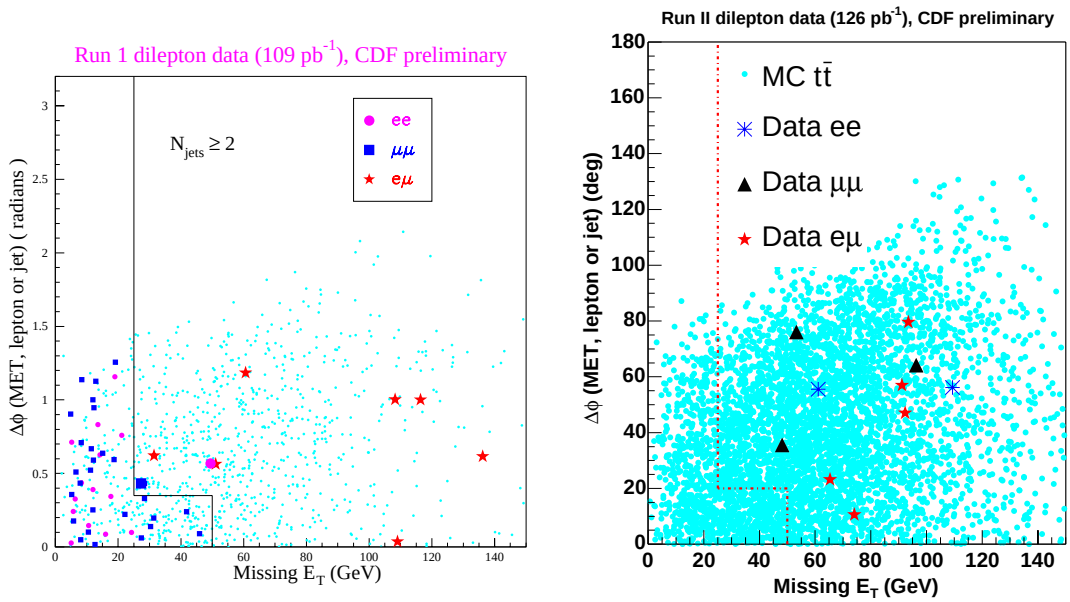

Figure 7.7: $\Delta\phi$ vs. $\not\!\!E_T$ distribution(s) of the dilepton candidates compared with the Standard Model prediction. The distribution from the Run I analysis is shown in the left-hand plot, and that from this analysis in the right-hand plot. The intriguing number of $e\mu$ events with large $\not\!\!E_T$ in the Run I distribution are not seen in this analysis.

	NJets				
Category	0j	1j	$\geq$ 2j	$H_T > 200$ GeV	OS
ee					
WW/WZ	1.29	0.39	0.10	0.07	0.06
$Z \to \tau\overline{\tau}$	0.02	0.09	0.06	0.05	0.05
Drell-Yan	2.74 ± 1.27	1.37 ± 0.60	0.35 ± 0.20	0.15 ± 0.10	0.18 ± 0.10
QCD fakes	0.11 ± 0.02	0.06 ± 0.01	0.04 ± 0.01	0.02 ± 0.00	0.01 ± 0.00
Background	4.16 ± 0.27	1.91 ± 0.60	0.55 ± 0.20	0.29 ± 0.10	0.30 ± 0.10
Expected signal	0.02 ± 0.01	0.14 ± 0.02	0.91 ± 0.04	0.89 ± 0.04	0.89 ± 0.04
Data	4	2	1	1	1
$\mu\mu$					
WW/WZ	1.99	0.53	0.10	0.08	0.08
$Z \to \tau\overline{\tau}$	0.03	0.14	0.09	0.07	0.07
Drell-Yan	1.18 ± 1.18	1.08 ± 0.98	0.73 ± 0.59	0.72 ± 0.55	0.72 ± 0.55
QCD fakes	0.11 ± 0.02	0.11 ± 0.02	0.05 ± 0.01	0.02 ± 0.00	0.01 ± 0.00
Background	3.31 ± 0.18	1.86 ± 0.98	0.97 ± 0.59	0.89 ± 0.55	0.88 ± 0.55
Expected signal	0.01 ± 0.00	0.22 ± 0.02	1.30 ± 0.05	1.25 ± 0.05	1.25 ± 0.05
Data	2	2	4	4	4
$e\mu$					
WW/WZ	3.22	0.69	0.12	0.13	0.1
$Z \to \tau\overline{\tau}$	0.07	0.24	0.15	0.12	0.12
QCD fakes	0.22 ± 0.03	0.19 ± 0.03	0.10 ± 0.01	0.04 ± 0.00	0.03 ± 0.00
Background	3.51 ± 0.03	1.12 ± 0.01	0.37 ± 0.01	0.29 ± 0.00	0.25 ± 0.00
Expected signal	0.02 ± 0.01	0.39 ± 0.03	2.61 ± 0.07	2.52 ± 0.07	2.52 ± 0.07
Data	1	0	5	4	4

Table 7.2: Central (isolated) + central (isolated) summary.

The run and event numbers of the candidates with b tags are denoted with an asterisk in Table 7.1.

	NJets				
Category	0j	1j	$\geq$ 2j	$H_T > 200$ GeV	OS
ee					
WW/WZ	0.06	0.02	0.01	0.01	0.01
$Z \to \tau\overline{\tau}$	0.00	0.01	0.00	0.00	0.00
Drell-Yan	0.11 ± 0.05	0.06 ± 0.03	0.02 ± 0.01	0.01 ± 0.00	0.01 ± 0.00
QCD fakes	0.68 ± 0.07	0.39 ± 0.04	0.24 ± 0.02	0.12 ± 0.01	0.06 ± 0.00
Background	0.85 ± 0.09	0.48 ± 0.05	0.27 ± 0.02	0.14 ± 0.01	0.08 ± 0.00
Expected signal	0.01 ± 0.00	0.04 ± 0.01	0.10 ± 0.01	0.09 ± 0.01	0.08 ± 0.01
Data	1	1	0	0	0
$\mu\mu$					
WW/WZ	0.05	0.04	0.01	0.01	0.01
$Z \to \tau\overline{\tau}$	0.00	0.00	0.01	0.01	0.01
Drell-Yan	0.02 ± 0.02	0.02 ± 0.02	0.02 ± 0.01	0.02 ± 0.02	0.02 ± 0.02
QCD fakes	0.10 ± 0.02	0.08 ± 0.01	0.04 ± 0.01	0.02 ± 0.00	0.01 ± 0.00
Background	0.17 ± 0.03	0.14 ± 0.02	0.08 ± 0.01	0.06 ± 0.02	0.05 ± 0.02
Expected signal	0.00 ± 0.00	0.00 ± 0.00	0.14 ± 0.02	0.14 ± 0.02	0.12 ± 0.01
Data	0	0	0	0	0
$e\mu$					
WW/WZ	0.10	0.06	0.02	0.01	0.01
$Z \to \tau\overline{\tau}$	0.00	0.01	0.01	0.01	0.01
QCD fakes	0.67 ± 0.05	0.41 ± 0.03	0.23 ± 0.02	0.11 ± 0.01	0.06 ± 0.00
Background	0.77 ± 0.05	0.48 ± 0.03	0.26 ± 0.02	0.13 ± 0.01	0.08 ± 0.00
Expected signal	0.01 ± 0.00	0.01 ± 0.00	0.30 ± 0.02	0.29 ± 0.02	0.27 ± 0.02
Data	0	0	1	1	1

Table 7.3: Central (isolated) + central (non-isolated) summary.

	NJets				
Category	0j	1j	$\geq$ 2j	$H_T > 200$ GeV	OS
ee					
WW/WZ	1.71	0.54	0.12	0.07	0.07
$Z \to \tau\tau$	0.02	0.10	0.04	0.02	0.02
Drell-Yan	5.28 ± 1.92	2.64 ± 0.91	0.68 ± 0.30	0.30 ± 0.15	0.30 ± 0.15
QCD fakes	3.64 ± 0.15	2.59 ± 0.14	1.16 ± 0.06	0.59 ± 0.03	0.52 ± 0.02
Background	10.65 ± 1.93	5.87 ± 0.92	2.00 ± 0.31	0.98 ± 0.15	0.91 ± 0.15
Expected signal	0.00 ± 0.00	0.10 ± 0.01	0.53 ± 0.03	0.51 ± 0.03	0.49 ± 0.03
Data	13	8	5	1	1
$e\mu$					
WW/WZ	1.50	0.33	0.07	0.04	0.04
$Z \to \tau\overline{\tau}$	0.01	0.07	0.05	0.04	0.04
QCD fakes	1.80 ± 0.08	1.27 ± 0.07	0.46 ± 0.04	0.24 ± 0.01	0.21 ± 0.01
Background	3.31 ± 0.08	1.67 ± 0.07	0.58 ± 0.04	0.32 ± 0.01	0.29 ± 0.01
Expected signal	0.01 ± 0.00	0.09 ± 0.01	0.62 ± 0.03	0.58 ± 0.03	0.54 ± 0.03
Data	9	7	0	0	0

Table 7.4: Central/plug (both isolated) + plug/plug (both isolated) summary.

	NJets				
Category	0j	1j	$\geq$ 2j	$H_T > 200$ GeV	OS
ee					
WW/WZ	0.02	0.01	0.00	0.00	0.00
$Z \to \tau\overline{\tau}$	0.00	0.00	0.00	0.00	0.00
Drell-Yan	0.06 ± 0.03	0.03 ± 0.01	0.01 ± 0.01	0.00 ± 0.00	0.00 ± 0.00
QCD fakes	0.23 ± 0.02	0.23 ± 0.03	0.17 ± 0.02	0.09 ± 0.01	0.04 ± 0.00
Background	0.31 ± 0.04	0.27 ± 0.03	0.18 ± 0.02	0.09 ± 0.01	0.04 ± 0.00
Expected signal	0.00	0.01 ± 0.00	0.02 ± 0.01	0.02 ± 0.01	0.02 ± 0.01
Data	0	0	0	0	0
$e\mu$					
WW/WZ	0.01	0.01	0.01	0.01	0.00
$Z \to \tau\overline{\tau}$	0.00	0.00	0.00	0.00	0.00
QCD fakes	0.02 ± 0.00	0.02 ± 0.00	0.01 ± 0.00	0.00 ± 0.00	0.00 ± 0.00
Background	0.03 ± 0.00	0.03 ± 0.00	0.02 ± 0.00	0.01 ± 0.00	0.00 ± 0.00
Expected signal	0.00 ± 0.00	0.00 ± 0.00	0.04 ± 0.01	0.04 ± 0.01	0.03 ± 0.01
Data	0	0	0	0	0

Table 7.5: Central (non-isolated) + plug (isolated) summary.

	NJets				
Category	0j	1j	$\geq$ 2j	$H_T > 200$ GeV	OS
ee					
WW/WZ	3.07 ± 1.23	0.97 ± 0.39	0.23 ± 0.10	0.15 ± 0.04	0.14 ± 0.04
$Z \to \tau\overline{\tau}$	0.05 ± 0.01	0.20 ± 0.07	0.10 ± 0.03	0.08 ± 0.02	0.07 ± 0.02
Drell-Yan	8.20 ± 2.43	4.10 ± 1.8	1.05 ± 0.36	0.46 ± 0.29	0.46 ± 0.29
QCD fakes	4.80 ± 0.17	3.40 ± 0.18	1.66 ± 0.07	0.85 ± 0.03	0.64 ± 0.02
Background	16.12 ± 2.73	8.67 ± 1.85	3.04 ± 0.38	1.54 ± 0.29	1.31 ± 0.29
Expected signal	0.03 ± 0.01	0.30 ± 0.04	1.63 ± 0.17	1.58 ± 0.16	1.54 ± 0.15
Data	17	12	7	2	2
$\mu\mu$					
WW/WZ	2.04 ± 0.16	0.57 ± 0.23	0.14 ± 0.05	0.09 ± 0.04	0.09 ± 0.04
$Z \to \tau\overline{\tau}$	0.03 ± 0.01	0.14 ± 0.04	0.10 ± 0.03	0.08 ± 0.02	0.08 ± 0.02
Drell-Yan	1.20 ± 1.18	1.10 ± 0.98	0.74 ± 0.59	0.73 ± 0.56	0.73 ± 0.56
QCD fakes	0.21 ± 0.03	0.19 ± 0.02	0.09 ± 0.01	0.04 ± 0.00	0.02 ± 0.00
Background	3.48 ± 1.19	2.00 ± 1.01	1.07 ± 0.59	0.94 ± 0.56	0.92 ± 0.56
Expected signal	0.01 ± 0.00	0.22 ± 0.03	1.45 ± 0.14	1.39 ± 0.14	1.37 ± 0.14
Data	2	1	3	3	3
$e\mu$					
WW/WZ	4.83 ± 1.93	1.10 ± 0.44	0.29 ± 0.12	0.19 ± 0.08	0.17 ± 0.08
$Z \to \tau\overline{\tau}$	0.08 ± 0.02	0.33 ± 0.10	0.21 ± 0.07	0.17 ± 0.06	0.17 ± 0.06
QCD fakes	2.67 ± 0.10	1.87 ± 0.08	0.78 ± 0.05	0.37 ± 0.01	0.30 ± 0.01
Background	7.58 ± 1.93	3.30 ± 0.46	1.28 ± 0.15	0.73 ± 0.10	0.64 ± 0.10
Expected signal	0.04 ± 0.01	0.52 ± 0.06	3.56 ± 0.36	3.42 ± 0.35	3.36 ± 0.35
Data	11	6	7	6	5

Table 7.6: Total summary (all categories, isolated + non-isolated).

Source	Events per 126 pb^{-1} after all cuts			
	ee	$\mu\mu$	$e\mu$	$\ell\ell$
WW/WZ	0.14 ± 0.06	0.09 ± 0.04	0.17 ± 0.07	0.40 ± 0.17
Drell-Yan	0.46 ± 0.29	0.73 ± 0.56	-	1.2 ± 0.7
$Z \to \tau\overline{\tau}$	0.07 ± 0.02	0.08 ± 0.03	0.17 ± 0.06	0.32 ± 0.11
QCD Fakes	0.64 ± 0.21	0.02 ± 0.007	0.30 ± 0.10	0.95 ± 0.31
Total Background	1.31 ± 0.36	0.92 ± 0.56	0.64 ± 0.14	2.9 ± 0.8
$t\overline{t}$	1.54 ± 0.16	1.37 ± 0.15	3.36 ± 0.36	6.3 ± 0.7
Total SM expectation	2.85 ± 0.44	2.29 ± 0.33	4.00 ± 0.41	9.2 ± 1.1
Run II data	2	3	5	10

Source	N jets			
	0j	1j	$\geq$ 2j	H_T, OS
WW/WZ	9.94 ± 4.22	2.64 ± 0.48	0.66 ± 0.28	0.40 ± 0.17
Drell-Yan	9.4 ± 5.7	5.2 ± 3.3	1.8 ± 1.1	1.2 ± 0.7
$Z \to \tau\overline{\tau}$	0.16 ± 0.06	0.67 ± 0.23	0.41 ± 0.14	0.32 ± 0.11
Fakes	7.68 ± 2.5	5.46 ± 1.8	2.53 ± 0.83	0.95 ± 0.31
Total Background	27.2 ± 8.4	14.0 ± 4.35	5.4 ± 1.7	2.9 ± 0.8
$t\overline{t}$	0.08 ± 0.01	1.04 ± 0.11	6.64 ± 0.70	6.3 ± 0.7
Total SM expectation	27.3 ± 8.4	15.0 ± 4.4	12.0 ± 1.8	9.2 ± 1.1
Run II data	30	19	17	10

Table 7.7: Brief overall summaries of the observed and predicted numbers of events in each decay channel (top), and as a function of the number of jets, H_T, and opposite sign requirements (bottom).

CHAPTER 8

Discussion

We have measured the $t\bar{t}$ cross-section in the dilepton decay channel using $\sim 126\,\mathrm{pb}^{-1}$ of data from Run II at the Tevatron, and obtain a result consistent with the Standard Model prediction. The focus of this analysis was directed towards increasing the acceptance for the dilepton decay signature, and in particular towards including leptons at higher pseudorapidity. Although the number of signal events observed in the data is small, no evidence is seen for any phenomena beyond the Standard Model in the kinematic distributions we have examined thus far. We expect that with ~ 1 fb^{-1} of data, precise measurements of the $|V_{tb}|$ CKM matrix element and the angular distribution of leptons in $t\bar{t}$ decays (See Fig. 2.5) will be possible. The characteristics of this distribution are determined by the fraction of longitudinally polarized W bosons present in $t\bar{t}$ decays (See Eqn. 2.10), which is predicted by the Standard Model. The dilepton decay channel has good sensitivity for these measurements, and will thus feature prominently in future tests of the Standard Model at CDF.

References

[1] F. Abe et al. Observation of Top Quark Production in $\overline{p}p$ Collisions. *Phys. Rev. Lett.*, 74:2626–2631, 1995.

[2] J. H. Christenson, J. W. Cronin, V. L. Fitch, and R. Turlay. Evidence for the 2 Pi Decay of the K(2)0 Meson. *Phys. Rev. Lett.*, 13:138–140, 1964.

[3] M. Kobayashi and T. Maskawa. CP Violation in the Renormalizable Theory of Weak Interaction. *Prog. Theor. Phys.*, 49:652–657, 1973.

[4] J. J. Aubert et al. Experimental Observation of a Heavy Particle J. *Phys. Rev. Lett.*, 33:1404–1406, 1974.

[5] J. E. Augustin et al. Discovery of a Narrow Resonance in e^+e^- Annihilation. *Phys. Rev. Lett.*, 33:1406–1408, 1974.

[6] Martin L. Perl et al. Evidence for Anomalous Lepton Production in e^+e^- Annihilation. *Phys. Rev. Lett.*, 35:1489–1492, 1975.

[7] S. W. Herb et al. Observation of a Dimuon Resonance at 9.5 GeV in 400 GeV Proton - Nucleus Collisions. *Phys. Rev. Lett.*, 39:252–255, 1977.

[8] Steven Weinberg. A Model of Leptons. *Phys. Rev. Lett.*, 19:1264–1266, 1967.

[9] W. Bartel et al. A Measurement of the Electroweak Induced Charge Asymmetry in $e^+e^- \to b\overline{b}$. *Phys. Lett.*, B146:437, 1984.

[10] DELPHI L3 OPAL The LEP Collaborations, ALEPH and the LEP Electroweak Working Group. A Combination of Preliminary LEP Electroweak Measurements and Constraints on the Standard Model. *CERN-PPE*, 95-172, 1995.

[11] G. Arnison et al. Experimental observation of isolated large transverse energy electrons with associated missing energy at $\sqrt{s} = 540$ GeV. *Phys. Lett.*, B122:103–116, 1983.

[12] G. Sauvage and J. Schacher. Latest Results from the UA2 Experiment at the CERN $\overline{p}p$ Collider: $W \to e\nu$, $Z^0 \to e^+e^-$, Hadron Jets. Invited talks given at the Int. Europhysics Conf. on High Energy Physics, Brighton, Eng., Jul 20-27, 1983.

[13] G. Arnison et al. Experimental Observation of Lepton Pairs of Invariant Mass Around 95 GeV/c^2 at the CERN SPS Collider. *Phys. Lett.*, B126:398–410, 1983.

[14] Gordon L. Kane and Michael E. Peskin. A Constraint from B Decay on Models with No t Quark. *Nucl. Phys.*, B195:29, 1982.

[15] A. Bean et al. Improved Upper Limit on Flavor Changing Neutral Current Decays of the b Quark. *Phys. Rev.*, D35:3533, 1987.

[16] L. H. Ryder. *Quantum Field Theory.* Cambridge, Uk: Univ. Pr., 1985.

[17] R. K. Ellis, W. James Stirling, and B. R. Webber. *QCD and Collider Physics*, volume 8. Cambridge Monogr. Part. Phys. Nucl. Phys. Cosmol., 1996.

[18] M. Cacciari, S. Frixione, M. L. Mangano, P. Nason, and G. Ridolfi. The $t\bar{t}$ Cross-Section at 1.8 TeV and 1.96 TeV: A Study of the Systematics Due to Parton Densities and Scale Dependence. 2003.

[19] L. Montanet et al. Review of particle properties. Particle Data Group. *Phys. Rev.*, D50:1173–1823, 1994.

[20] J. Cockcroft and E. Walton. *Proc. Roy. Soc.*, 136:619, 1932.

[21] W. K. H. Panofsky et al. Berkeley Proton Linear Accelerator. *Rev. Sci. Instrum.*, 26:111, 1955.

[22] D. Mohl, G. Petrucci, L. Thorndahl, and Simon Van Der Meer. Physics and Technique of Stochastic Cooling. *Phys. Rept.*, 58:73–119, 1980.

[23] The CDF II Collaboration. The CDF II Detector Technical Design Report. *FERMILAB-PUB-96*, 390-E, 1996.

[24] See:
`http://www.nikhef.nl/pub/departments/et/ccd_rasnik/ccd_rasnik.html`.

[25] D. Goldstein and D. Saltzberg. The RASNIK real-time relative alignment monitor for the CDF inner tracking detectors. *Nuclear Instruments and Methods in Physics Research*, A 506:92–100, 2003.

[26] D. Goldstein. A measurement of the W boson cross section using electrons in the upgrade endplug detectors, 2002.
CDF internal document: CDF/PHYS/CDF/CDFR/5975.

[27] B. Rossi. *High Energy Particles.* Prentice Hall, 1952.

[28] T. Nelson, R. Snider, and D. Stuart. Forward Electron Tracking with the PhoenixMods Package, 2003.
CDF internal document: CDF/DOC/TRACKING/PUBLIC/6278.

[29] A. Robson. Presentation to the CDF Electroweak physics group, 6/26/03.

[30] We thank Pierre Savard for this suggesting this check.

[31] D. Stuart. Presentation to the CDF electroweak physics group, 4/17/03.

[32] A. Sidoti. Presentation to the CDF electroweak physics group, 6/26/03.

[33] A. D. Martin, R. G. Roberts, W. J. Stirling, and R. S. Thorne. NNLO global parton analysis. *Phys. Lett.*, B531:216–224, 2002.

[34] E. Halkiadakis et al. $W \to e\nu$ Cross Section Analysis with Run II Data, 2003.
CDF internal document: CDF/DOC/ELECTROWEAK/CDFR/6300.

[35] A. Robson et al. A Measurement of $\sigma \cdot Br(Z^0 \to e^+e^-)$ Using Run II Central and Plug Electrons, Winter 2003.
CDF internal document: CDF/DOC/ELECTROWEAK/CDFR/6642.

[36] E. Halkiadakis et al. Measurements of $\sigma \cdot B(W \to e\nu)$, $\sigma \cdot B(Z \to ee)$ and $R = \frac{\sigma \cdot B(W \to e\nu)}{\sigma \cdot B(Z \to ee)}$ using CDF Run II Data, 2003.
CDF internal document: CDF/DOC/ELECTROWEAK/CDFR/6681.

[37] A. Attal, J. Hauser, M. Lindgen, and B. Mohr. Investigation and Reduction of Cross Talk in the Run 2 Endplug Calorimeter PES and PPR Detectors, 2003. CDF internal document: CDF/DOC/PLUG_UPGR/CDFR/6812.

[38] M. Coca et al. Central Electron Identification Efficiencies for Winter 2003 Conferences, 2003.
CDF internal document: CDF/DOC/ELECTROWEAK/CDFR/6262.

[39] R.G. Wagner. Electron Identification for Run II: Understanding and Using *Lshr*, 2003.
CDF internal document: CDF/DOC/ELECTRON/CDFR/6249.

[40] K. Bloom et al. Muon Efficiencies, 2003.
CDF internal document: CDF/ANAL/MUON/CDFR/6293.

[41] M. Tecchio. Adding CMIO Muons to the Top Dilepton Cross-Section Measurement, 2003.
CDF internal document: CDF/PHYS/TOP/CDFR/6517.

[42] L. Nodulman et al. A First Look at Run 2 High p_T Electrons, 2003.
CDF internal document: CDF/MEMO/ELECTRON/CDFR/5803.

[43] W. Sakumoto and H.S. Budd. Run II PEM Tower Transverse Response Maps, 2002.
CDF internal document: CDF/DOC/ELECTRON/PUBLIC/6181.

[44] W. Sakumoto and H.S. Budd. Determining Gains of Plug Towers using Plug Laser and Source Data, 2003.
CDF internal document: CDF/DOC/CALORIMETRY/CDFR/6433.

[45] A. Sedov et al. PEM and PHA SCL/LERs from Jan 2003 Source Data, 2003.
CDF internal document: CDF/DOC/CALORIMETRY/PUBLIC/6328.

[46] L. Nodulman. Central Electron Issues for Summer 03, 2003.
CDF internal document: CDF/MEMO/ELECTRON/CDFR/6558.

[47] R.G. Wagner. Electron Identification for Run II: Algorithms, 2003.
CDF internal document: CDF/DOC/ELECTRON/CDFR/5456.

[48] D. Goldstein. A New PEM Clustering Algorithm for Run II, 2001.
CDF internal document: CDF/DOC/CDF/CDFR/5682.

[49] B. Heinemann and A. Wyatt. Correction for Leakage Energy in the Central and Plug Calorimeters in Run II, 2002.
CDF internal document: CDF/ANAL/ELECTRON/CDFR/6167.

[50] H. Frisch. Separating Top and Z's in Dilepton Events Inside the Z Mass Window, 1995.
CDF internal document: CDF/ANAL/TOP/CDFR/3387.

[51] M. Coca and P. Tipton. Optimization Studies for the Top Dilepton Cross-Section Measurement, 2003.
CDF internal document: CDF/DOC/TOP/CDFR/6579.

[52] E. Thomson. Description of data samples for Top and Electroweak groups for Winter 2003.
CDF internal document: CDF/DOC/TOP/PUBLIC/6265.

[53] D. Goldstein et al. A Measurement of the $t\bar{t}$ Cross-Section Using Dileptons in the Central and Endplug Detectors, 2003.
CDF internal document: CDF/PHYS/TOP/6588.

[54] Y.K. Kim et al. Trigger Efficiencies for High P_T Electrons, 2003.
CDF internal document: CDF/DOC/ELECTRON/CDFR/6234.

[55] M. Tecchio. Acceptance and Background Systematics for the Top Dilepton Cross-Section Measurement, 2003.
CDF internal document: CDF/DOC/TOP/CDFR/6590.

[56] A.A. Bhatti et al. Jet Corrections for Summer 2003 Analyses (Offline Version 4.10.4), 2003.
CDF internal document: CDF/ANAL/JET/CDFR/6565.

[57] J. M. Campbell and R. K. Ellis. An Update on Vector Boson Pair Production at Hadron Colliders. *Phys. Rev.*, D60, 1999.

[58] C. Hill et al. Fake Lepton Backgrounds for the Summer 2003 Top Dilepton Cross Section, 2003.
CDF internal document: CDF/DOC/TOP/CDFR/6592.

[59] S. D. Drell and Tung-Mow Yan. Massive Lepton Pair Production in Hadron - Hadron Collisions at High-Energies. *Phys. Rev. Lett.*, 25:316–320, 1970.

[60] A. Hocker et al. Determination of Drell-Yan Backgrounds for the Run II Top Dilepton Cross Section, Summer 2003.
CDF internal document: CDF/DOC/TOP/CDFR/6591.

[61] J. Konigsberg et al. The CDF Cherenkov Luminosity Monitor, 2001.
CDF internal document: CDF/PUB/CDF/PUBLIC/5559.

[62] F. Abe et al. Measurement of the Top Quark Mass and $t\bar{t}$ Production Cross Section from Dilepton Events at the Collider Detector at Fermilab. *Phys. Rev. Lett.*, 80:2779–2784, 1998.